DETAILED CHARACTERIZATION OF NUCLEAR RECOIL PULSE SHAPE DISCRIMINATION IN THE DARKSIDE-50 DIRECT DARK MATTER EXPERIMENT

A DISSERTATION SUBMITTED TO THE GRADUATE DIVISION OF THE UNIVERSITY OF HAWAIʻI AT MĀNOA IN PARTIAL FULFILLMENT OF THE REQUIREMENTS FOR THE DEGREE OF

DOCTOR OF PHILOSOPHY

IN

PHYSICS

MAY 2017

By

Erin Edkins Ludert

Dissertation Committee:

Jelena Maricic, Chairperson
Jason Kumar
John Learned
Sandip Pakvasa
Olga Boric-Lubecke

Keywords: dissertations, DarkSide-50, dark matter, direct detection, calibration, neutrons

To my grandparents,

June and Darrold Yeager,

for their unconditional love and unwaivering support. You are missed beyond words.

ACKNOWLEDGMENTS

I want to express my appreciation and gratitude to my advisor, Dr. Jelena Maricic. Thank you for your support and constant encouragement. Your confidence in me has been a tremendous boost in times of doubt. I owe a special debt of gratitude to Bernd Reinhold, our post-doc during my research, who guided, argued with, tolerated and patiently instructed me until I could reasonably be called a scientist. I'm not sure what I would have done without you. A huge thank you to my fellow graduate student, friend and co-conspirator, Brianne Hackett, who has been by my side since the very beginning. Graduate school has been an amazing, world-traveling adventure, which I am so glad I was able to share with you. After all our journeys, you are truly like family to me.

In my time at UH, there have been several professors who have been incredibly helpful to me. I am thankful to my committee members, Sandip Pakvasa and Olga Boric-Lubecke, for your time in getting me to this point. Thank you to Jason Kumar, whom I can always count on for a Star Wars "dark side" pun or a great movie reference, in addition to the answer to just about any physics question I could think of. I am grateful to have been able to have Xerxes Tata to teach me particle physics, who has gifted me not only with the clearest understanding of quantum mechanics anyone could hope for, but also with the knowledge of how to do my physics problems like a donkey. To John Learned, who responded to my graduate school inquiry, I owe sincerest thanks. You changed my life for the better, and I will never forget it.

Working on DarkSide afforded me the opportunity to work with people from all over the world, many of whom have had a tremendous impact on me. I would like to thank Andrea Ianni, Augusto Goretti, Nicola Canci, Yura Suvorov and Marco Carlini, who supported and assisted during our multiple calibration campaigns. Your friendship and expertise were indispensable. A special thank you to Masayuki Wasa, who has always been readily available and willing to help, no matter how much was already on his plate. Thank you for never failing to answer my emails, regardless of time of day, and for all your patience with my endless questions. I am grateful for all the mentoring I received from the senior members of the collaboration, notably Peter Meyers and Emilija Pantic. Thank you for the long discussions via email and Skype, and all of your excellent feedback. I also want to thank our Paris Monte Carlo group, Davide Franco, Stefano Perasso and, especially, Paolo Agnes, for your help throughout my research experience. Thank you to Stephan Pordes for your piercing wit and great analysis questions. Your self-effacing manner belies an uncanny ability to provide real insight, which as a student I found truly useful. To my fellow DarkSide PhD students, Shawn Westerdale, Alden Fan, Andrew Watson and Luca Pagani, from whom I have benefited from both your collaboration and commiseration, thank you.

Finally, I would not be here without the love and support of my family. I have always been able to count on my incredible mother, Lynlee Yeager Edkins, who has encouraged my dreams and my love of science all my life. To my in-laws, Juan and Maite Ludert, thank you for welcoming me

into your family with open arms. You never fail to provide love and support in every way. Lastly, to my husband, Alejandro Ludert, thank you for literally, not figuratively, everything. You are the best partner anyone could hope for on this journey.

ABSTRACT

While evidence of non-baryonic dark matter has been accumulating for decades, its exact nature continues to remain a mystery. Weakly Interacting Massive Particles (WIMPs) are a well motivated candidate which appear in certain extensions of the Standard Model, independently of dark matter theory. If such particles exist, they should occasionally interact with particles of normal matter, producing a signal which may be detected. The DarkSide-50 direct dark matter experiment aims to detect the energy of recoiling argon atoms due to the elastic scattering of postulated WIMPs. In order to make such a discovery, a clear understanding of both the background and signal region is essential. This understanding requires a careful study of the detector's response to radioactive sources, which in turn requires such sources may be safely introduced into or near the detector volume and reliably removed.

The CALibration Insertaion System (CALIS) was designed and built for this purpose in a joint effort between Fermi National Laboratory and the University of Hawaii. This work describes the design and testing of CALIS, its installation and commissioning at the Laboratori Nazionali del Gran Sasso (LNGS) and the multiple calibration campaigns which have successfully employed it.

As nuclear recoils produced by WIMPs are indistinguishable from those produced by neutrons, radiogenic neutrons are both the most dangerous class of background and a vital calibration source for the study of the potential WIMP signal. Prior to the calibration of DarkSide-50 with radioactive neutron sources, the acceptance region was determined by the extrapolation of nuclear recoil data from a separate, dedicated experiment, ScENE, which measured the distribution of the pulse shape discrimination parameter, f_{90}, for nuclear recoils of known energies. This work demonstrates the validity of the extrapolation of ScENE values to DarkSide-50, by direct comparison of the f_{90} distribution of nuclear recoils from ScENE and an AmBe calibration source. The combined acceptance as defined by ScENE and the *in-situ* AmBe calibration were used to establish the best WIMP exclusion limit on an argon target. Unfortunately, radioactive sources used for the calibration of DarkSide-50 are universally accompanied by gamma decays, which obscure the low energy region where most WIMP interactions are expected to occur and seem to make continuing dependence on an external measurement such as ScENE inevitable. However, this work presents a novel method of nuclear recoil calibration employing event selection, unique to the design of DarkSide-50, which produces a nearly pure sample of nuclear recoils. Further, it describes the execution of a neutron calibration campaign, from planning to analysis, which yielded a valuable data set for defining the acceptance region. Together with the event selection techniques, this allows for the definition of the acceptance region independent of ScENE values. Two analytical models of the f_{90} distribution are described and their results for nuclear recoils are compared. Finally, a detailed study of integrated noise in nuclear and electron recoil events is presented, which demonstrates a difference between these classes of events for the first time.

TABLE OF CONTENTS

LIST OF TABLES

LIST OF FIGURES

CHAPTER 1
DARK MATTER

1.1 Evidence for Dark Matter

Observational evidence of the existence of non-radiative, gravitationally interacting matter has been accumulating for decades. While the astronomical and cosmological evidence now seems almost overwhelming, the exact nature of this matter remains elusive. The discovery of particle dark matter is currently the holy grail of high energy physics, with multiple technologies engaged in the hunt. In this chapter, I will describe the evidence for dark matter, from galactic to cosmological scales, and argue that the such evidence cannot be fully explained by the known particles of the Standard Model.

1.1.1 Galaxies

Galaxy rotation curves, which demonstrate the speed at which stars and gas rotate as a function of distance from the galactic center, provide some of the most robust evidence for dark matter at galactic scales. Rotation curves are obtained using the Doppler shift of spectral lines, notably the 21-cm line from neutral hydrogen. Hydrogen clouds extend much farther out than the visible stellar disk, and allow for the measurement of galactic orbital speeds beyond the radius of visible stars. Newtonian mechanics tells us that the speed of an orbiting body is given by:

$$v(r) = \sqrt{\frac{GM(r)}{r}}$$

where M is the mass contained within the radius, r. If the distribution of matter in a galaxy is well represented by what we can see, that is, luminous matter, we would expect the velocity to fall off with increasing radius as $1/\sqrt{r}$, as is the case for the planets in the solar system. However, typical galaxies have velocity curves which continue to slowly rise or to flatten out at large radii, implying that the mass increases linearly with r, ie: $M(r) \propto r$. This was first shown conclusively by Vera Rubin and Ken Ford in the late 1970's and early 1980's [1] [2], although earlier measurements had been made without indicating unseen matter as a cause [3].

1.1.2 Galaxy Clusters

Although the 1980's saw acceptance of the existence of dark matter, the term was coined many years earlier in 1933 by Fritz Zwicky, an astrophysicist at the California Institute of Technology [4]. Zwicky studied the velocities of member galaxies of several galactic clusters, including the Coma cluster. Given the galaxy velocities, he was able to apply the virial theorem to the cluster,

which relates the average kinetic energy of bodies in a gravitationally bound system to the average gravitational potential energy of the system:

$$\bar{T} = -\frac{1}{2}\bar{V}$$

Since the gravitational potential energy is a function of the mass of the system, the virial theorem provides an estimate of the total mass of the cluster. Using this technique, Zwicky estimated that in order to achieve the average velocity found in the Coma Cluster, the mass of the cluster would have to be 400 times greater than what was measured from the visible matter [4].

Gravitational Lensing

In 1937, Zwicky suggested another technique to detect non-luminous matter which would prove pivotal in the case for dark matter: gravitational lensing [5]. Massive objects bend the spacetime around them, changing the trajectory of photons as they move through the curved space. As massive bodies pass in front of more distant background stars and galaxies, the images of these objects are distorted, an effect known as gravitational lensing. There are three classes of gravitational lensing: strong lensing, weak lensing, and microlensing. Strong lensing produces the effect most apparent to the eye, creating clear Einstein rings or multiple images of the background object. Weak lensing, in contrast, produces distortions on the order of a few percent, and requires statistical techniques to analyze large numbers of sources. Microlensing is the temporary, apparent brightening of the background star or galaxy during the passage of a foreground object. Of these, weak lensing has been the most important in mapping concentrations of non-luminous matter.

Figure 1.1: The Bullet Cluster, the result of the collision of two sub-clusters. Pink: X-ray image of colliding gas. Blue: regions of highest mass concentration. Image Credit: NASA/CXC/CfA/M.Markevitch et al.; Optical: NASA/STScI; Magellan/U.Arizona/D.Clowe et al.; Lensing Map: NASA/STScI; ESO WFI

An excellent and famous example of the revelations made possible by weak lensing is the Bullet Cluster. This cluster is actually the result of a merger of sub-clusters. As the sub-clusters collide, the individual galaxies, with vast stretches of space between them, pass by each other mostly undisturbed. The majority of the matter of the clusters is not contained within the member galaxies, however, but in intergalactic gas, which collides energetically during the merger. A composite image of the Bullet Cluster shows the galaxies, seen in the visible spectrum, the hot, collisional gas detected by X-ray telescopes, and the location of the bulk of the cluster matter, as revealed by gravitational lensing. If most of the matter in the Bullet Cluster was luminous, we would expect gravitational lensing to show a center of mass which coincides with the location of the X-ray emitting gas. Instead, we see that it resides near the sparse galaxies. From this we can conclude that the majority of the matter not only passed through without interacting, but is non-radiative, revealing itself only through its effect on the spacetime around it [6].

1.1.3 The Cosmos

While results from galactic rotation curves and gravitational lensing reveal the presence of unseen matter, with this evidence alone it could still be argued that this matter is simply large numbers of asteroids, planets and stellar remnants, which do not emit enough light to be seen (if any), and are sparse enough to have negligible interactions in cluster collisions. However, comprehensive searches for microlensing effects which would accompany these objects have not been able to account for more than a fraction of the necessary mass [7]. Additionally, multiple supporting measurements on the cosmological scale demonstrate convincingly that this matter is of a type which is as yet undiscovered.

Big Bang Nucleosynthesis

Big Bang Nucleosynthesis (BBN) provides us with a measure of the abundance of baryonic matter in the universe. BBN is the process by which the lightest elements (D, ^{3}He, ^{4}He, and ^{7}Li) were formed from hydrogen in the first few minutes after the Big Bang. During this time, the universe was very hot and dense, with a mostly uniform temperature distribution. After about 20 minutes, the universe had expanded and cooled to the point that nuclear fusion stopped, leaving the elements which would form the earliest stars [8]. The abundances of these elements at this point depend on the baryon-to-photon number ratio (see Figure 1.2):

$$\eta_{10} \equiv 10^{10}(\frac{n_B}{n_\gamma})$$

Of these, D/H is the most informative, as deuterium produced in stars is converted to ^{4}He, as is any deuterium incorporated during stellar formation. This means any remaining D was produced during BBN and thus provides a lower bound on its original abundance. By observing the D/H

ratio in far distant regions, which give a picture of the universe at an earlier time before there could have been significant conversion of D to ^{4}He, we get a measure of the baryon density [9]:

$$\Omega_b h^2 = 0.02202 \pm 0.00046$$

This corresponds to a mass-energy density for baryonic matter of less than 5%.

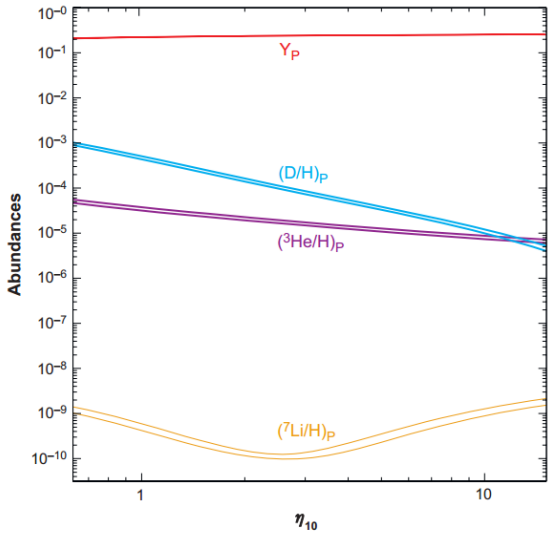

Figure 1.2: The primordial abundances of D, ^{3}He, ^{4}He (labeled as Y_p), and ^{7}Li, relative to ^{1}H, as predicted by Big Band Nucleosynthesis. The uncertainties are indicated by the width of the bands. [8]

Cosmic Microwave Background

For the first few 100,000 years after the Big Bang, the universe was too hot for electrons to combine with the newly formed baryonic elements. During this time, these ions existed in a plasma state, opaque to radiation. As the universe continued to expand and cool, electrons and protons combined to form neutral atoms, transparent to radiation. When the universe was 380,000 years old, the epoch of recombination was effectively completed, and photons began to move freely for the first time. These photons are still visible today in the form of the Cosmic Microwave Background (CMB).

The CMB, at a mean temperature of 2.725 K, is highly isotropic, with variations in temperature occurring at the 10^{-4} level. These anisotropies provide a critical snapshot of the very early universe. On the largest scales, areas of higher density can be seen as slightly cooler regions in the CMB, as photons lost energy escaping the larger gravitational potentials. On smaller scales, local overdense regions caused the baryon-photon plasma to be compressed, increasing the pressure. This pressure would increase until it forced the region to expand. The outward expansion, in turn, allowed the

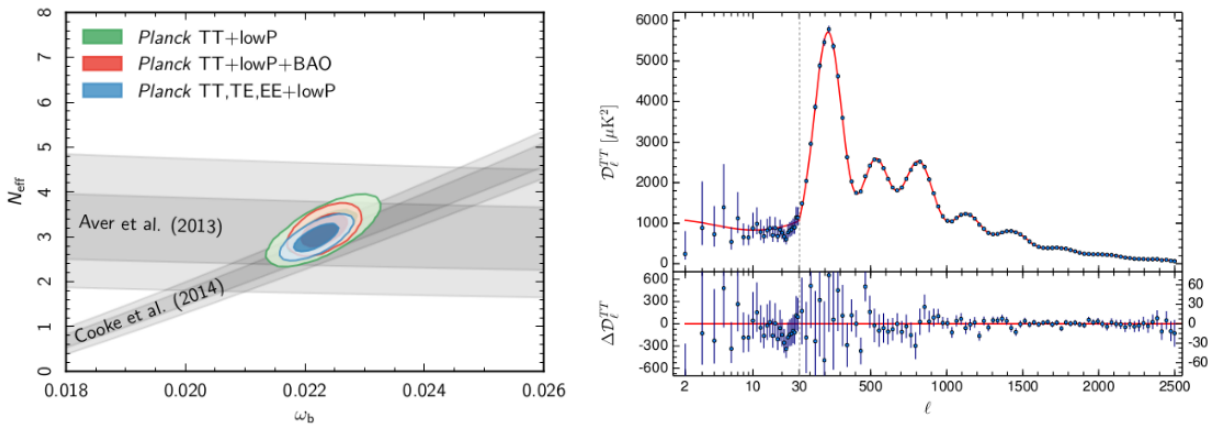

Figure 1.3: *Left:* Comparison of constraints from Plank and BBN. Here N_{eff} is the radiation density, while ω_b is the relative baryon density. The contours represent the 68% and 95% confidence regions. *Right:* CMB temperature power spectrum, demonstrating the Baryonic Acoustic Oscillations which occurred when the universe was less than 380,000 years old [10].

pressure to decrease, until it was overcome by gravitational attraction and collapsed inward again. These periodic fluctuations, called Baryonic Acoustic Oscillations (BAO), reveal the conditions in the universe at the time of the last scattering, notably the relative abundance of baryons. The results are in excellent agreement with those from BBN [10]:

$$\Omega_b h^2 = 0.02226 \pm 0.00023$$

While baryonic matter accounts for less than about 5% of the mass-energy of the universe, the results show the fraction of total matter is near 30%:

$$\Omega_m = 0.308 \pm 0.012$$

Thus, more than a quarter of our universe is comprised of a form of matter which is non-baryonic.

Large Scale Structure

Neutrinos are a type of particle discovered in 1956 [11]. They are non-baryonic, abundant, and as was determined in 1998, they have mass [12]. Additionally, they are electrically neutral, so they do not interact with light and are, therefore, non-radiative. Given that they possess all of the qualities we have so far seen are required of dark matter, they would seem to be an excellent dark matter candidate. However, although neutrinos have mass, it is well constrained to be significantly less than required to be the missing dark matter [10]. Additionally, neutrinos at large redshift are relativistic particles, moving near the speed of light. This high velocity gives neutrinos a large free streaming length, the distance that a particle is able to travel from random motions. In the early

universe, this would have prevented matter from clustering on small scales and created a paradigm of top-down structure formation, where the largest structures form first and successively smaller objects form through fragmentation. This is ruled out by observations that the age of clusters is less than that of their member galaxies [13], as well as N-body simulations of galaxy cluster formation [14].

1.2 WIMP Dark Matter

Although we have seen what dark matter is not, we have yet to determine what it is. In this case, it is instructive to begin with a consideration of the properties we know dark matter must possess:

- Gravitationally interacting
- Electrically neutral
- Non-relativistic
- Stable ($\tau_\chi \gg \tau_U$)

Since existing Standard Model particles have been ruled out as the sole source of dark matter, at the time of the Big Bang there must have been another particle, or class of particles, formed. When the universe was still hot and dense, these particles would have been in thermal equilibrium, annihilating with each other to form lighter particles, and in turn being created through the energy of particle annihilation. As the universe expanded and cooled, at a certain point there would not be enough energy for massive dark matter particles to be formed from the annihilations of lighter elements, and their number density would have dropped off exponentially. When the universe had expanded enough, dark matter annihilations would have effectively ceased, leaving their abundance roughly the same as it is today. This relic density which we are left with today depends on the dark matter annihilation cross section:

$$\Omega_\chi \propto \frac{1}{\langle \sigma(\chi\chi \longrightarrow qq)v \rangle}$$

Based on this relationship, a value of $\Omega_\chi \sim 1$ is obtained when the cross section is on the order of the weak nuclear force. Thus, we can add weak scale interactions to the properties listed above [15].

Weakly Interacting Massive Particles (WIMPs) are a well motivated dark matter candidate arising naturally from certain extensions of the Standard Model. Their popularity stems from the fact that they were hypothesized independently of dark matter theory, and have all the properties required of dark matter, including the correct relic abundance. This coincidence is referred to as the "WIMP miracle." There are several types of theoretical particles which fall under the WIMP

category. These include neutralinos (from Super Symmetry) and the lightest Kaluza-Klein particle (from the Universal Extra Dimensions model).

1.2.1 Methods of Detection

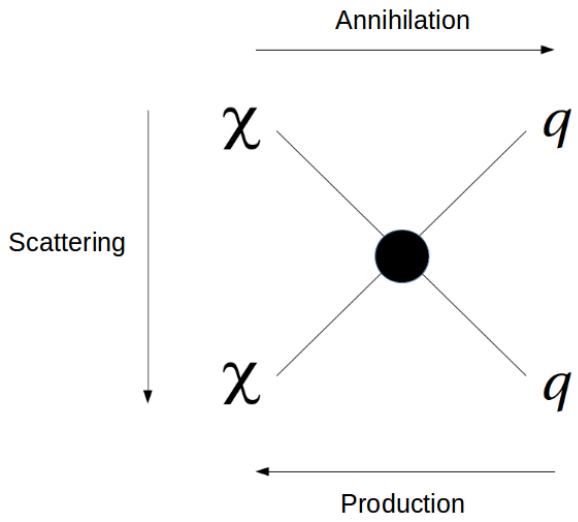

Figure 1.4: Non-gravitational interactions of WIMP particles, X, with Standard Model particles, q.

Although dark matter has been observed through its gravitational interactions on astronomical scales, to discover particle dark matter in the laboratory we must look for visible signatures from stronger interactions. These are summarized in Figure 1.4.

Dark matter annihilations may be detected by their annihilation products, including high energy photons and antimatter particles, such as positrons and anti-protons. The signal for this type of detection, known as indirect detection, would consist of an excess of these particles. Indirect searches focus on regions where a high concentration of dark matter is expected, such as the Milky Way galactic center, the interior of the Sun, and the Earth's core [16].

Production of dark matter particles may occur at particle colliders, such as the LHC. Although it would not be possible to detect the dark matter particles themselves, their presence would be seen as missing momentum in the collision products [17].

Finally, dark matter may be directly detected by elastically scattering off the nuclei of normal atoms. Direct detection experiments aim to measure the energy of the target atom thus imparted. The next section will describe this method of detection in detail.

1.3 Direct Detection

1.3.1 WIMP Signal and Event Rate

Following [18], the recoil energy imparted to a target nucleus by the elastic scatter of a WIMP particle can be expressed by:

$$E_R = \frac{\mu^2 v^2}{m_N}(1 - \cos\theta) \tag{1.1}$$

where

$$\mu = \frac{m_N m_\chi}{m_N + m_\chi}$$

is the WIMP-nucleus reduced mass and θ is the scattering angle in the center-of-mass frame. The differential scattering rate, then, is:

$$\frac{dR}{dE_R} = N_T \frac{\rho_{dm}}{m_\chi} \int_{v_{min}}^{v_{max}} d\vec{v} f(\vec{v}) v \frac{d\sigma}{dE_R} \tag{1.2}$$

where N_T is the number of target nuclei. In this equation, ρ_{dm} is the local WIMP density in the galactic halo, v is the WIMP velocity and $f(\vec{v})$ is the velocity distribution function. These values are input parameters which must be derived from astrophysical models of the galactic halo. The experimental observables, then, are $\frac{d\sigma}{dE_R}$, the WIMP-nucleus differential cross section, and m_χ, the WIMP mass. Here the maximum WIMP velocity, v_{max}, is the escape velocity in the solar system frame, generally taken to be 544 km/s [19]. The minimum WIMP velocity, v_{min}, is given by:

$$v_{min} = \sqrt{\frac{m_N E_{th}}{2\mu^2}}$$

where E_{th} is the detection threshold energy of the detector.

According to [20], to first approximation Eq. 1.2 can be expressed as:

$$\frac{dR}{dE_R} = \frac{R_0}{E_T} e^{-\frac{E_R}{E_T}} \tag{1.3}$$

where R_0 is the total event rate and E_T is a constant dependent on the kinetic energy of the dark matter particle, as well as its mass and the mass of the target nucleus. Thus, we can expect the signal rate to decrease exponentially with recoil energy.

Eq. 1.3 assumes the simplest scenario, wherein the detector is stationary in the galaxy, the escape velocity is infinite and there is zero momentum transfer so that the scattering cross section is constant. Adjusting for the velocities does not change the functional form of Eq. 1.3; allowing for momentum transfer, however, requires a non-constant cross section:

$$\sigma(E_R) = \sigma_0 F^2(E_R) \tag{1.4}$$

where σ_0 is the zero momentum transfer cross section and F is the nuclear form factor which is a function of the recoil energy. The form factor is a number less than one which becomes important when the de Broglie wavelength is no longer large compared to the radius of the target nucleus. That is, when:

$$\lambda = \frac{h}{p} \leq r_0 A^{1/3}$$

for a momentum transfer of:

$$\langle p \rangle = \mu \langle v \rangle$$

In this case, the scattering amplitudes across individual nucleons lose coherence, and the event rate becomes form factor suppressed. This can be seen in Figure 1.5, where the event rate is shown as a function of recoil energy for various targets. Higher mass nuclei are especially affected as the nuclear recoil energy increases, making low detector thresholds critical for detectors using heavier target materials.

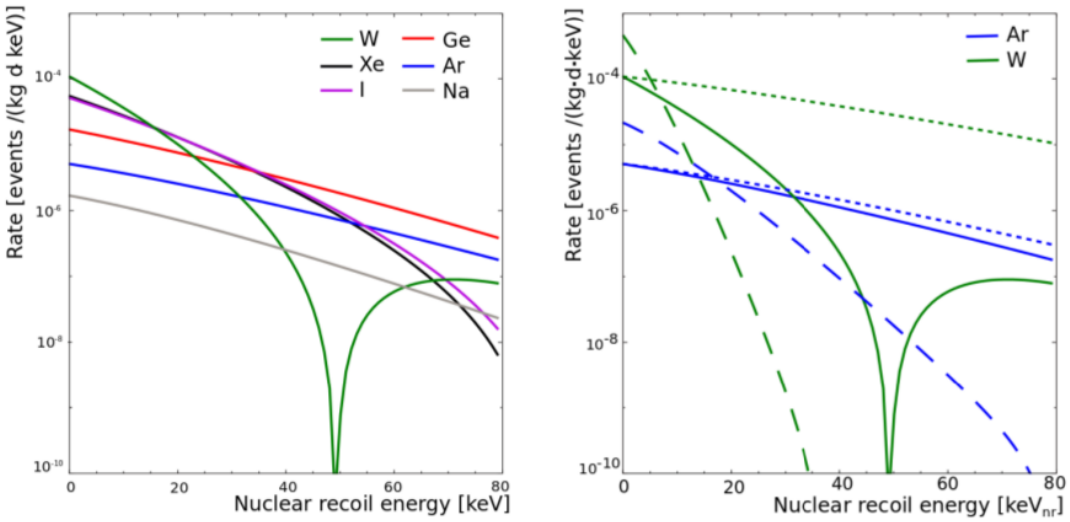

Figure 1.5: *Left:* Differential event rate for a scattering cross section of 10^{-45} cm^2 and a WIMP mass of 100 GeV/c^2 on target nuclei of different masses. *Right:* The effect of neglecting the form factor is shown in the dotted line, demonstrating the importance of form factor suppression on heavier nuclei, such as tungsten (green), versus lighter nuclei, such as argon (blue). The dashed line represents the differential scattering rate for a WIMP mass of 25 GeV/c^2. [21]

In the simplest case, the WIMP-nucleus cross section may be further modified by expressing σ_0 as a sum of spin-independent and spin-dependent terms:

$$\sigma_0 = \sigma_{SI} + \sigma_{SD} \tag{1.5}$$

The differential scattering cross section is then:

$$\frac{d\sigma}{dE_R} \propto \sigma_{SI} F_{SI}^2 + \sigma_{SD} F_{SD}^2 \tag{1.6}$$

For the spin-independent case, the cross section is dependent on the mass of the target nucleus:

$$\sigma_{SI} \propto [Z f_p + (A - Z) f_n]^2 \tag{1.7}$$

The coupling strengths for protons and neutrons, f_p and f_n, are generally assumed to contribute equally, so that σ_{SI} goes as A^2. This dependence on atomic mass causes a rate enhancement for large nuclei at low recoil energies before form factor suppression becomes dominant.

In spin-dependent scattering, the cross section goes as:

$$\sigma_{SD} \propto [a_p \langle S_p \rangle + a_n \langle S_n \rangle]^2 \frac{J+1}{J} \tag{1.8}$$

where $a_{p,n}$ are the spin-dependent proton/neutron couplings, $S_{p,n}$ are the expectation values of the total proton/neutron spin and J is the nuclear angular momentum. Since only unpaired nucleons will contribute to spin-dependent interactions, experiments hoping to detect this form of scattering must utilize target materials with an odd number of protons or neutrons.

1.3.2 Techniques for Direct Detection

For direct detection experiments, the goal is to measure the recoil energy of a scattered atom after a WIMP interaction. This requires target materials which produce a detectable signal from the scattering, which may be in the form of crystal lattice vibrations (phonons), scintillation light or ionization, or bubble nucleation. Additionally, the low expected energy of WIMP-induced recoils (at the level of a few 10's of keV) along with the low event rate requires detection technologies with very low thresholds combined with robust background mitigation. Several different methods, described below, have been employed for this purpose.

Scintillation

Scintillation has been used as a method of particle detection since the beginning of the 20th century [22]. Scintillation is the process by which atoms of a target material, excited by the scattering of a particle, emit light. This light can then be detected by light collection devices, commonly photomultiplier tubes (PMTs). Although many materials scintillate, in order to be a good candidate for particle detection the material must efficiently convert the recoil energy to scintillation light, as well as be transparent to this light, ie: the scintillation light must not be reabsorbed by the detector material. Additionally, the de-excitation time, the time between the scattering event and the emission of light, must be short in order to allow for the detection of multiple scatter events, which are certain to be caused by background particles, as well as minimize dead time in the

detector. Materials meeting these requirements include inorganic crystals, such as NaI(Tl), and noble elements, such as argon and xenon, in their liquid state.

Phonons

Following a particle recoil in a crystal lattice, phonons - vibrations of the electrons and nuclei of the lattice - are produced. To use this process for dark matter detection, the detector material is cooled to cryogenic temperatures. The phonons cause a change of temperature in the detector, which, because of the T^3 dependence of dielectric crystals, can be measurable even for a tiny recoil energy. This allows these detectors to reach low energy thresholds and, thus, obtain sensitivity to potentially low mass WIMPs [23].

Bubble Nucleation

Bubble chamber detectors use superheated fluids kept just below the boiling point to detect bubble nucleation from the passage of particles. The events are observed both optically and acoustically. These types of detectors have the advantageous ability to adjust the temperature and pressure such that only nuclear recoil events, which lose a large amount of energy as a function of distance, will cause the formation of bubbles, eliminating the large β and γ backgrounds common to most WIMP searches. They are also sensitive to multiple scatter events and can use this as an additional form of background rejection. Because fluorine is typically used in the target material, which has an unpaired proton, they are sensitive to the spin-dependent WIMP scattering channel. However, although it is possible to efficiently separate α recoils from other events based on the acoustic signal, event energy is not readily reconstructed beyond the threshold required for bubble nucleation. Therefore these devices are only able to count the number of candidate events above threshold [21] [23].

1.3.3 Current Status of Direct Detection

Multiple direct detection experiments are currently engaged in the search for dark matter. Starting in 1995, the DAMA collaboration has been studying the annual modulation of the event rate using NaI(Tl) crystals [24]. Located at the Laboratori Nazionali del Gran Sasso in Italy, this experiment exploits the regular change in event flux which is expected to be caused by the Earth's movement through the galactic dark matter halo as it revolves about the Sun. The detector is disadvantaged in that it does not have the ability to discriminate between β/γ events and nuclear recoils, and can only measure total flux as a function of time. However, the annual modulation induced by dark matter should have several defining features which would allow it to be distinguished from simple variations in the background spectrum. Specifically, such a modulation should have a one year period, with a maximum amplitude around June 2nd, and would be comprised entirely of single

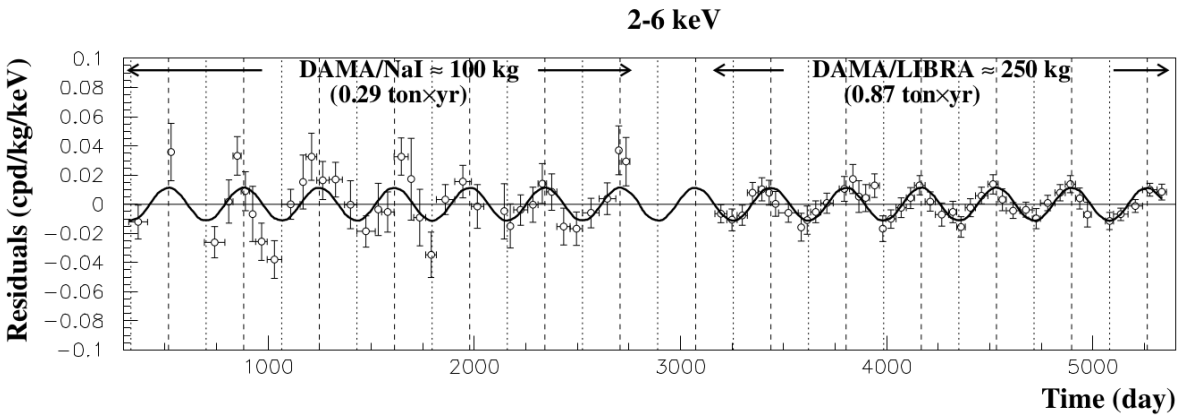

Figure 1.6: The DAMA signal, as seen in seven annual cycles by the first iteration of the experiment, DAMA/NaI, and six annual cycles by the upgraded DAMA/LIBRA [24].

scatter events. This signal does not depend on the model assumed, only on the halo distribution, which would affect the amplitude but not the period or phase. Additionally, unlike seasonal effects, the phase would not depend on the hemisphere (North or South).

The DAMA collaboration has reported the detection of precisely such a signal, currently at a 9.3σ C.L. over 14 annual cycles, in the 2-6 keV energy range [24]. Unfortunately, this result is in tension with exclusion limits set by other experiments. Although a few collaborations, such as CDMS and CRESST-II, had initially reported potential WIMP events, improvements in detector components and analysis revealed these to be consistent with the expected background [25] [26].

Several experiments have attempted to directly verify or rule out the DAMA signal. Most recently, the DM-Ice collaboration released the results of a 3.6 year search with DM-Ice17, the first detector in the program. With the same target material, NaI(Tl), as DAMA, DM-Ice is not subject to systematic differences in interaction rates between experiments with different targets. Located at the South Pole under 2200 m.w.e of glacial ice, this experiment should be able to separate an annual modulation due to seasonal effects, which change phase between hemispheres, and the dark matter signal. The current signal detected is consistent with zero modulation, however, with only 17 kg active mass and a high level of internal background, DM-Ice17 is not yet sensitive enough to make a definitive claim [27].

The current best limit has been set by the LUX collaboration. With an active mass of 250 kg, the LUX detector is a liquid xenon TPC (see Section 2.3) located at the Sanford Underground Research Facility in Lead, South Dakota. For a WIMP mass of 50 GeV/c^2, a 3.35×10^4 kg·day exposure set an exclusion limit of 1.1×10^{-46} cm^2 [28].

With no clear WIMP signature so far found, the potential for discovery is more than ever dependent on the ability to mitigate background interactions. Beyond merely shielding the detector, this requires the capacity to discriminate between classes of events, such as β/γ interactions and

nuclear recoils, as well as actively identify events which may mimic the WIMP signal. Liquid argon as a target material allows for excellent event discrimination. With a lower atomic mass than xenon, argon is sensitive to a different range of WIMP masses, making searches with these two targets complimentary.

CHAPTER 2
LIQUID ARGON AS A TARGET FOR DIRECT DETECTION

2.1 Scintillation Mechanism

For a given recoil of an argon atom, the recoil energy will be split amongst ionization, excitation and heat. In the case of heat energy, the scattering increases the kinetic energy of the target argon atom. This energy is not visible (ie: cannot be detected) and thus is considered lost [29]. In the case of excitation, the excited argon atom combines with an argon atom in the ground state to form a diatomic excimer (excited dimer, Ar_2^*) in either the singlet ($^1\Sigma_u^+$) or triplet state ($^3\Sigma_u^+$) (See Table 2.1). Upon relaxation, the excimer will decay with the emission of a VUV photon (at 128 nm for argon). The excimer lifetime is very different for the two excited states: in the case of the singlet state, the excimer decays after only 7 ns, whereas the triplet state survives for 1.6 μs. In the case of ionization, an ionized dimer forms (Ar_2^+). This state lasts until eventual electron recombination, ending in the excited dimer state. The process then follows the excitation path, with the final emission of a VUV photon. Thus, both ionization and excitation channels result in scintillation. This process is illustrated in Figure 2.1.

Recoil events which are caused by scattering electrons or photons will preferentially create excimers in the long-lived triplet state, and are more likely to ionize the argon atom. Conversely, nuclear recoil events, such as those produced by neutrons, alpha particles, or WIMPs, will lead to excimers in the short-lived singlet state, with less ionization. This difference in excimer production, coupled with the large separation in singlet vs triplet lifetimes, allows for event discrimination at the level of 10^7 in argon from the scintillation signal alone [30].

Atomic configuration	State	Energy
[Ne] $(3s)^2(3p)^6$	$^1S_0$	0
[Ne] $(3s)^2(3p)^5 \uparrow (4s) \downarrow$	$^1P_1$	11.82 eV
[Ne] $(3s)^2(3p)^5 \uparrow (4s) \uparrow$	$^3P_0$	11.72 eV
	$^3P_1$	11.62 eV
	$^3P_2$	11.54 eV

Table 2.1: Lowest excited states of argon atoms. Excimer formation is possible in the $^3P_1$ (producing the excimer singlet state) and $^3P_2$ (producing the excimer triplet) states.

2.2 Energy Transfer

Neglecting the energy lost as heat, the energy imparted to the argon target can be written as:

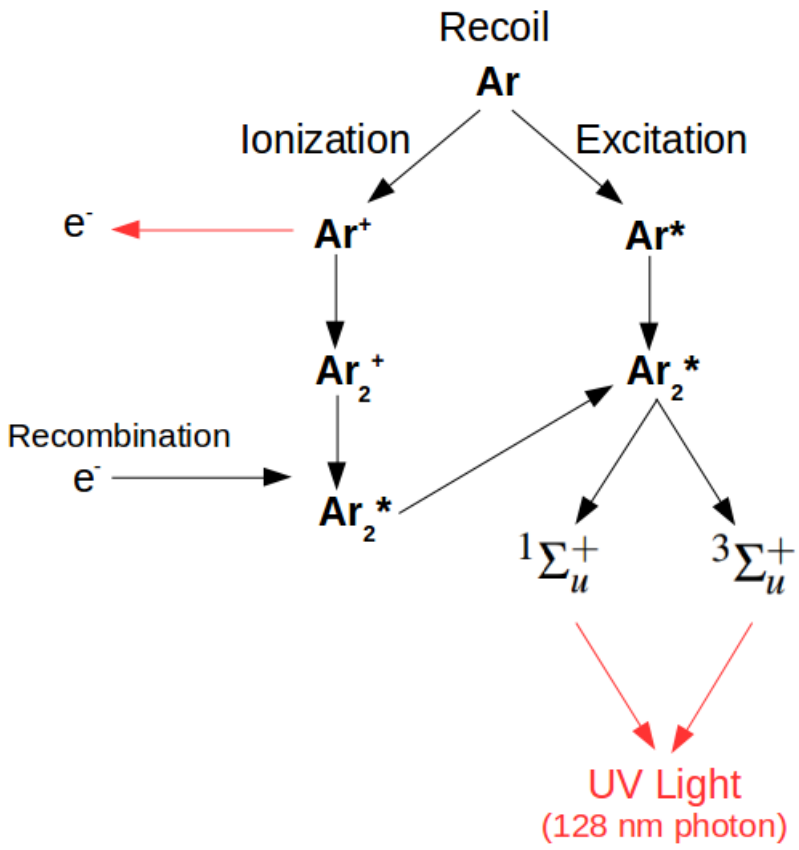

Figure 2.1: Schematic of the scintillation process in argon.

$$E_0 = N_i E_i + N_{ex} E_{ex} \tag{2.1}$$

where E_i and E_{ex} are the ionization and excitation energies and N_i and N_{ex} are the numbers of ionized and excited atoms. Assuming that each ionized or excited atom will yield one scintillation photon, the maximum number of photons produced will be [31]:

$$N_{ph} = N_i + N_{ex} = N_i\left(1 + \frac{N_{ex}}{N_i}\right) = \frac{E_0}{W}\left(1 + \frac{N_{ex}}{N_i}\right) \tag{2.2}$$

Here $W = E_0/N_i$ is the average energy required to produce one electron-ion pair. We can then write the average energy to produce a single scintillation photon, W_{ph}, as:

$$W_{ph} = \frac{W}{1 + \frac{N_{ex}}{N_i}} \tag{2.3}$$

The values of N_{ex}/N_i and W have been experimentally measured, allowing for the calculation of W_{ph} [32] [33]. The results for electron recoils are summarized in Table 2.2.

W	23.8 ± 0.3 [eV]
N_{ex}/N_i	0.21
W_{ph}	19.5 ± 0.1 [eV]

Table 2.2: Measured values of W and N_{ex}/N_i, along with the calculated value of W_{ph} for electron recoils in liquid argon.[33] [34]

Although we have discussed the physics of argon scintillation in terms of the scattering of a single atom, in reality a particle interacting with the target medium will scatter off many atoms, depositing its energy in a track of ionized and excited argon. The length and density of this track, measured in terms of dE/dx, or the linear energy transfer (LET), depends on the particle species. Nuclear recoils from neutrons or WIMPs create dense ionization / excitation tracks and thus have large LETs relative to electron recoils. Critically, although the lifetimes of the singlet and triplet states are independent of the track density, the ratio of singlet to triplet states produced in the interaction is determined by the LET. For nuclear recoils, this ratio is approximately 3, whereas for electron recoils it is ~ 0.3 [35]. This forms the basis for the event discrimination introduced in the previous section.

The scintillation light yield is likewise different for electron and nuclear recoils. In the case of nuclear recoils, a much larger fraction of the recoil energy will be lost as heat. We, therefore, define a parameter, L_{eff}, which is the scintillation efficiency of nuclear recoils relative to electron recoils:

$$L_{eff} = \frac{N_{ph}(E)_{nr}}{N_{ph}(E)_{er}} \tag{2.4}$$

For liquid argon, L_{eff} has been measured to be 0.25 ± 0.1 for recoil energies greater than 20 keV [36].

2.3 Dual-Phase Time Projection Chambers

In order to utilize liquid argon for dark matter searches, experiments such as DarkSide use a dual-phase design, shown schematically in Figure 2.2. A cylindrical volume of liquid argon is observed by two arrays of light collection devices, typically photomultiplier tubes (PMTs). The main volume of liquid argon is immersed in an applied electric field and topped with a thin layer of argon in its gaseous state. When an incoming particle scatters off the liquid argon target, it will deposit its energy as ionization and excitation as described above. Some of the ionized electrons will recombine and contribute to the scintillation signal, however some will be carried away due to the electric field. These electrons will drift upwards until they reach an extraction grid, just below the level of the gaseous argon. Here a stronger electric field will accelerate them out of the liquid and into the gas

layer, producing a second scintillation signal. Because this secondary scintillation light is caused by ionized electrons, it is often called the ionization signal, or S2. The primary scintillation signal, then, is referred to as S1.

The XY position of the event can be reconstructed by the projection of the hit pattern of S2 on the PMTs, while the Z coordinate is provided by the time between S1 and S2. This feature, along with the employment of argon in both its liquid and gas phases, leads to the term for these detectors, dual-phase time projection chambers (TPCs).

At 128 nm, the scintillation photons have too small a wavelength to be detected by PMTs, so a wavelength shifter is used. At each PMT, the now visible photons are absorbed by the photocathode material, which then emits electrons via the photoelectric effect. The number of these electrons, called photoelectrons (PE), produced for a single photon varies for each PMT and thus must be calibrated. Because the number of scintillation photons produced depends on the energy deposited (Eq. 2.2), we are able to reconstruct the recoil energy from the S1 signal. Additionally, because electron recoils are more likely to cause ionization, electron recoil events tend to have much larger S2 signals relative to S1 than do nuclear recoils, making the ratio of S2 to S1 another metric for event discrimination. This effect is enhanced in dual-phase TPCs: given the lower density of electron recoil LETs, due to the applied electric field in TPCs the ionization electrons they produce are less likely to recombine, preventing them from contributing to the S1 signal but leaving them free to increase S2. While this metric is of critical importance in liquid xenon detectors, which have a small difference between the lifetimes of the singlet and triplet state (3 ns and 27 ns, respectively [18]), for liquid argon the background rejection based on S1 alone is typically sufficient for WIMP searches.

2.4 Underground Argon

A drawback to the use of natural argon is the presence of ^{39}Ar, a β emitter formed from cosmic ray activation in the atmosphere. With an activity of 1 Bq/kg, this limits the size and sensitivity of liquid argon detectors, in spite of the excellent background rejection power. Because it has a half-life of only 269 years, argon which has been shielded from cosmic ray activation, such as that sourced from underground, should be depleted of ^{39}Ar. However, because ^{39}Ar can also be produced from neutron capture on ^{39}K, it is necessary to source argon from an underground location which has a low free neutron flux [37]. Such a location was found in Cortez, Colorado, at the site of the Kinder Morgan Doe CO_2 extraction facility. The underground argon at this location has an ^{39}Ar concentration which was measured initially to have an upper level of 0.65% that of atmospheric argon [38]. After employing it for use in DarkSide-50, the levels of residual ^{39}Ar have been precisely measured to be reduced by a factor of $(1.4 \pm 0.2) \times 10^3$ relative to atmospheric argon [39].

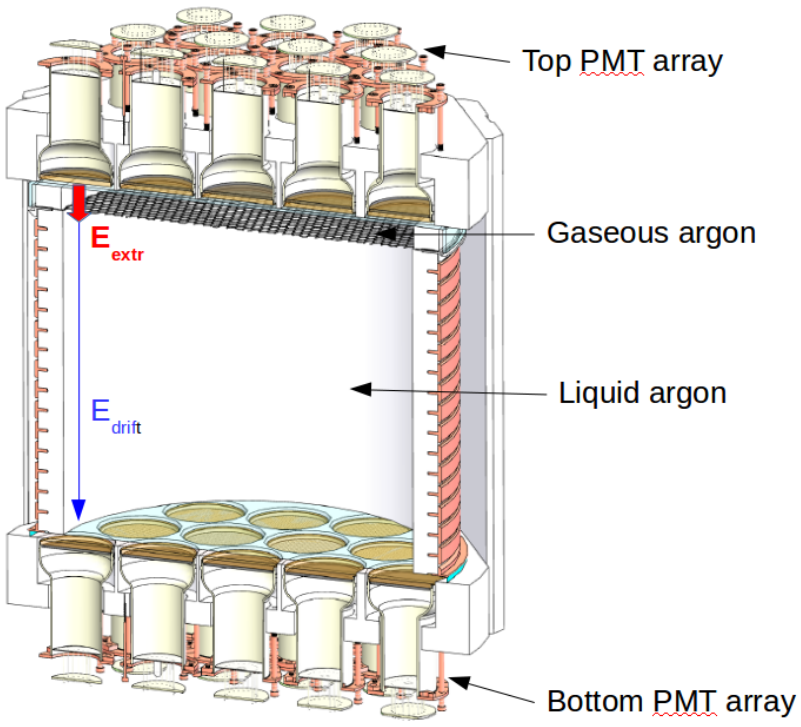

Figure 2.2: Cross section of the DarkSide-50 time projection chamber (TPC).

CHAPTER 3
DARKSIDE-50

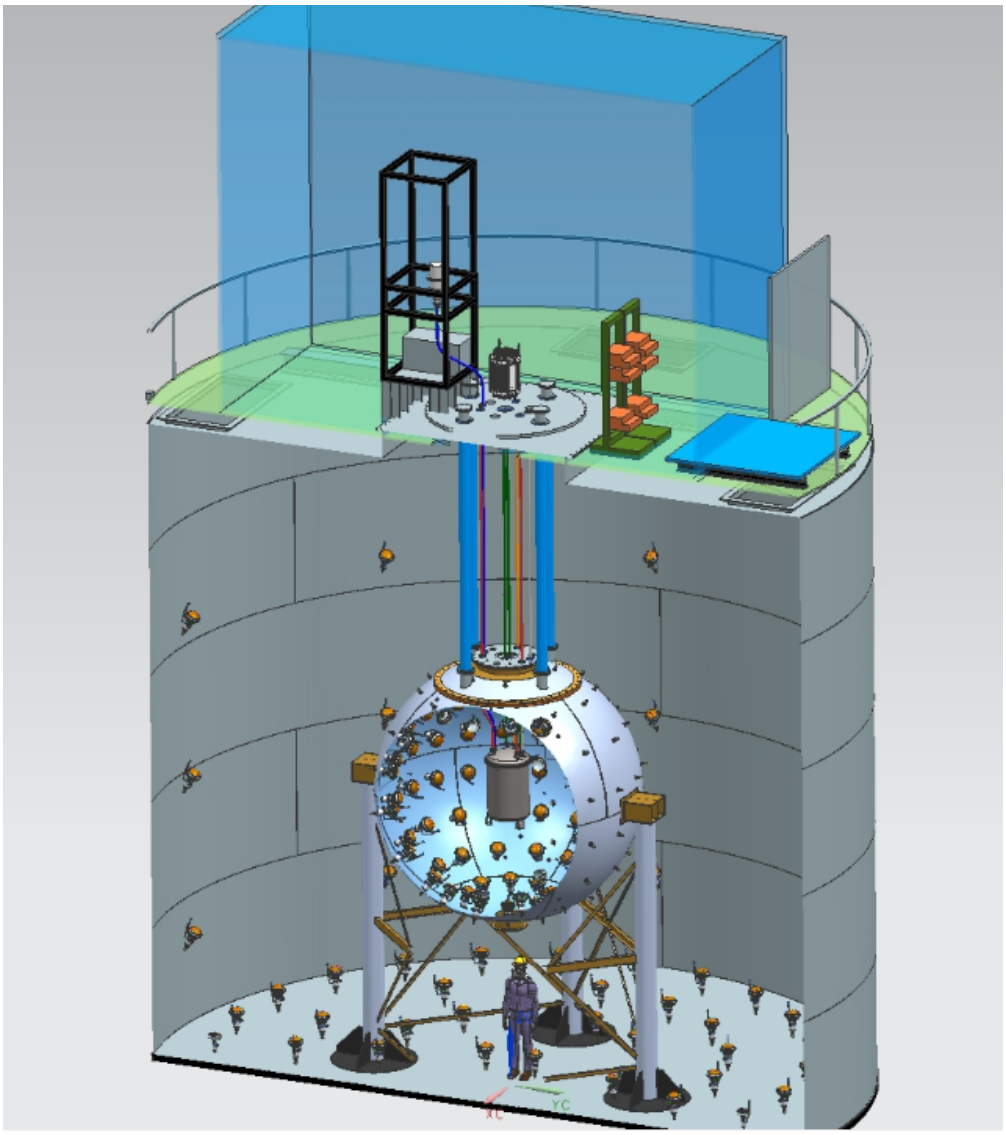

Figure 3.1: A cross sectional view of the DarkSide-50 experiment. The TPC is housed within the stainless steel cryostat in the center, surrounded by the LSV, which is in turn inside the WCV. On top of the detectors is the clean room, CRH, which houses the detector electronics.

The DarkSide-50 direct dark matter detector is part of a phased dark matter program which began with DarkSide-10, a prototype liquid argon TPC constructed at Princeton in 2010 [40]. The DarkSide-10 detector contained an active volume of 10 kg of liquid argon, observed by two arrays of 7 PMTs top and bottom. It demonstrated several key requirements of liquid argon TPCs. In

particular, an excellent light yield was measured at an average of nearly 9 PE/keV$_{ee}$ [41].

DarkSide-50 is the first detector in the DarkSide program with physics reach. Located at the Italian underground laboratory, Laboratori Nazionali del Gran Sasso (LNGS), DarkSide-50 consists of a liquid argon TPC nested within a liquid scintillator active neutron veto (LSV), which is in turn inside a water Cherenkov muon veto (WCV) (see Figure 3.1). Each of these detectors are described in more detail in the following sections.

Figure 3.2: Photograph of the DarkSide-50 TPC prior to palcement inside the cryostat.

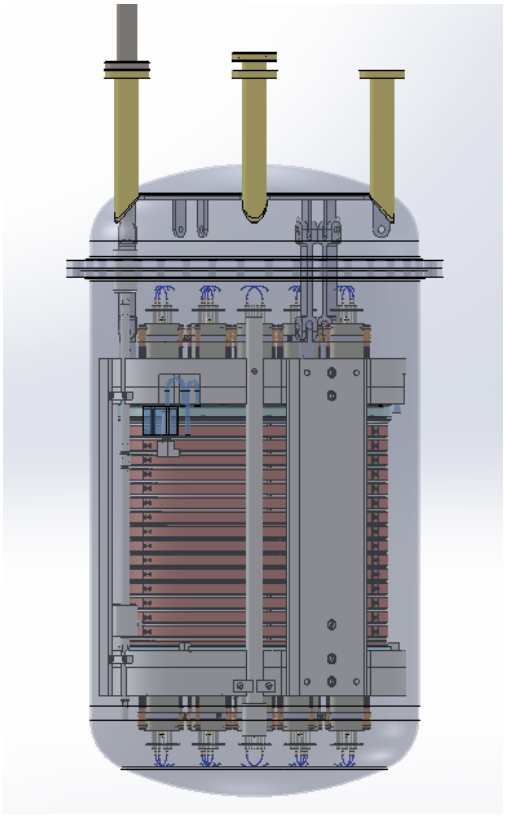

Figure 3.3: Conceptual drawing of the TPC inside the inner cryostat volume.

3.1 Dual-Phase LAr TPC

The DarkSide-50 TPC contains an active volume of 50 kg of liquid argon (150 kg total liquid argon) viewed by two arrays of 19 R11065 Hamamatsu PMTs top and bottom, arranged in a hexagonal pattern. In order to prevent the PMTs from sparking in the argon gas, they are fully submerged in the LAr; this argon is outside the active volume. The TPC body is a solid Teflon (PTFE) cylinder 36 cm in diameter and 36 cm in height, encircled by copper rings which facilitate the electric drift field (Figure 3.2). The active volume of LAr extends to the full height of this cylinder, 36 cm, and is topped by a 1 cm thick gaseous argon layer. The TPC is encased in a double-walled stainless

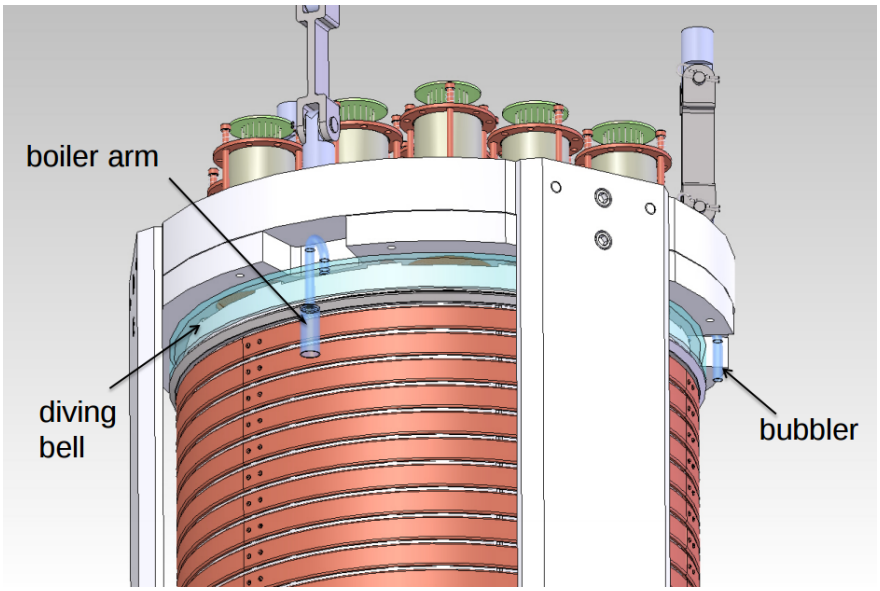

Figure 3.4: The diving bell at the top of the TPC active volume, which contains the gaseous argon layer.

steel cryostat (Figure 3.3). The space between the inner and outer cryostat walls, each 5 mm thick, is filled with Mylar multilayer insulation and evacuated to maintain the interior at liquid argon temperatures (less than 87 K). The PMT arrays view the active volume through fused silica windows, which, along with the cylinder walls, are coated with the wavelength shifter tetraphenyl-butadiene (TPB). The TPB coating absorbs the VUV photons from argon scintillation and re-emits in the visible spectrum peaked at 420 nm, in the range detectable by the PMTs. On average, for each VUV photon absorbed by the TPB, 1.2 visible photons are emitted [42]. In addition to the TPB, the fused silica windows are coated with indium tin oxide (ITO), a transparent conducting oxide. The top window extends into a diving bell structure which contains the layer of gaseous argon (Figure 3.4). Directly below the diving bell, approximately 5 mm below the liquid surface, is the stainless steel extraction grid. An electric drift field of 200 V/cm is maintained between the bottom ITO layer (the cathode, at ground) and the extraction grid. Between the grid and the anode (the top window ITO layer) is a stronger electric field at 2.8 kV/cm, which accelerates the drifted electrons out of the liquid phase and into the gas layer.

3.1.1 TPC Electronics and Data Aquisition

One of the greatest difficulties facing the development of DarkSide-50 was the operation of electrical components at both cryogenic and room temperatures. For example, the TPC PMTs are located within the cryostat, at 87 K. When operated at this temperature, the usual gain applied to the PMTs of greater than $\sim 10^6$ caused the PMTs to occasionally produce a large number of single

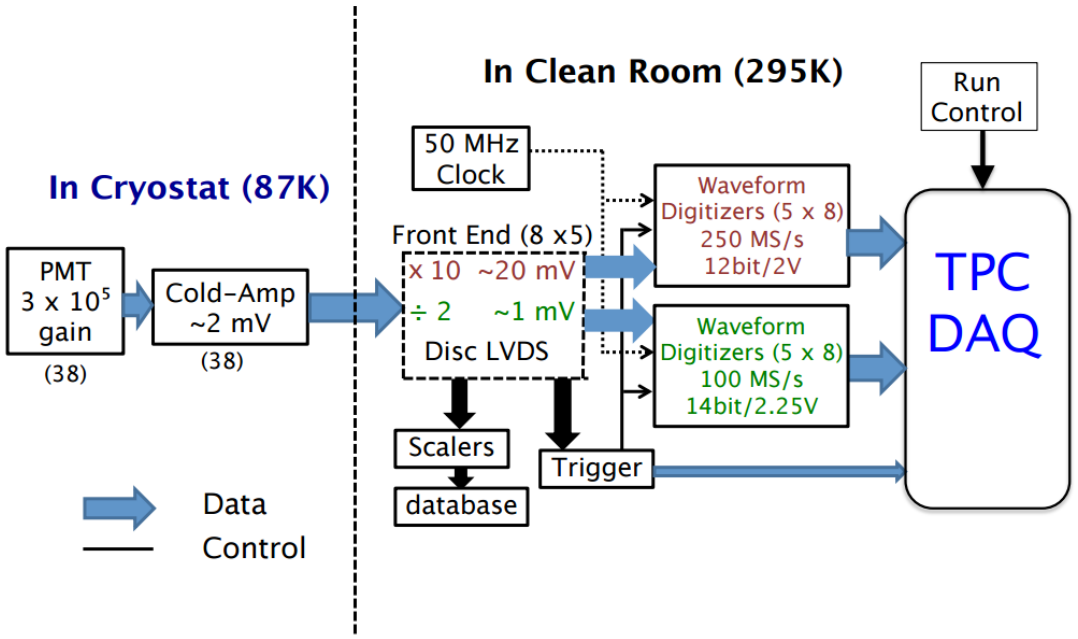

Figure 3.5: Schematic of the electronics chain for the TPC. [43]

photoelectron pulses. The high rate of these pulses, which could reach the MHz level, required the PMT high voltage to be powered down for more than 24 hours and made continuous data gathering impossible. This problem was solved by reducing the PMT gain to 3 x 10^5. The loss in gain was made up for by adding cyrogenic pre-amplifiers to each PMT. There additionally needed to be cabling which ran from the TPC (at 87 K) to the clean room (at room temperature) of over 6 m in length. These cables are protected from the liquid volumes they must traverse by being encased in flexible stainless steel tubing. The cables are also double-shielded in order to reduce pick-up noise. All components are chosen to have the minimum amount of radiation possible.

The cables running from the TPC connect to the front end module, which produces an amplified (x10) signal, a reduced (x0.5) signal, and two time-over-threshold LVDS outputs which are used for the trigger and to monitor the PMT rates.

The trigger is a majority logic trigger, which requires a preset number of channels to produce a signal within 100 ns. During the AAr campaign, which had a high rate in the TPC due to the ^{39}Ar background, the majority threshold was set to 3. Also during this time, a so-called G2-trigger was employed to reduce the rate of events recorded which are beyond the WIMP region of interest but which are still produced in large number by ^{39}Ar. Once the majority trigger is tripped, the G2-trigger counts the hits from all PMTs within a 5 μs time window. If the total of these hits, called the trigger digital sum, or TDS, is between 360 and 1500, a prescale of 33 is applied to the event, meaning that only 1 out of 33 events in this range are recorded. Variations of this trigger

were also used during various calibration campaigns (see Section 6.3). Upon replacing the AAr for UAr, the rate in the TPC dropped from about 50 Hz to 1.5 Hz. As a result, the majority threshold was reduced to 2, and the G2-trigger was no longer used.

The amplified signal is sent to 12-bit, 5 x 250 MHz CAEN 1720 digitizers, while the reduced signal is sent to 14-bit, 5 x 100 MHz CAEN 1724 digitizers. The 1720 digitizers are effective for the energies associated with the WIMP search region, while the 1724 digitizers allow for an extension of the dynamic range, up to 10,000 PE. The data acquisition gate is set to 440 μs, with an inhibit window of 810 μs to prevent event pile-up.

3.1.2 TPC Event Reconstruction

The DarkSide-50 event reconstruction software, called DarkArt, is based on the *art* DAQ reconstruction framework produced by Fermi National Laboratory. The first step in the reconstruction begins with the converter module, which produces the raw waveforms for each PMT channel, as well as event level information such as event ID and trigger time, and channel level information such as channel ID, sample rate and whether the channel digitizers were saturated.

Each raw waveform is then sent to the baseline finder module. In DarkSide-50, the waveform baselines cannot be assumed to be constant in time. The baseline finder module, therefore, computes the baseline as a moving average. First, the maximum amplitude in the pre-trigger window is found. This value is used to define the maximum and minimum (as the negative of the maximum amplitude) of the allowed baseline vertical values: values which are outside this range are assumed to be due to the signal pulse. The module thereby separates the baseline into signal and non-signal regions. The baseline is followed, sample by sample, until a point is reached where there are a user-defined number of samples before and after which are in the baseline (non-signal) regime. Here, the average is calculated. This continues for each sample point, until a value outside of the $\pm$maximum amplitude is found, and is therefore the beginning of a signal or pulse region. The algorithm then ceases to calculate the average until the sample is once again determined to be part of the baseline. Under the signal region, the baseline is linearly interpolated. Thus, the majority of integrated electronics noise occurs in the pulse region.

Once the baseline has been calculated on all channels, the sum channel module combines the waveforms from each channel into a single waveform. To do this, each channel waveform is first scaled by its single photoelectron response, determined at regular interval by laser calibration (see Section 4.1). The waveforms are then zero-suppressed, meaning that all values above 0.1 PE are set to zero (note that the signal amplitudes are negative). Finally, each are added to create the final, summed waveform.

At this point, only two things remain: to first identify each pulse, and then to calculate the relevant quantities, such as the integrated charge. The pulse finder module identifies each pulse by first doing a broad search, looking for any 2 μs region which has at least 5 PE above baseline (or,

to be precise, below baseline, as the signal amplitudes are negative, as noted above). Within each 2 μs region where a pulse is located, the start of the pulse is identified by the region where a 0.3 PE threshold is met. The end of the pulse is identified as the location where the signal returns to baseline, or where another pulse begins, in the case of pile-up.

With the pulses for each event identified, the relevant quantities can be calculated on each. These are the total number of photoelectrons in each pulse, the value of f_{90}, which is the ratio of the integral of light in the first 90 ns of the pulse to the total pulse integral, the number of photoelectrons in the first 7 μs of the pulse, and the number of photoelectrons in the first 30 μs of the pulse. As no assumptions have been made about the nature of any pulses, these values are calculated for all pulses, as well as on all individual channels. During analysis, the 7 μs integral is used to determine the total S1 signal, while the 30 μs integral yields the S2 total signal.

3.2 Outer Detector Veto System

Given that any recoiling particle in the TPC will produce a scintillation signal, a convincing claim of dark matter detection requires a clear understanding of detector backgrounds and robust mitigation techniques. In DarkSide-50, both passive shielding and active vetoing are employed to produce the only direct dark matter experiment to date running background free [39]. The underground location at LNGS provides 3800 meters water equivalent shielding from cosmogenic muons, resulting in a flux reduction at the level of $\sim 10^6$ relative to the Earth's surface [44]. The remaining muon flux, as well as radiation from the rock walls and detector elements, are blocked or tagged by the nested active veto system, or outer detectors, described below.

3.2.1 Liquid Scintillator Neutron Veto

Although liquid argon TPCs have excellent discrimination between nuclear recoil events caused by α particles, neutrons, or potential WIMPs and electron recoil events caused by photons or electrons, they lack the ability to discriminate between different types of nuclear recoil events. Thus, particles which cause these events form the most dangerous class of backgrounds.

α particles most frequently originate in the decay chain of radon, which can be introduced from the detector materials and the rock walls underground. The level of this contamination can be greatly reduced by radon-free clean room detector assembly and use of radiopure materials. Additionally, as alpha particles are not deeply penetrating, choosing a fiducial volume within the TPC which excludes the region closest to the detector walls removes the residual alpha background.

Neutrons, therefore, present the greatest challenge to WIMP direct detection. Sources include radiogenic neutrons produced from (α, n) reactions and spontaneous fission, and cosmogenic neutrons formed via spallation. Passive shielding can reduce the rate of neutrons reaching the inner detector, but cannot eliminate them: cosmogenic neutrons are highly energetic and can penetrate

through vast amounts of shielding material, and radiogenic neutrons from detector components have already bypassed any such shielding at the moment of their production. The solution, then, is to actively detect and veto these events.

The DarkSide-50 Liquid Scintillator Veto (LSV) is a 4 m diameter stainless steel sphere equipped with 110 PMTs and filled with the organic liquid scintillator pseudocumene (Figure 3.6). In pure pseudocumene, neutrons are attenuated by scattering off hydrogen, leading to their eventual capture after approximately 250 μs [45]. This capture produces a 2.2 MeV gamma which can be observed by the PMTs. The pseudocumene in DarkSide-50 is further doped with 5% by volume trimethylborate (TPB). Boron has a large neutron capture cross section of 3837 b (for comparison, the neutron capture cross section on hydrogen is 0.330 b), and reduces the neutron capture time to approximately 2.3 μs. Neutrons are captured on boron via one of two channels:

$$\begin{aligned} {}^{10}B + n &\longrightarrow {}^{7}Li + \alpha \text{ (1.78 MeV)} && [6.4\%] \\ {}^{10}B + n &\longrightarrow {}^{7}Li^{*} + \alpha \text{ (1.47 MeV)} && \\ {}^{7}Li^{*} &\longrightarrow {}^{7}Li + \gamma \text{ (0.48 MeV)} && [93.6\%] \end{aligned}$$

Both capture channels produce energetic reaction products for veto detection. The majority of captures (93.6%) yield a 478 keV gamma. However, 6.4% of captures produce only an α particle, which, while energetic, is heavily quenched. The detection of the α-only channel is, therefore, the critical factor for a highly efficient neutron veto. In the LSV, these events produce a signal of $\sim$30 PE, well above the detection threshold of a few PE (see also Section 4.6) [46].

Within the LSV, three fish-eye lens CCD cameras are installed. While it is not possible to operate these while the veto PMTs are on, they provide an invaluable cross check of the source position during calibrations (see Chapter 4).

3.2.2 Water Cherenkov Muon Veto

The Water Cherenkov Veto (WCV) is a cylinder 10 m in height and 11 m in diameter, originally used as the Borexino Counting Facility. Filled with approximately 1000 tonnes of ultra-pure water, the WCV provides a highly effective passive shield for energetic neutrons and muons. The volume is monitored by 80 PMTs, which detect Cherenkov radiation from cosmogenic backgrounds before they can reach the LSV or TPC (Figure 3.7).

3.2.3 Outer Detector Electronics and Data Aquisition

While the TPC has substantial requirements for its DAQ system in pulse time distribution and energy reconstruction, the primary requirement for the outer vetoes is event detection, along with high timing precision. Muons crossing the WCV produce huge signals, easily separable from other background noise. The large reflectivity of the Lumirror covering both the WCV and LSV means

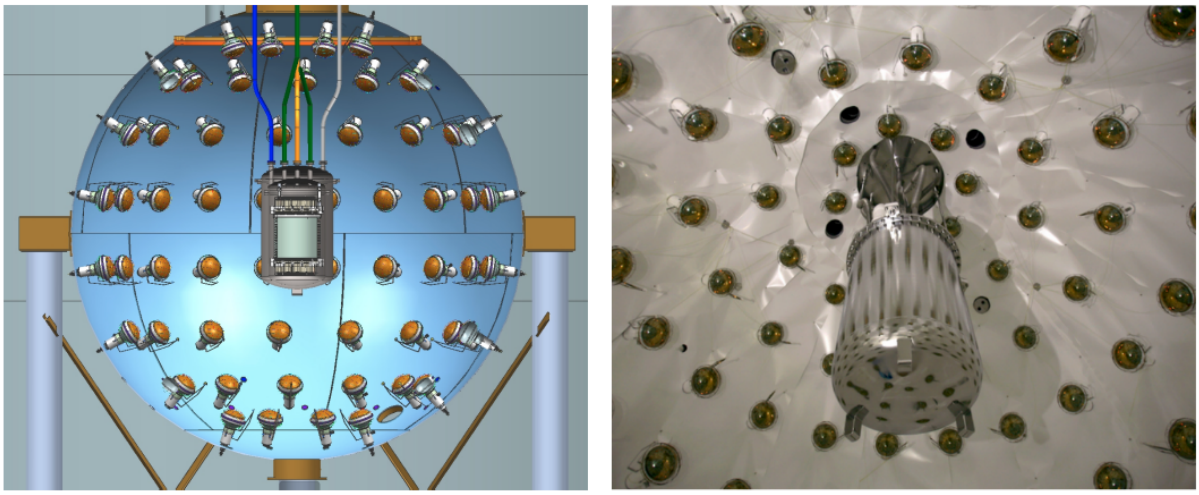

Figure 3.6: *Left:* Conceptual drawing of the TPC within the LSV. *Right:* Photograph of the TPC cryostat inside the LSV, prior to filling with liquid scintillator.

most events are seen by all PMTs. In the LSV, the only exception is in the case that an event occurs directly in front of a single PMT, and thus most of the light will be detected there.

The output signal from all 190 outer detector PMTs are amplified x10 and digitized by National Instruments PXIe-5162 digitizers; the unamplified signal is also recorded in order to extend the dynamic range. There are 56 digitizers for the LSV, and 40 for the WCV. Each waveform is zero-suppressed by the ODAQ in order to reduce the data size, with parameters set by the user. The threshold amplitude is usually set to 0.25 times the amplitude for a single photoelectron pulse. Additionally, 20 samples before and after each above-threshold pulse are recorded.

The trigger may be operated in one of two modes: either on the LSV itself, regardless of the state of the TPC trigger (self-trigger mode), or on the TPC, regardless of the state of the LSV (slave-trigger mode). For standard data taking during a WIMP search, the outer detectors are triggered by the TPC, with a data acquisition window of 200 μs.

3.2.4 Outer Detector Event Reconstruction

Like the TPC, the outer detector reconstruction software, DarkArtOD, is based on *art*. A clustering algorithm identifies each pulse via a top-down iterative procedure, starting at the position of the sum waveform maximum amplitude. The waveform region before and after this position is scanned in order to identify the pulse (cluster) start and end time. Each cluster is defined to include all pulses with less than 20 ns separation between them. Once a 20 ns gap is found, signaling the boundary of the largest cluster, the next highest peak position is identified, and the procedure repeats until the maximum amplitude found is less than 2 PE. The clustering algorithm is demonstrated in Figure 3.8.

Figure 3.7: Photograph of the interior of the WCV, prior to being filled with ultra pure water. The LSV is in the center. All surfaces are covered with highly reflective Limirror.

In addition to integrating the charge in all clusters to obtain the total event energy, the charge is integrated in temporal regions of interest (ROIs) specific to the appearance or capture of neutrons in the LSV. This includes the 300 ns around the TPC prompt signal, in which the neutron thermalization signal may appear, and the time between the TPC prompt and the end of the acquisition window, in which the neutron capture signal may be detected.

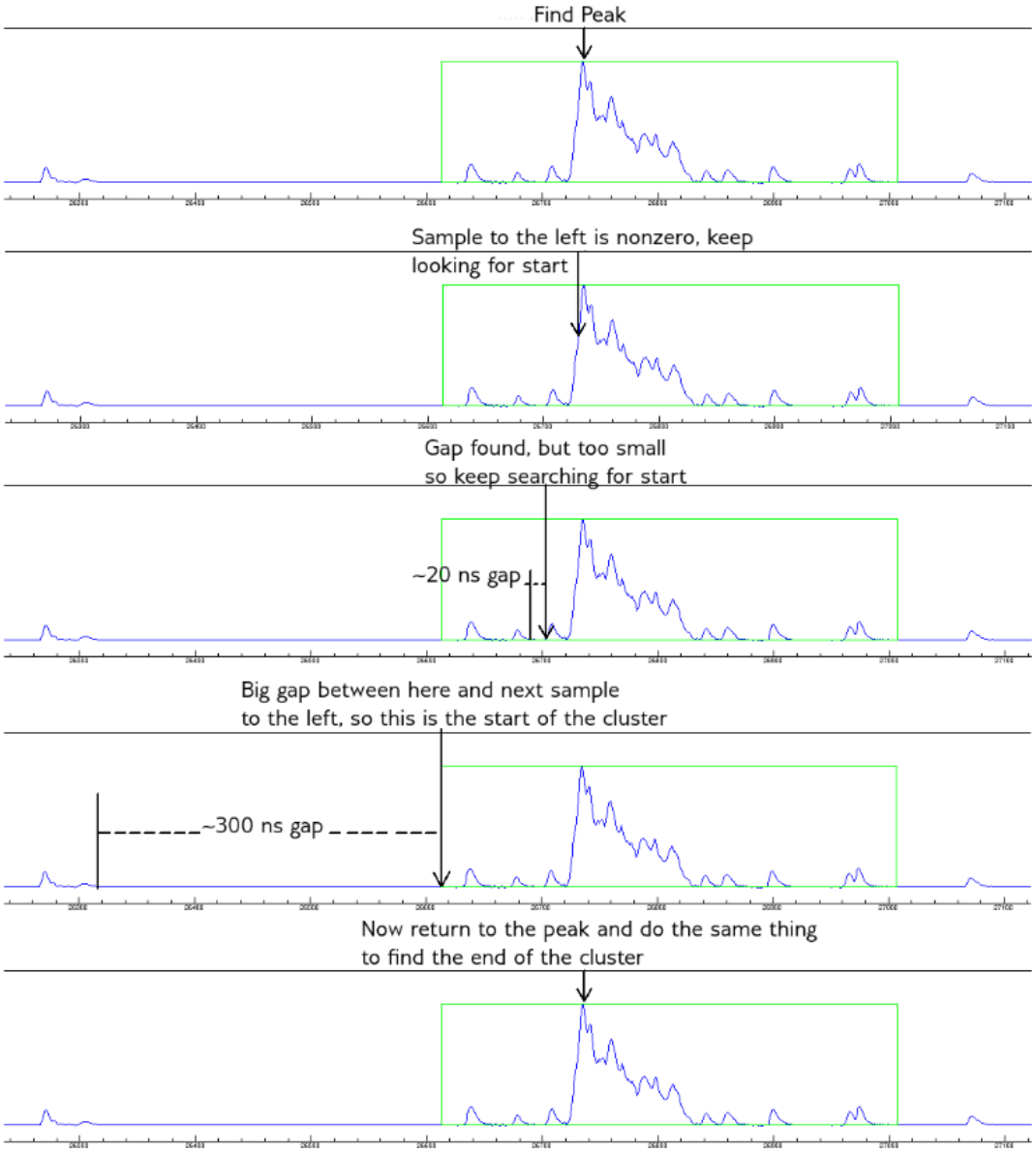

Figure 3.8: Example of the cluster finding algorithm in the LSV event reconstruction (see text) [46].

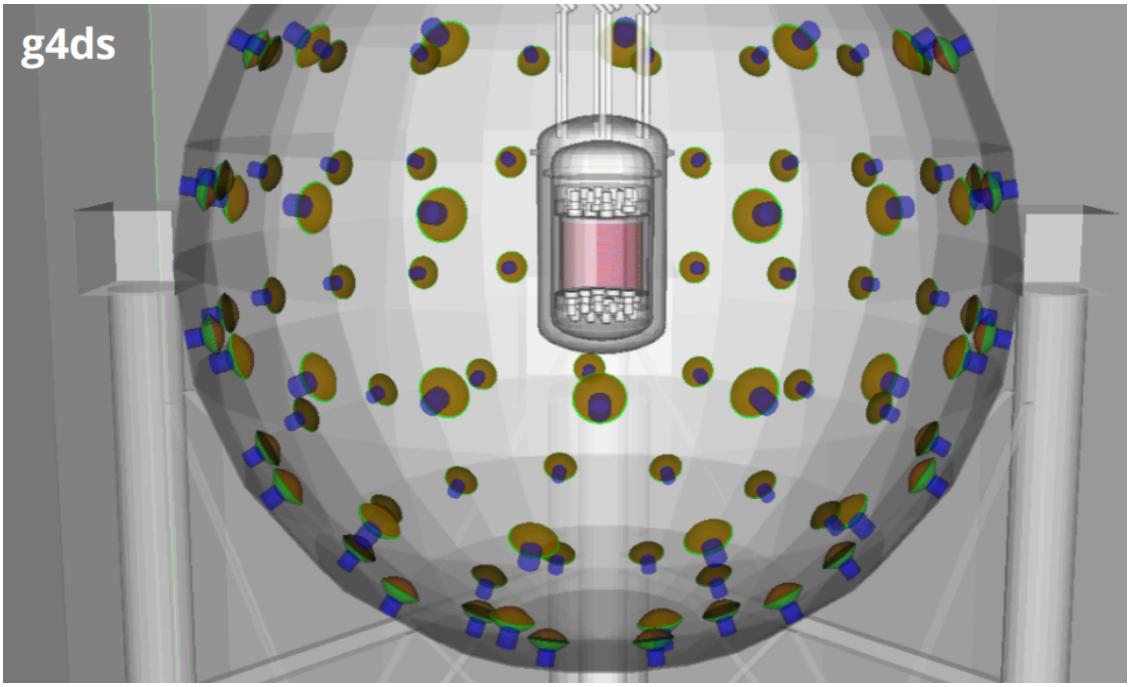

Figure 3.9: The geometry of the DarkSide-50 detectors, as simulated in g4ds [48].

3.3 g4ds: The DarkSide-50 Monte Carlo

The DarkSide-50 Monte Carlo package, g4ds, is based on the Geant4 particle simulation platform developed at CERN. g4ds describes the full geometry of all three detectors: the TPC, LSV and WCV (Figure 3.9). The full optics of particle interactions are implemented and tuned on DarkSide-50 data. Additionally, the energy response in the TPC is modeled. The recombination probability for ionized electrons in LAr, modeled as a function of recoil energy, assumes a value of 19.5 eV for the average energy to produce a single scintillation photon, W_{ph}, and 0.21 for the ratio of the number of excited to ionized atoms produced, N_{ex}/N_i (see Section 2.2). The energy and recombination model has been validated against gamma source calibrations, such as ^{57}Co and ^{133}Ba (see Figure 3.10).

The quenching of nuclear relative to electron recoils follows the model introduced by Mei, et al., which combines Lindhard's theory of scintillation in liquid noble elements and Birk's saturation law for scintillation quenching [47]. Excellent agreement between the simulated nuclear recoil energy spectra in the TPC produced by g4ds and that from AmBe calibration data is shown (see Figure 3.11).

In addition to modeling energy deposits and optics, the DarkSide-50 electronics may also be simulated, allowing for analysis of the full reconstruction chain [48].

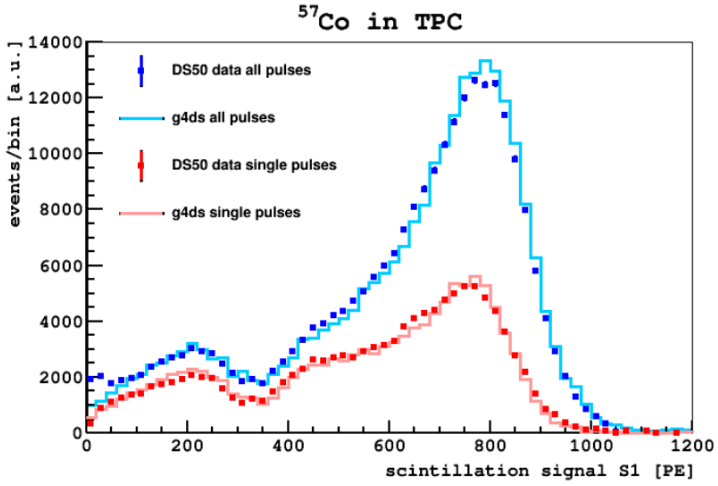

Figure 3.10: Comparison between the S1 spectrum in the TPC from calibration with ^{57}Co and that produced by g4ds simulation [49]. Excellent agreement has been achieved for both single and multiple pulse events.

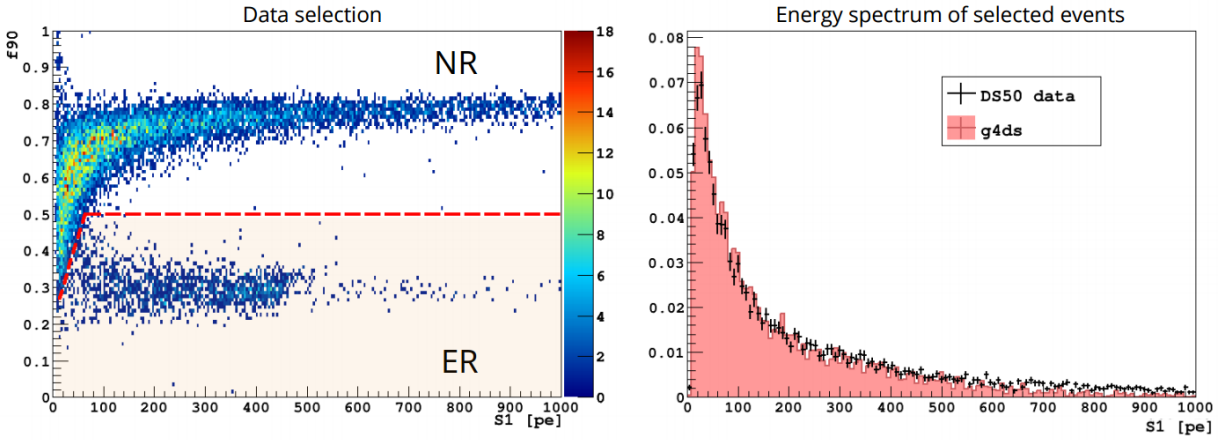

Figure 3.11: *Left:* Nuclear recoils from AmBe calibration data, after the application of event selection criteria which removed almost all electron recoil events (see Section 6.2). The remaining electron recoils (below the red dashed line) are cut away in order to select only nuclear recoil events for data-Monte Carlo comparison. *Right:* Comparison of the energy spectrum of AmBe nuclear recoils in the TPC simulated by g4ds with the calibration data shown. [48]

CHAPTER 4
CALIBRATION OF DS-50

4.1 Calibration Requirements

DarkSide-50 has three nested, active detectors, all of which require calibration. In the case of the WCV, calibration requirements are limited to the SPE response of the PMTs, which is calibrated by a dedicated laser system. The LSV and TPC are similarly outfitted with their own laser calibration systems, which give regular measures of the PMT gain. Both the LSV and TPC further require their light yield/energy response to be thoroughly measured at a range of energies. The LSV additionally requires verification of its neutron vetoing efficiency, while in the TPC, characterization of pulse shape discrimination is necessary.

The light yield may be calibrated both through the use of spectral features in the intrinsic background and the introduction of radioactive sources with known energies. Figure 4.1 shows the photoelectron spectrum in the LSV, with two of the peaks used to measure the light yield marked. Table 4.1 shows the scintillator light yield values determined from this intrinsic background. These measurements, which are uniformly distributed in the detector, are complimentary to point source measurements from radioactive sources. In the TPC, ^{83m}Kr is injected into the LAr. With a half life of 1.83 hours, the introduced radiation decays away with no lasting impact to the detector background, while allowing for a full volume calibration of the light yield. ^{83m}Kr produces two low energy sequential lines at 32.1 and 9.4 keV, separated by 154 ns. The separate peaks are not resolvable, and thus form a single calibration line at 41.6 keV.

The endpoint energy of the ^{39}Ar background in the LAr may also be used as a measure of the light yield. However, better use of these events is made by studies of pulse shape discrimination and X-Y position reconstruction. The single-sited β decays, occurring uniformly throughout the active volume and at a high rate in AAr, are ideally suited for both of these purposes.

Additional calibration needs must be met by radioactive gamma and neutron sources. Such sources have relatively long half lives, and must be safely inserted into or near the detector and reliably removed. A dedicated system was built for this purpose, and is described in the following section.

4.2 CALibration Insertion System (CALIS)

The CALibration Insertion System (CALIS) was designed and built by engineer Cary Kendziora at Fermi National Laboratory, in collaboration with the DarkSide members at the University of Hawaii, during the spring and summer of 2014. After extensive testing at both FNAL and LNGS by the Hawaii group, CALIS was installed in October, 2014. The system resides in the CRH clean

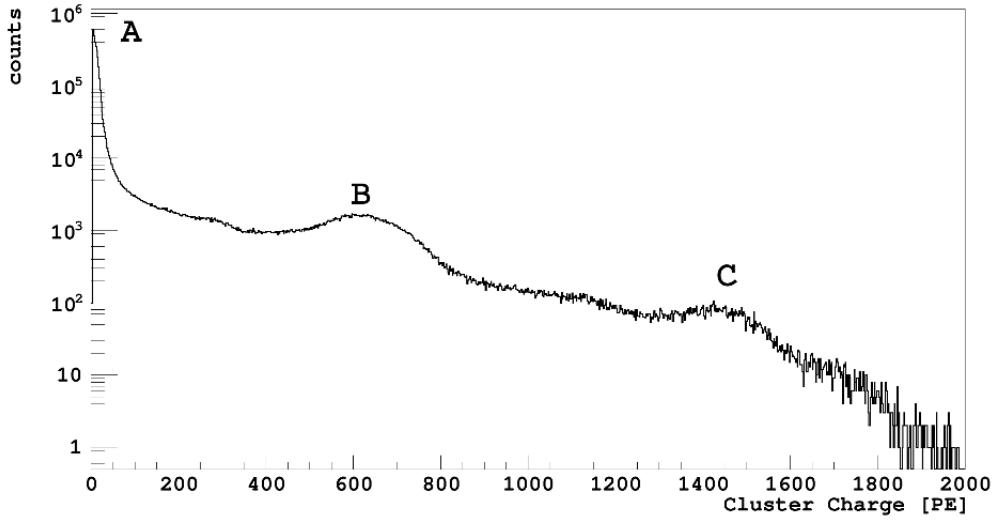

Figure 4.1: Energy spectrum of the LSV in photoelectrons. Region A is from low energy afterpulsing, Region B is due to ^{60}Co (from the stainless steel of the cryostat and LSV sphere), and Region C is the peak due to ^{208}Tl (naturally present in iron, and thus also from the stainless steel) [46].

Isotope	Decay Mode	Energy [keV]	Light Yield [PE/keV]
^{14}C	β^-	156 (endpoint)	0.561 ± 0.013
^{60}Co	γ	1173	0.524 ± 0.002
^{60}Co	γ	1332	0.544 ± 0.003
^{208}Tl	γ	2514	0.551 ± 0.002

Table 4.1: Light yields measured from 4 spectral peaks in the LSV intrinsic background, shown in Figure 4.1 [46].

room above the DarkSide-50 detectors, where it is mounted on a gate valve which allows access to the LSV. Calibration sources are lowered through an organ pipe (access port) into the LSV, where they may be placed close to the TPC or rotated away, into the main scintillator volume (see Figures 4.2, 4.3 and 4.4).

4.2.1 System Design

A schematic of CALIS is shown in Figure 4.5, along with a photograph for comparison. The insertion system is comprised of three parts, which may be separated for shipment or storage: a lower assembly, an upper assembly, and the source deployment system. The lower assembly consists of the base, which is mounted on the gate valve. Directly above the lower assembly is the view port, which allows access to the source holder for source exchange. This is at the bottom of the upper assembly, which also houses the stepper motor and cable spools, shown in Figure 4.6. The source deployment system is shown in Figure 4.4. This portion of CALIS is referred to as the "PIG",

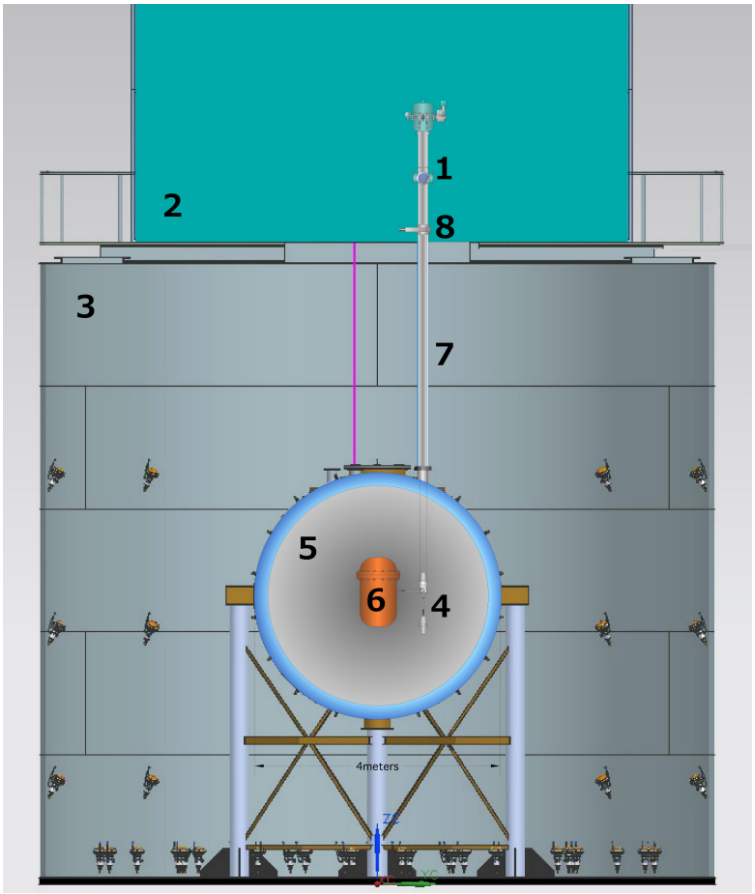

Figure 4.2: Diagram of CALIS inside the LSV, next to the TPC with the source arm articulated. The noted points correspond to: (1) CALIS; (2) the clean room (CRH); (3) the WCV; (4) the PIG (source deployment system); (5) the LSV; (6) the TPC; (7) the organ pipe providing access to the LSV (note that there are four such access ports, but only one is shown); and (8) the gate valve, upon which CALIS is mounted.

an acronym for Pipeline Inspection Gauge, in reference to a device which is used in pipelines for cleaning and maintenance. The conical sections of the PIG add weight for stability and are intended to allow for smooth motion through the organ pipe.

The organ pipe remains closed at all times, except during calibration. Prior to opening the gate valve at the beginning of a campaign, the CALIS enclosure is evacuated, filled with nitrogen, and then evacuated again. This process, called "pump and purge", is repeated for several cycles in order to remove all oxygen and humidity from the enclosure due to their quenching effect on the scintillator. At the completion of a calibration, prior to opening the view port for source removal, the pump and purge process is performed again, this time with the goal of removing all trace of scintillator, for the safety of both the human operators and the sensitive electronic equipment. This is especially important due to the presence of ^{10}B, which reacts with any moisture in the air to

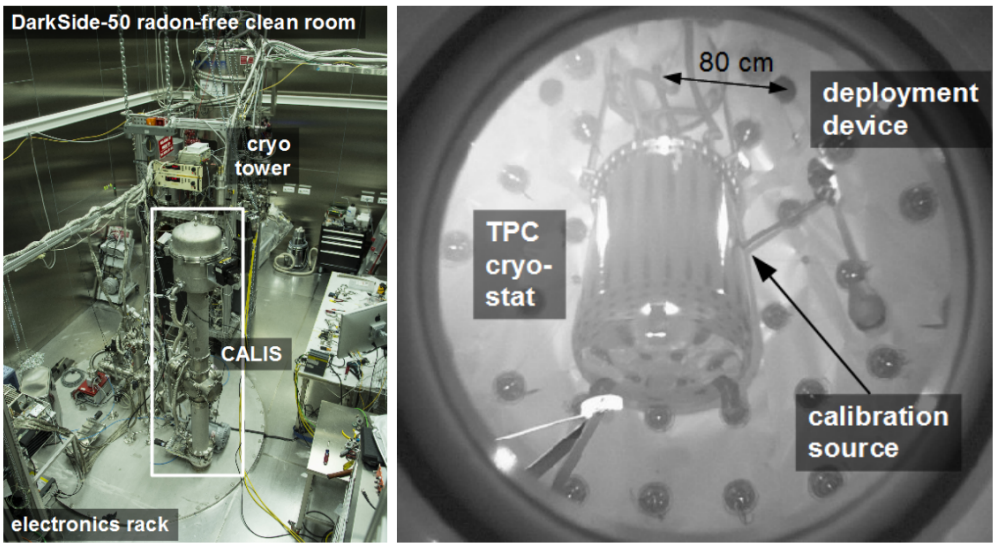

Figure 4.3: *Left:* CALIS installed inside CRH. *Right:* The PIG, or source deployment device, inside the LSV. This image was taken with one of the CCD cameras which are installed inside the veto. Here the source arm is partially articulated.

form boric acid.

Vertical motion is achieved via the stepper motor, which is controlled by a LabView interface on a dedicated laptop in the clean room. The stepper motor has an absolute encoder which retains the PIG position information, even in the event of power failure. A single cable is wound on two spools in the upper housing (see Figure 4.6). The PIG is lowered by rotating both spools simultaneously. A hand wheel manually controls the rotation of a single spool. By rotating only one spool, the source arm is both articulated and lifted a short distance vertically. The arm may be articulated to any angle between 0° and 90°. Once the arm has been articulated, vertical motion is prevented by a limit switch which cuts the power to the motor. This prevents the PIG from being retracted into the organ pipe with the arm extended. The azimuthal position of the source is controlled by manually rotating the upper assemby (see Figure 4.8).

4.2.2 FNAL: Testing

The operation of CALIS was tested in August and September, 2014, at Fermi National Laboratory in Batavia, Illinois. The goal of this testing period was to establish the stability of the system in terms of source positioning, minimal lateral motion during deployment, and functionality of safety features. In order to deploy CALIS to its full length, the tests were performed in the Wide Band Lab, which has a high bay platform to which the system was mounted, allowing the PIG to be lowered through a hole in the platform. The results of the testing are detailed below.

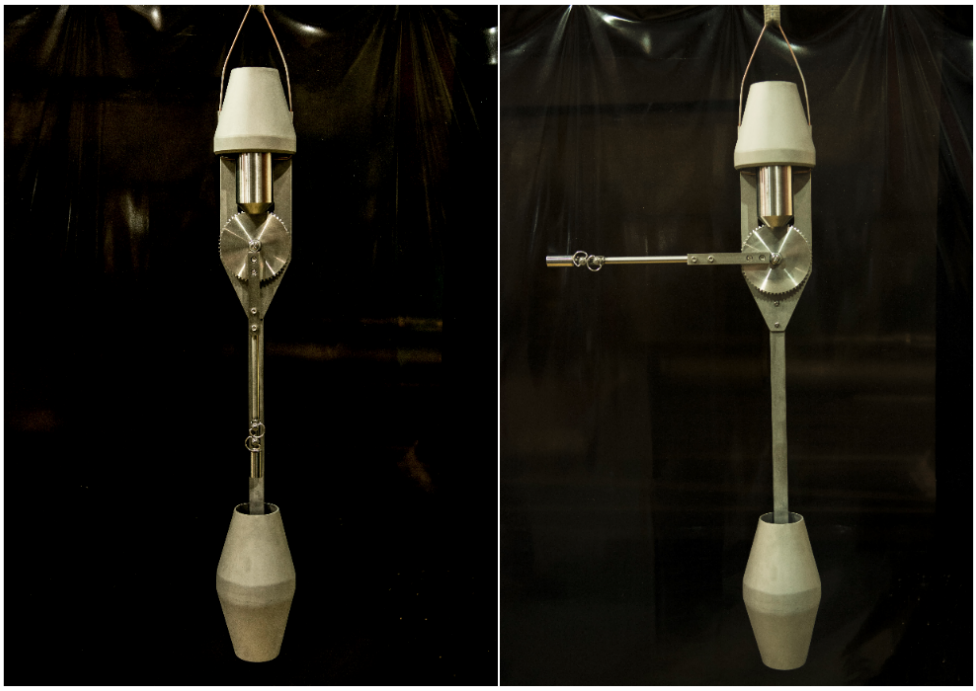

Figure 4.4: The source deployment system, called the PIG, with the source arm vertical (left) and articulated to horizontal (right). The source arm showed in this picture is 40.31 cm, however the arm used in deployments is 62.0 cm in order to put the source holder in contact with the cryostat.

Z Position Accuracy and Repeatability

Because the motor steps are given in arbitrary units, it was necessary to calibrate the relation between step number and vertical distance. First, the PIG was deployed to its lowest position, and the bottom was covered with tape. The surface of the tape formed a target on which a laser ranger was directed. After first using the laser ranger to measure the distance to this bottom position, the PIG was retracted, stopping at regular intervals to record the vertical distance. After arriving at the home position, the PIG was deployed again to the same motor step positions, and the vertical distance recorded. This process was repeated for a total of 31 trials, each trial consisting of either sending the PIG to its lowest point or returning it to the home position. Such a large number of trials was conducted in order to detect any slipping in the cables, which may be small for each trial but accumulate over time.

The Z-positioning was found to be extremely consistent, with no measurable slipping. All vertical measurements agreed to within $\sim$2 mm, consistent with the level of unevenness in the tape surface.

Lateral Motion During Deployment and Articulation

The PIG is lowered by the motor stepper at very low speed (4 mm/s), barely visible to the naked eye. As a result, there is no discernible lateral movement during deployment. During articulation, however, the wheel is turned by hand, and can have some friction. Therefore, articulation which is performed too quickly will cause the PIG to swing. Depending on the vertical position at the time of articulation, this swinging could potentially cause the PIG to collide with a PMT in the veto, a situation which obviously must be avoided. In order to measure the magnitude of the lateral motion during articulation, a ruler was formed on a white backdrop and mounted behind the PIG on a mock up of the cryostat. Video recordings were then taken of the PIG during articulation and de-articulation. Analysis of the videos showed that the PIG swung approximately 1.5 cm. In air, about 2 minutes were required for the PIG to stop moving completely.

Articulation Accuracy and Repeatability

The repeatability of the articulation angle was tested by choosing two Z motor step positions, one at the center of the cryostat mock up and one at the full deployment length, and articulating the source arm until it was horizontal as determined by a level placed along it. The angle on the articulation wheel was then recorded. The vertical displacement of the PIG was also recorded when the arm was vertical prior to articulation, when the source arm was horizontal, and again after de-articulation.

It was found that the source arm did not return to a vertical position after de-articulation, but retained a small ($\sim 2^\circ$) angle, although the articulation wheel indicated a vertical position. Some investigation revealed that the articulation position is very sensitive to any stretch or tension which has accumulated in the cable. For this reason, it is necessary to deploy the PIG to its full length before positioning and articulation, in order to release any such tension.

Stability During Azimuthal Rotation

In order to check the stability of the system during azimuthal rotation, the PIG was deployed and articulated next to the cryostat mock up. The clamp at the base of the upper assembly must be loosened to allow the rotation; the position is then indicated by the ruler (see Figure 4.8).

Despite the significant weight of the upper assembly, the azimuthal rotation is smooth, with no jerking or sticking. The slow rotation did not induce swinging in the PIG.

Safety Features

The leak tightness of CALIS was verified with helium leak testing, both while the upper assembly is clamped tightly and when the clamp is loosened to allow for azimuthal rotation. This is especially

important due to the ^{10}B content of the scintillator. Additionally, the upper limit and arm retraction switch were both tested and found to operate consistently.

4.2.3 LNGS: Testing, Cleaning and Commissioning

After the arrival of CALIS at LNGS in October, 2014, it was again tested for position repeatability and characterization. These tests were performed in Hall C, prior to the cleaning and installation of CALIS in the clean room above the detectors.

Position Characterization

Because the cable winding (or unwinding) on the spool causes the radius to change, the relationship between motor step count and the physical location of the source in non-linear (see Figure 4.9). Additionally, this means that the hand wheel must be rotated by a different amount to fully articulate the source arm, depending on the vertical position. As the source arm is not visible to the operator while it is being deployed, both the Z position and hand wheel angle as a function of motor step count needed to be well characterized.

In order to measure the relevant values, the motor step counts which approximated the location of the full length of the cryostat were determined. For each motor step position, the vertical distance was measured, both before and after articulating the source arm to 90°, and the hand wheel angle noted. Particular attention was given to positions which would commonly be utilized during a calibration, such as those corresponding to the center of the TPC active volume and its vicinity.

Cleaning and Installation

Once the vertical and articulation positioning had been fully characterized, CALIS was disassembled and thoroughly cleaned, in preparation for clean room installation. Each component was first cleaned with detergent and rinsed with high purity water. The parts were then pickled with glycolic (2%) and formic (1%) acid at $80 - 90°$ C. After rinsing with high purity water, they then underwent passivation with a 4% solution of citric acid at $60 - 70°$ C, followed by an EDTA (1%) alkaline rinse. The last high purity water rinse continued until the conductivity was more than 17 MΩ/cm. Finally, all components were thoroughly dried with compressed nitrogen. In order to prevent contamination while transporting CALIS from the cleaning facility inside Hall C to CRH, it was partially pre-assembled and all parts double bagged. The full assembly was done inside CRH, and CALIS was mounted on the gate valve on October 19, 2014.

Pressure Stability

After installation, CALIS was first evacuated to again verify that it was properly sealed. Prior to opening the gate valve, the "pump and purge" procedure outlined in Section 4.2.1 was performed. CALIS was then given a slight over pressure relative to the pressure at the surface of the scintillator, in preparation for opening the gate valve. To ensure that there would be no pressure loss during azimuthal rotation, the ring clamp between the upper and lower assemblies was loosened, and the system rotated in each direction by several degrees. Finally, the ring clamp was re-tightened, and the gate valve was opened, while the pressure inside CALIS was closely monitored. At all points, CALIS was verified to be leak tight and pressure was maintained.

Source-less Deployment

The first deployment occurred without a source and with the veto PMTs off. The cover was left off of the viewport so that the motion of the PIG and the cables could be monitored. Once the PIG had cleared the organ pipe, its progress was recorded by CCD cameras installed inside the LSV. The PIG was deployed to its full length, and then positioned near the center of the TPC active volume, as determined by the previously characterized motor step count. The source arm was articulated to 90°, and azimuthally rotated. All positions were verified by CCD images and agreed with expectations.

Light Tightness

Before turning on the veto PMTs, it was necessary to verify that the system was light tight. To do this, the viewport cover was first put in place and secured, and a PMT close to the gate valve was selected for monitoring. Prior to opening the gate valve, the dark rate of the selected PMT was noted. The lights in CRH were then turned off, except for a red light flashlight. As the gate valve was opened, the dark rate of the selected PMT was carefully monitored. Finding no increase, the ring clamp between the upper and lower assemblies was loosened, and the upper assembly rotated to verify that this would not introduce a light leak. Finally, the lights were turned on, while monitoring the PMT rates, and the upper assembly again rotated. No increase in PMT rate was seen.

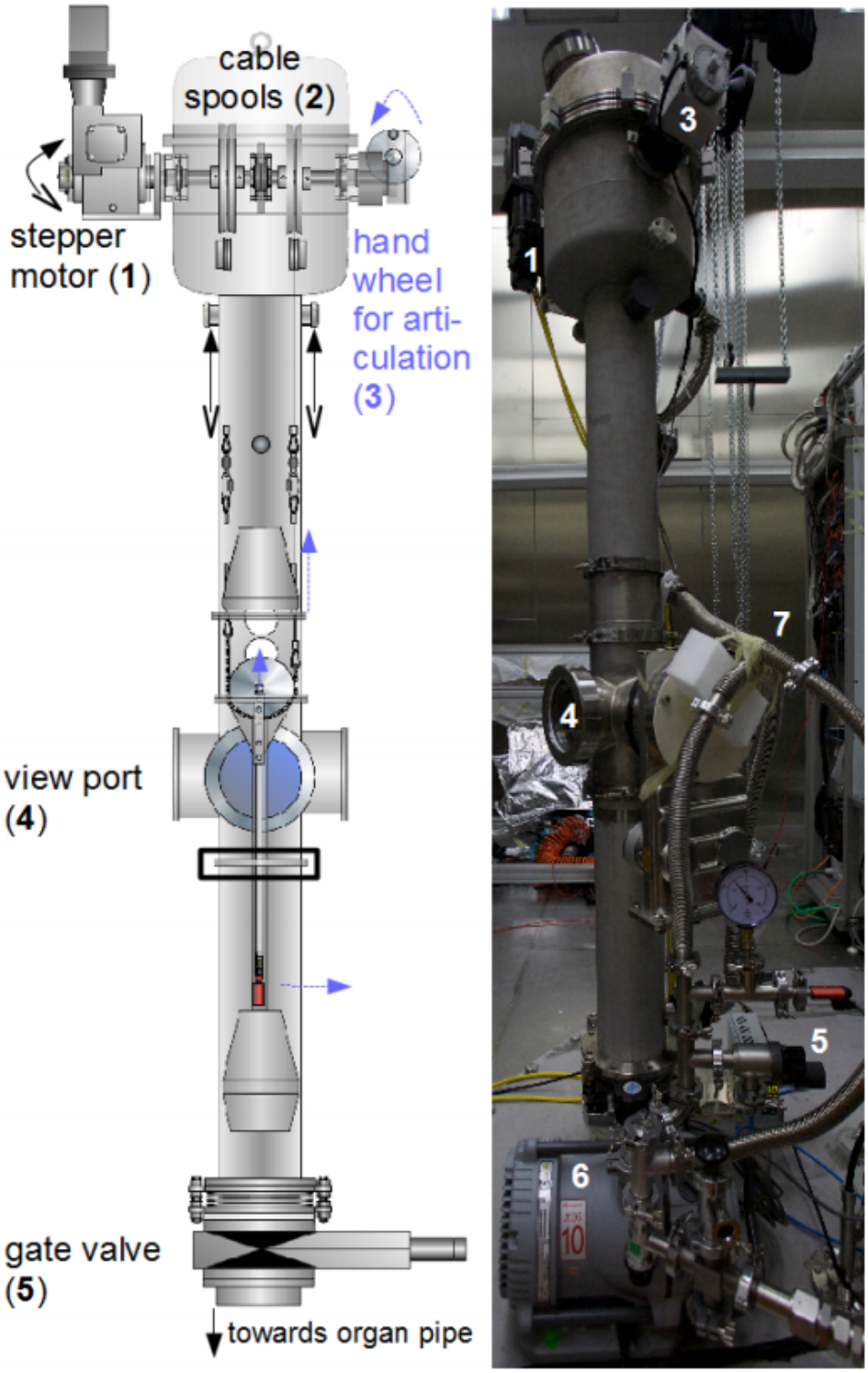

Figure 4.5: Diagram of CALIS, along with a photograph for comparison. The motion of the source arm due to hand wheel rotation is noted. [49].

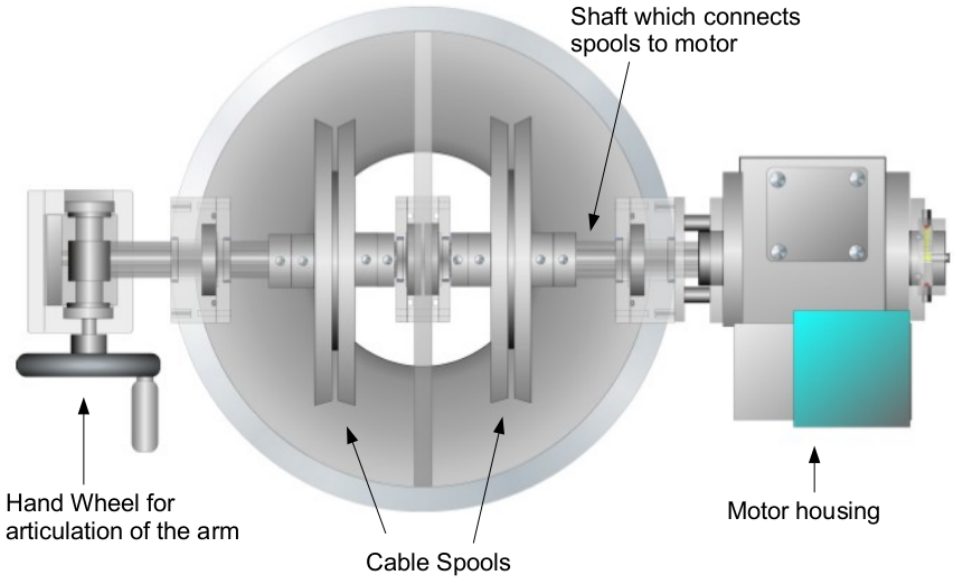

Figure 4.6: Diagram of the interior of the upper assembly, as seen from above.

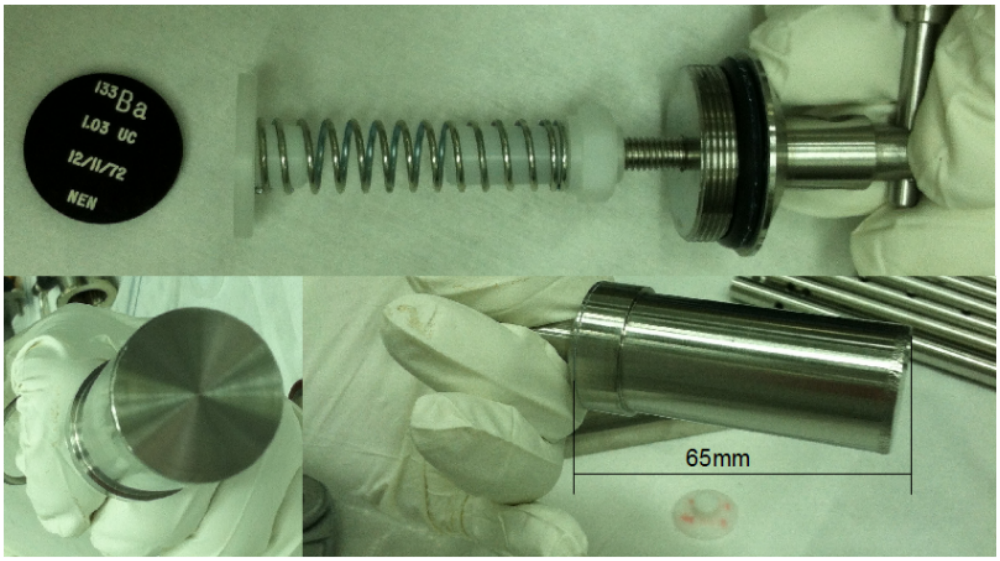

Figure 4.7: Photo of the source holder. Sources are held in place inside the holder by a spring. [49]

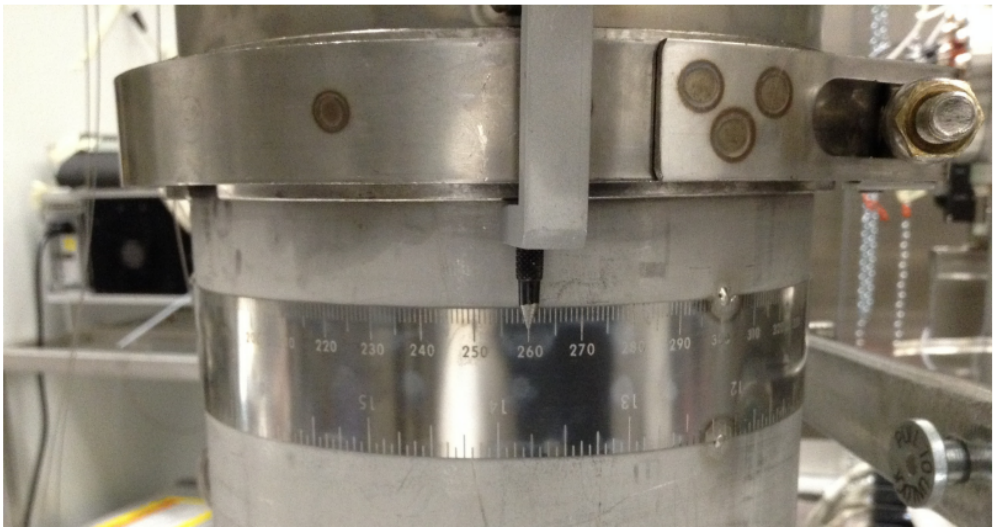

Figure 4.8: The ring clamp between the upper and lower assemblies. The ring clamp is loosened to allow the upper assembly to be rotated, thus rotating the source. The ruler informs the operator of the source position.

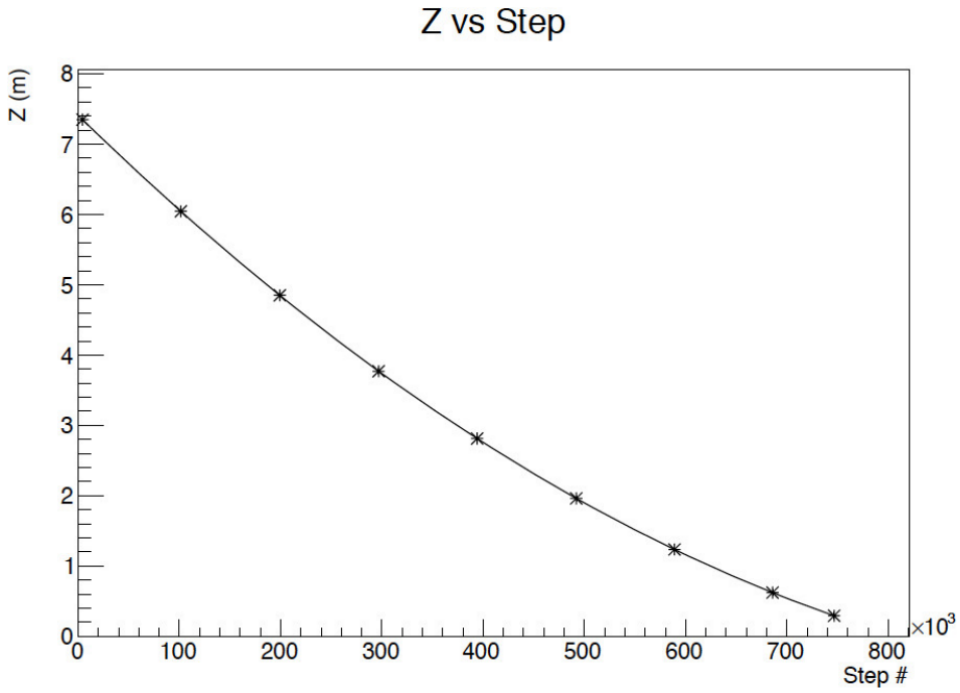

Figure 4.9: Z position (in meters) versus motor step number, as measured during testing. The lowest distance shown is the distance from the bottom of the PIG to the laser ranger when the PIG is fully deployed; similarly, the largest Z value corresponds to the home position, or the greatest distance from the laser ranger.

4.3 Calibration Campaigns with Radioactive Sources

Multiple campaigns have been successfully carried out with CALIS. The first and most comprehensive took place in October and November of 2014. Most recently, the system was used for calibration with AmBe in June, 2016. The specifics of the campaigns utilizing the insertion system are detailed below.

October/November, 2014

The first calibration campaign immediately followed the installation and commissioning of CALIS presented above. At this time, the TPC was filled with AAr, and the LSV had a concentration of 1.4 g/L of the wavelength shifter PPO and less than 0.1% TPB. Three gamma sources were used: ^{57}Co, ^{133}Ba, and ^{137}Cs. As can be seen in Figure 4.10, these sources, along with the internal calibration with ^{83m}Kr, cover the full range of the ^{39}Ar spectrum. In order to determine *in-situ* the dependence of the energy response to drift field, data was taken at 200 V/cm (the nominal drift field), 150 V/cm, 100 V/cm, and null field. In each case, the source was placed near the center of the TPC active volume and against the cryostat wall. An independent check on the source Z position was obtained by taking gamma source data both above and below the central position and on a different side of the cryostat (see Section 4.5). This data also provided a check of the light yield position dependency.

In addition to the gamma sources, two AmBe neutron sources were deployed: one with a high activity of 2000 n/s, and the other with a low activity of 10 n/s. In the case of the high activity source, the rate was too large to place the source directly against the cryostat, as was done with all other sources. As a result, the high activity data was taken with the source approximately 10 cm from the cryostat wall. Because of the large penetration of neutrons, data for these sources was only taken at the central position.

February, 2015

After the concentration of TBP had been increased to 5%, a neutron campaign with the 10 n/s AmBe source was performed, primarily for the purpose of LSV studies. Data was taken with the source at the central TPC position, both against the cryostat and rotated away in order to compare the effects of shadowing by the cryostat on neutron detection. Additionally, data was taken with a PPO concentration of 0.7 g/L and 1.4 g/L (the nominal concentration), in order to study the effects of PPO quenching.

August, 2015

The first calibration campaign in UAr with an external source occurred in August, 2015, with the insertion of a ^{22}Na source. The goal of this calibration was to obtain a high statistics set of β^+

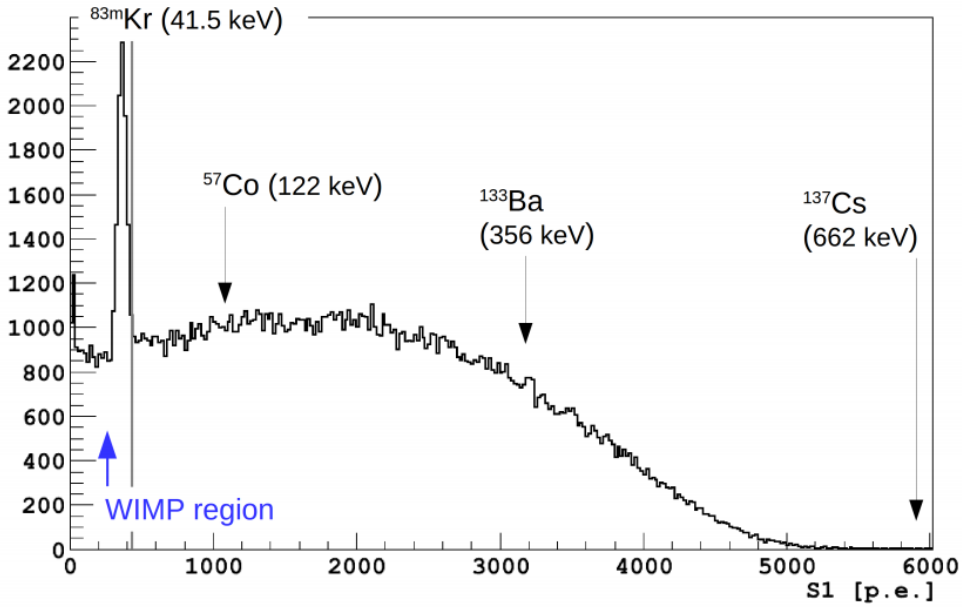

Figure 4.10: The ^{39m}Kr peak, along with the ^{39}Ar background spectrum. Noted are the locations of the full absorption peaks of ^{57}Co, ^{133}Ba and ^{137}Co. [49]

events for studying pulse shape discrimination in the TPC.

December, 2015

In December, 2015, an AmC source was deployed for the purpose of measuring the LSV neutron detection efficiency. This source was created in order to avoid the high energy correlated gamma accompanying AmBe neutron decays, which obscure the prompt neutron thermalization signal in the veto. The analysis of this data is currently nearing completion, and will be detailed in an upcoming publication.

June, 2016

The most recent campaign, in June, 2016, was intended for the study of nuclear recoils in the TPC. An AmBe source with a mid-range activity of 160 n/s was deployed at the central TPC position, against the cryostat. This campaign is described in detail in Section 6.3, and forms the basis for demonstrating the success of the novel calibration technique described in this dissertation.

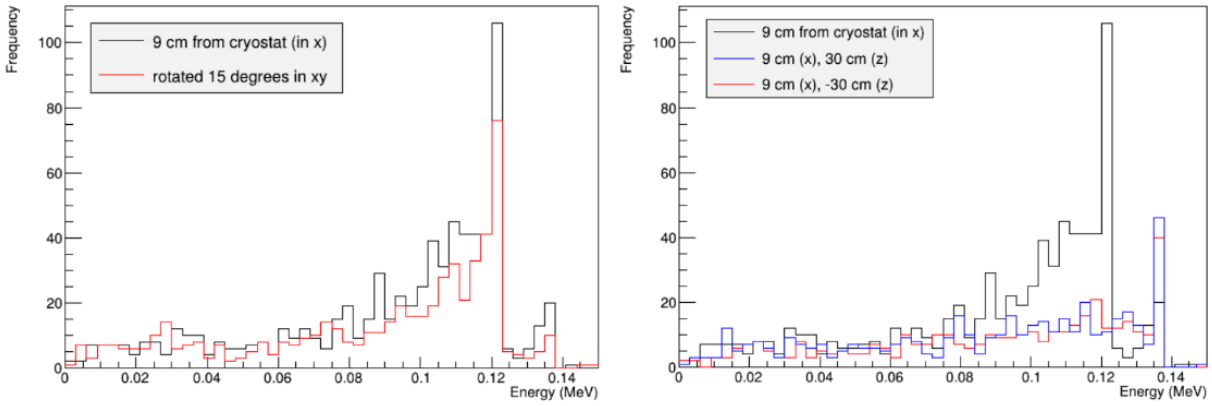

Figure 4.11: Monte Carlo of source spectra in the TPC for ^{57}Co for multiple positions.

4.4 Preliminary Studies

In preparation for source calibrations, multiple extensive Monte Carlo studies were performed, of which one is presented below. These studies aimed to estimate the trigger rate in the TPC in order to properly select the source activity, as well as examine the potential effect of source position. At the time of these studies, prior to the first campaign, optical simulations were not yet available. The following results, therefore, are extrapolated from energy deposits only.

In this study, two gamma sources were simulated, ^{57}Co and ^{133}Ba, and one neutron source, AmBe. The nominal source position was chosen to be 9 cm from the cryostat wall at the central TPC location. This position was then compared to the results with the source rotated away 15° in XY, and shifted up and down in Z by 30 cm. In each case, 1 M events were produced.

The effect of position on source spectra can be seen in Figure 4.11. While rotating the source away in XY causes the rate in the TPC to drop, shifting it up or down by 30 cm in Z causes spectral distortion, and a complete loss of the full absorption peak at 122 keV. The reason for this is that at these positions, which are near the top and the bottom of the cryostat, there is substantially more material between the source and the TPC active volume, particularly stainless steel.

As one would expect, source penetration is strongly dependent on initial energy (see Figure 4.12). Based on this study, an interaction length in LAr of 4.6 cm was found for ^{57}Co. This compares with a finding of 8 cm for ^{133}Ba, and 18.7 cm for AmBe neutrons.

An important discovery was the strong dependence of trigger rate on source position. For the lowest energy source, ^{57}Co, at the simulated nominal position only 0.08% of decays produced a trigger in the TPC. Of these, 25% were in the full absorption peak. For this source, a shift of only 3 cm causes a rate reduction of nearly 50% (see Figure 4.13). Based on these findings, it was concluded that in order to gather statistics at a reasonable rate, all sources would have a nominal position in contact with the cryostat at the center of the TPC active volume. Vertical displacements

were restricted to being within 10 cm of the central position. Given the long interaction length found for AmBe neutrons, no position shift was deemed necessary for this source.

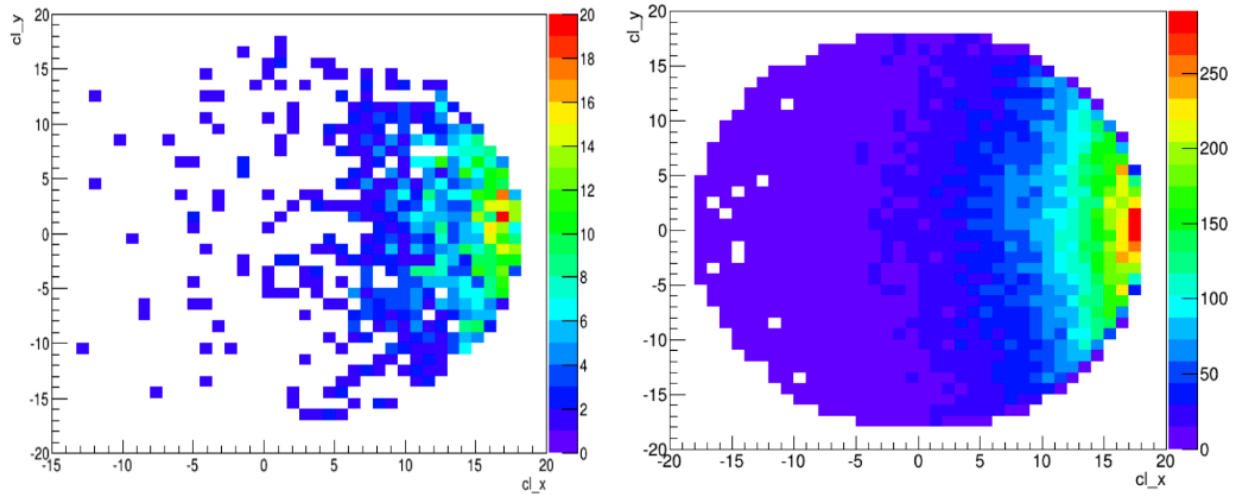

Figure 4.12: Monte Carlo of source induced interactions in the TPC for ^{57}Co (left) and ^{133}Ba (right). ^{57}Co produces a 122 keV gamma in 86% of decays, whereas the primary gamma line from ^{133}Ba is at 356 keV. The dependence on source energy is readily apparent in the above distributions.

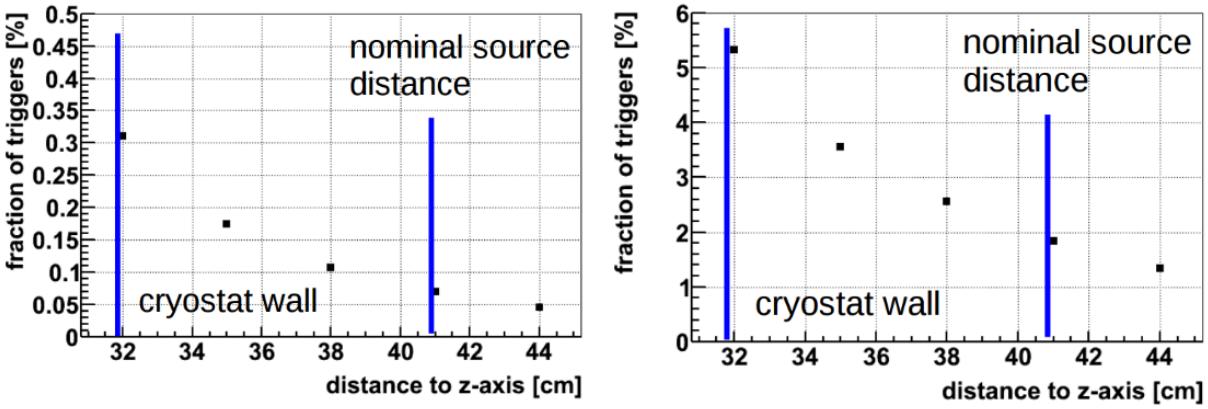

Figure 4.13: Fraction of decays producing triggers in the TPC as a function of source position for ^{57}Co (left) and ^{133}Ba (right). Here the Z-axis marks the location of the center of the TPC active volume. The trigger rate is affected by both the position and source energy.

4.5 Source Position

The vertical position of the source was verified independent of the motor step count by fitting the drift time (t_{drift}) distribution of the gamma sources deployed in the first calibration campaign at the end of 2014. As was described in Section 2.3, the Z coordinate of an event is determined by the time between the S1 and S2 signals, which is the time it takes for the ionized electrons to drift under the influence of the applied electric field.

The small interaction length of ^{57}Co yields a t_{drift} distribution which is well peaked for obtaining the mean event position, and thus the source location. The higher energy of ^{133}Ba gives it a broader distribution, which can nonetheless be fit to extract the mean (see Figure 4.14). The t_{drift} distribution of ^{137}Cs, with a decay energy of 662 keV, is too broad to contribute to this study.

The motor step count 731000 was chosen to be the nominal central position. From the t_{drift} study, this corresponded to a mean position which was 157.4 mm below the extraction grid, or 15.3 mm above the TPC active volume center. The extraction grid is a useful fiducial point, as it is located at a t_{drift} of zero by definition. Over the course of the campaign, a systematic shift in the source position was observed (see Figure 4.15). As a result of this shift, the mean position of 157.4 mm below the grid varied by an RMS of 10.1 mm. In order to avoid this shift in future calibrations, the source is deployed to its fullest depth before being sent to the desired location. This allows the cables to unwind fully, and release any tension which may accumulate and cause asymmetric forces on the source arm.

Because the sources are placed outside of the cryostat, they must first pass through several layers of material before reaching the TPC active volume. This leads to attenuation of the source flux, especially for low energy sources such as ^{57}Co. The amount and type of material will dictate the level of attenuation. Because the TPC materials are not distributed uniformly, photons following different paths will have varying degrees of attenuation. The difference in attenuation, or contrast, may be calculated for different paths. In DarkSide-50, the regular spacing of the copper field rings lead to predictable attenuation patterns. A study by Andrew Watson of Temple University calculated the expected flux in the TPC for 122 keV photons (as produced in ^{57}Co decays) for various Z positions of the source outside the cryostat. This study predicted there should be multiple peaks in the ^{57}Co t_{drift} distribution which correspond to a vertical spacing of 25 mm. As can be seen in Figure 4.16, these peaks are clearly visible in the data. Fits to each peak yielded a mean distance of 26.4 ± 3 mm between them, in excellent agreement with the predicted value.

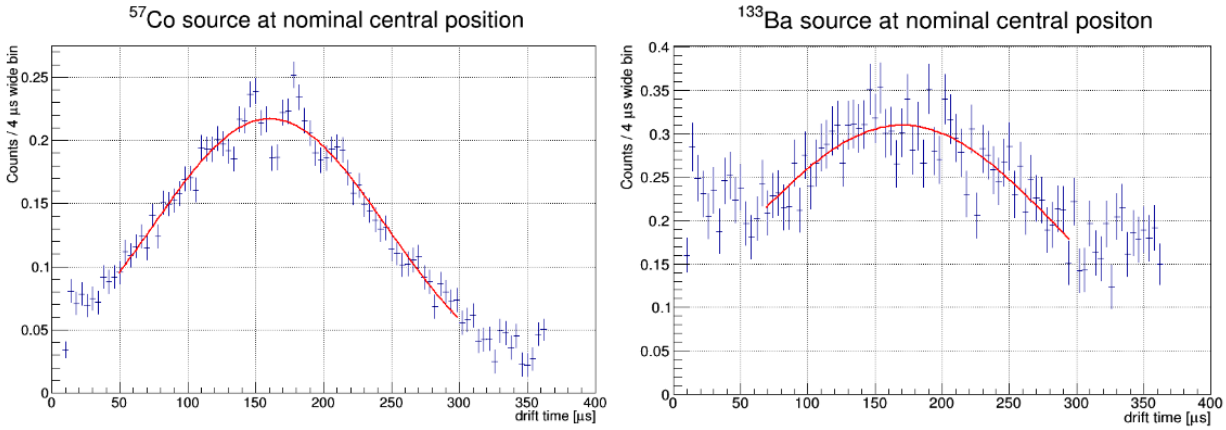

Figure 4.14: t_{drift} distributions for ^{57}Co (left) and ^{133}Ba (right) with the source at the nominal central position, corresponding to motor step count 731000.

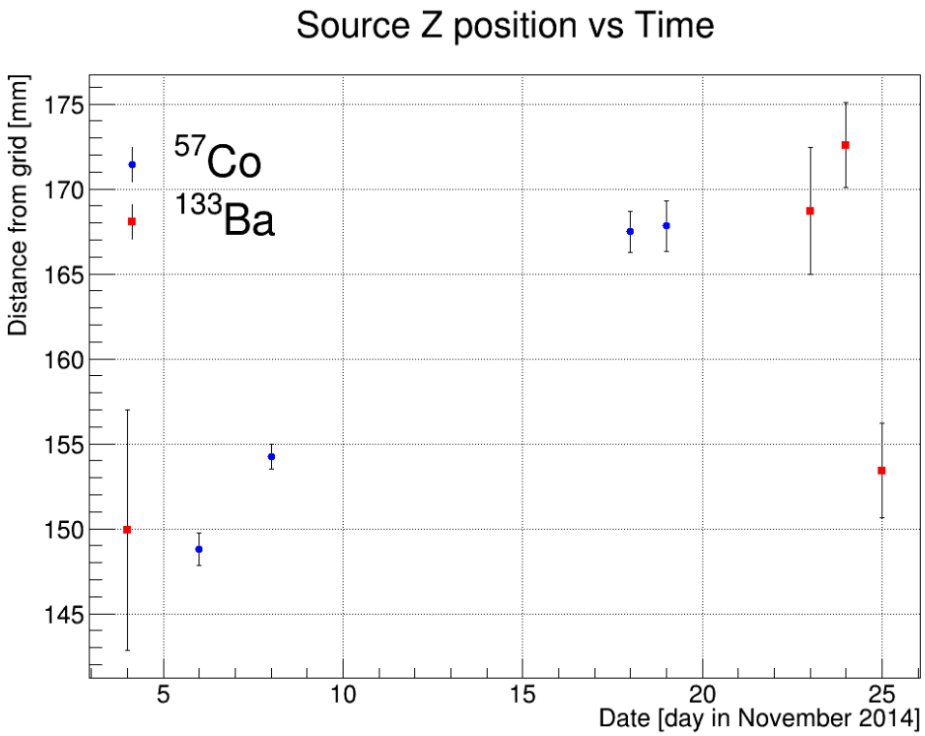

Figure 4.15: Vertical source positon versus time, as determined by the t_{drift} and with the source at motor step count 731000. The errors on the fitted values include both the fit and systematic uncertainties.

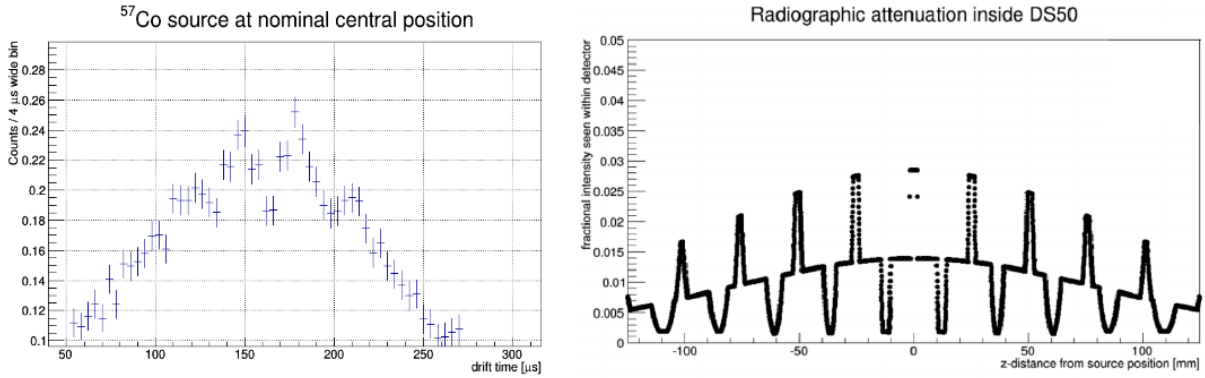

Figure 4.16: *Left:* The peaks in the ^{57}Co t_{drift} distribution due to attenuation by the copper field rings are clearly visible. *Right:* The result of the ray tracing study performed by Andrew Watson, which predicted the peaks seen.

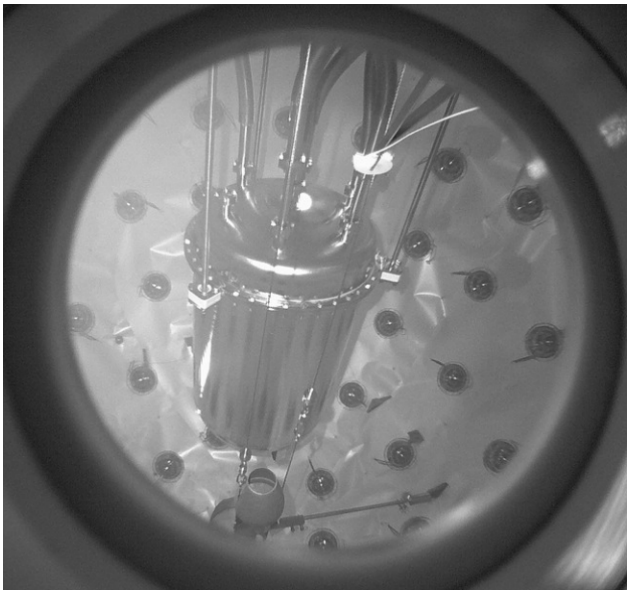

Figure 4.17: Photo of the source deployment system inside the LSV and the position of the AmBe source for this study. The source arm is rotated $\sim 90^{\circ}$ away from the cryostat, placing it approximately 72 cm distant.

4.6 Liquid Scintillator Veto

Following the February, 2015 AmBe campaign, a comprehensive analysis was performed with the goal of identifying the 6.4% of neutron captures on ^{10}B which produce only a 1.78 MeV α and a ground state ^{7}Li atom. As these capture products are heavily quenched, the ability to detect this signal is a critical factor for reaching a high vetoing efficiency. The data used for this study was taken with the AmBe source placed approximately 72 cm away from the TPC (see Figure 4.17). Two concentrations of PPO were employed during the data taking period: 0.7 g/L and 1.4 g/L. A second analysis goal was then to measure the quenching effect of the wavelength shifter by comparing the capture peak positions at each concentration.

The LSV was self-triggered on the prompt 4.4 MeV gamma signal. For approximately the first 20 μs after the trigger, the low energy region where the α-only channel is located is dominated by PMT after-pulsing. Low energy photons from ^{241}Am also populate this region throughout the event. The after-pulsing region is avoided by only looking at veto clusters occurring more than 20 μs after the prompt LSV signal. To remove the accidental background, we use a restricted time window of 30 μs, starting not more than 60 μs after the prompt, and statistically subtract the off-time spectra between 100 and 130 μs after the prompt. In this region, we expect few neutron captures, while the rate of accidental backgrounds remains constant. Additionally, we except only the first cluster in the relevant time window.

The α-only capture peak can clearly be seen at ~30 PE in Figure 4.18. The second, larger peak at ~270 PE is the $\alpha + \gamma$ capture channel. The branching ratio is estimated by taking the ratio of the area under the α-only peak (from 0 to 50 PE) to the total area under both peaks (from 0 to 350 PE). The results for each of the time windows used in the analysis can be seen in Figure 4.19. Excellent agreement is shown with the literature value of 6.4%. This study demonstrated a better than 99.1% efficiency for the detection of radiogenic neutron captures [46].

The PPO was found to decrease the light yield of the $\alpha + \gamma$ peak by ~5%, possibly due to enhanced self-absorption, while increasing the light yield of the α-only signal by ~11% [46]. The increase in the second case is likely due to the PPO reducing the level of ionization quenching.

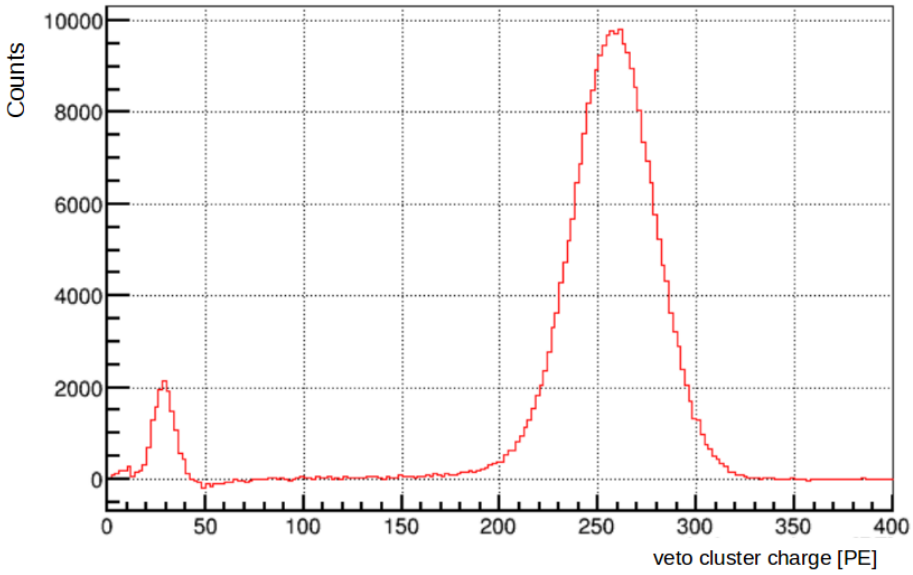

Figure 4.18: Cluster charge spectra after background subtraction. The low energy peak at ~30 PE is due to neutron captures on ^{10}B which produce only an α particle and a ^{7}Li atom in the ground state. The peak at ~270 PE is due to the 93.6% of such captures which produce also a 478 keV γ.

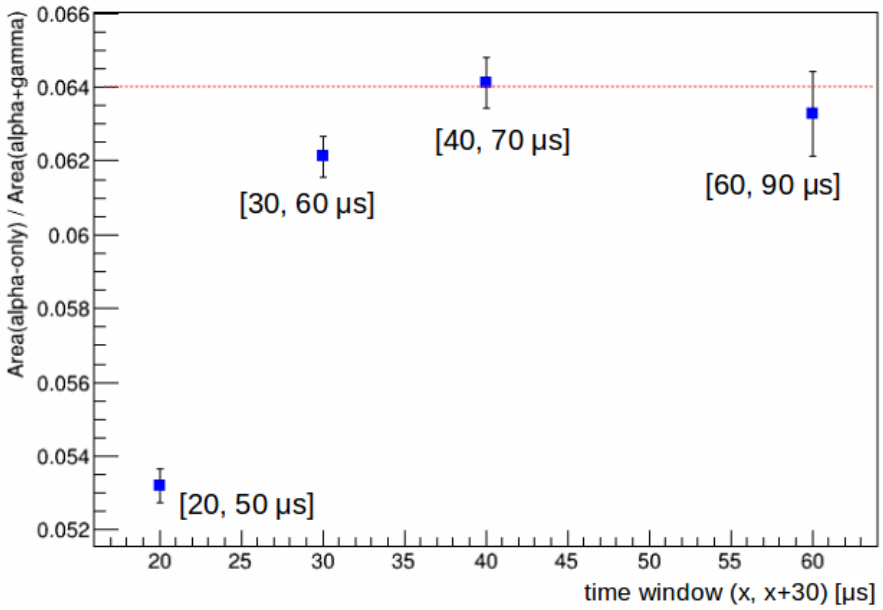

Figure 4.19: Branching ratio of the α-only capture channel, as measured by the ratio of the area under the α-only peak (from 0 to 50 PE) to the area under both capture peaks (from 0 to 350 PE) for veto clusters occurring in the given time window. The red dashed line indicates the literature value of 6.4%.

4.7 ScENE

In order to determine the energy response of liquid argon to single-sited nuclear recoils, a dedicated experiment was carried out by a portion of the DarkSide collaboration called ScENE (Scintillation Efficiency of Noble Elements) [50]. Protons were accelerated onto a LiF target, producing neutrons via the reaction ^{7}Li(p,n)^{7}B. Three liquid scintillator neutron detectors were placed at angles to the LAr TPC, so that neutrons scattered in the LAr and striking a given detector would have a known recoil energy and momentum. Figure 4.20 shows a schematic of the experimental setup, as well as close up view of the LAr TPC. Neutron recoil energies between 10.3 and 53.6 keV were measured for TPC drift field values between 0 and 970 V/cm. Two methods were used to model the pulse shape parameter, f_{90}, of the events: a fit with the Hinkley (or ratio-of-Gaussians) model, described in Section 7.1.1, and a statistical simulation of all the processes contributing to a scintillation signal in LAr. Using either model, any LAr experiment can use the $L_{eff,^{83m}Kr}$ and f_{90} means reported by the ScENE experiment to produce nuclear recoil acceptance for their particular detector, using only the light yield at null field to normalize the values. Here, $L_{eff,^{83m}Kr}$ is the scintillation of nuclear recoils at some drift field, ε_d, relative to electron recoils from ^{83m}Kr at null field, ε_0:

$$L_{eff,^{83m}Kr} = \frac{(S1/E)_{nr}|\varepsilon_d}{(S1/E)_{Kr}|\varepsilon_0}$$

This method was used by DarkSide-50 to establish the nuclear recoil acceptance in the first physics analysis, prior to an *in-situ* neutron calibration [30]. Once neutron calibration data was available, following the November, 2014 campaign, the extrapolation of ScENE values to DarkSide-50 was compared to the f_{90} medians from AmBe. For this analysis, the high-activity (2000 n/s) AmBe data was used. Both the electron and nuclear recoil bands were fit with the sum of two Gaussians. The result is shown in Figure 4.21, as published in [39]. Excellent agreement between the extrapolated f_{90} values and those measured *in-situ* is shown, validating the use of ScENE values for the DarkSide-50 WIMP analysis, presented in greater detail in Chapter 5.

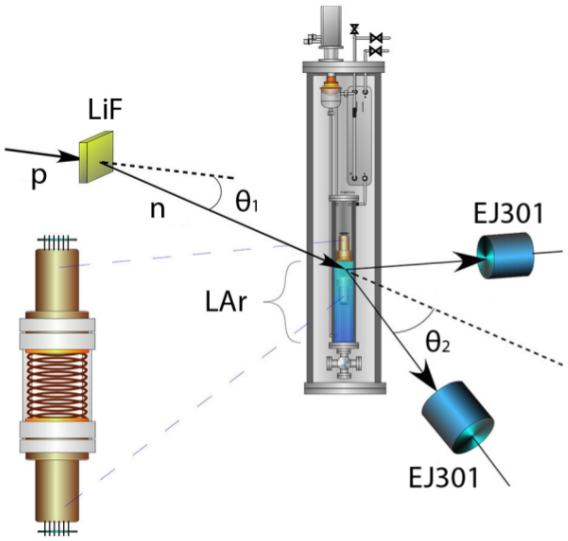

Figure 4.20: A schematic of the experimental setup used by ScENE. [50]

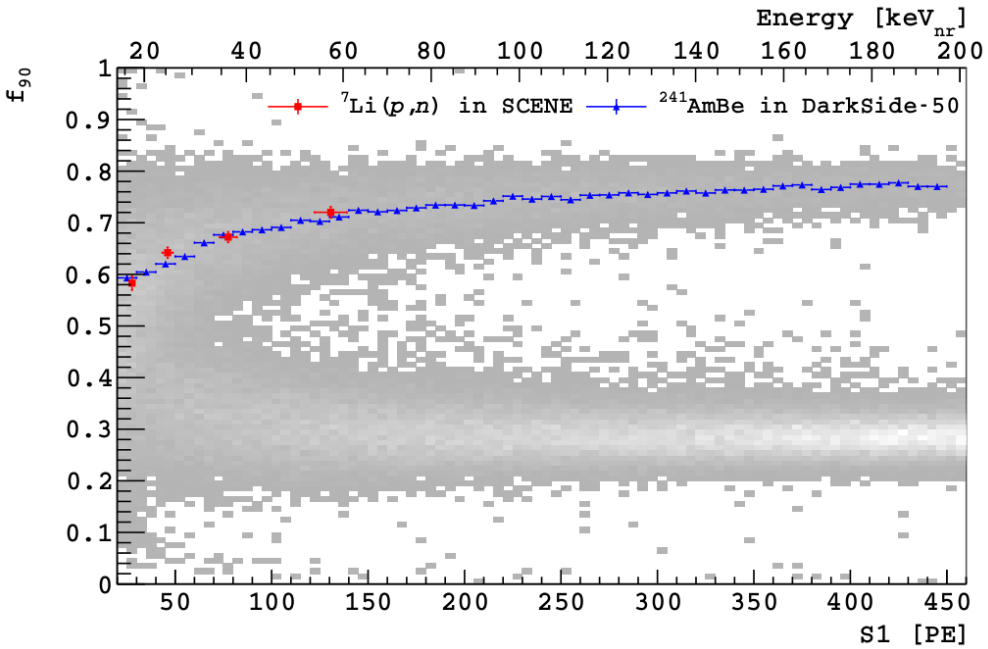

Figure 4.21: Comparison of the median f_{90} values extrapolated from ScENE and those found from sum of two Gaussian fit to the high-activity AmBe data in DarkSide-50. [39]

CHAPTER 5
WIMP SEARCH WITH UNDERGROUND ARGON

Following the successful accumulation of 47 live days of WIMP search data with AAr, DarkSide-50 set a spin-independent WIMP exclusion limit of 6.1 x 10^{-44} cm^2 for a WIMP mass of 100 GeV/c^2, the best limit from a liquid argon target at the time of its publication [30]. In order to improve the sensitivity, as well as to demonstrate the reduction in background necessary for future detectors, the AAr was replaced by UAr in April, 2015. 70 days of live data were accumulated with this improved target, leading to the publication of the current best limit with argon. The details of the WIMP search analysis which led to this result are given below.

5.1 Data Selection

The data taking for the 70-day UAr analysis took place between April 8th and July 31st, 2015. In order to ensure the integrity of the data used for the WIMP search, all the runs were inspected for quality. Data runs which occurred during human operatons in CRH, which can create unpredictable noise in the electronics, or any other cause which may have the same effect, are not included. Additionally, any runs which had a very high rate in a single PMT, or were very short (likely due to crash of the DAQ or ODAQ) are likewise excluded. The trigger rate and light yield of both the TPC and LSV were monitored and found to be stable, save for a few runs in which the TPC had a higher or lower than normal rate; such runs were removed. The electron lifetime and maximum drift time were both monitored as well and no issues were found. The only additional runs which were removed occurred over a period of about one day, in which the width of the laser pedestal had sharply increased, before returning to normal. The cause of this increase is not known.

5.2 Event Selection

Once all the data runs were verified to be robust, events were selected by a sequence of analysis cuts which ensure the events which pass are valid and meet the criteria for WIMP candidates.

5.2.1 Quality Cuts

The first event cuts applied, like the data selection cuts, are designed to ensure that each event considered in the analysis does not suffer from transient electronics or PMT issues.

Number of channels

Definition: Number of channels present = 38

Very occasionally, a malfunction may cause a single PMT channel to be missing from the data. This cut requires that data from all 38 PMTs is recorded for each event, so that the light yield of each event is properly reconstructed. Very few events (less than 0.01%) are removed by this cut.

Baseline found

Definition: The baseline is found on all PMT channels

Since all the characteristics of an event depend on accurately calculating the sum channel integral, it is essential that the baseline finder algorithm functions normally on every individual channel. Should the algorithm abort for any reason, the event is rejected. This cut removes about 13.6% of all events.

Time between events

Definition: Event lifetime + inhibit time > 1.35 ms

In order to remove pile-up events, where one event is triggered on the light from the end of the previous event, we require that the event lifetime plus the inhibit time is greater than 1.35 ms. This ensures that the event start time of each event is at least 1.35 ms after the start time of the event prior. This cut removes 5.3% of events which pass the previous two cuts.

Correct live time

Definition: Event lifetime < 1 s

This cut removes events which have very long lifetimes, due to problems with the DAQ file input / output procedure. This process was improved prior to the UAr campaign, so no events were removed by this cut.

Veto present

Definition: There is a matching veto event for the event in the TPC, with the correct timestamp

If the DAQ for either the TPC or the outer detectors malfunctions, or one of the reconstruction algorithms fail for either detector, either the TPC or veto event will not be recorded. In this case, the event is rejected. After all previous cuts, this cut removes 0.9% of events.

5.2.2 Physics cuts

The purpose of the following cuts is to reject events which do not meet the criteria of a WIMP candidate. The only parameter needed to characterize a WIMP event in the TPC which is not applied here is f_{90}, so that the full f_{90} region is included in the analysis.

Single scatter

Definition: The number of pulses is 2 or 3, IF the third pulse is an S2-echo

Given the small cross section for a WIMP scatter in the TPC, the likelihood of a WIMP scattering twice is vanishingly small. Background particles, such as photons, however, have a relatively large likelihood of multiple interactions. We therefore require that all events have only two pulses, the S1 pulse and the S2 pulse, corresponding to a single scatter event. A bright S2 pulse, however, can photoionize the cathode, releasing electrons which are then drifted to the gaseous argon layer, producing a scintillation signal in the same way as regular S2 pulses. These "echoes" are always separated in time from the original S2 pulse by the maximum drift time, having transversed the full length of the TPC active volume, and so are easy to identify. Of the events which survived all previous cuts, 66.5% are removed by this cut, the vast majority of which are due to γ interactions.

S1 start time

Definition: -6.1 μs < S1 start time < -6.0 μs

This cut removes events which are triggered on the end of the previous event, but still had a true particle scatter occur within the ensuing event time window. The event tails which cause the trigger will be very small, with only a few photoelectrons. The pulse finder algorithm will, therefore not reconstruct these tails as the first pulse, but rather the pulse from the true particle scatter, causing a delay between the event start time and the S1 start time. The reason this start time is not expected to be at $t = 0$ is due to the cable lengths and connections creating an offset of $\sim$6 μs. Only 0.3% of events which pass the previous cuts are removed by this cut.

S1 not saturated

Definition: The digitizers are not saturated by the S1 pulse

Very high energy S1 signals are likely to saturate the ADCs, making an accurate reconstruction of the event energy impossible. Such saturation can also occur at lower energies, but with decreasing probability. Since the event energy is not determined by the charge of the S2 pulse, no saturation cut is applied to S2. This cut removes 0.8% of events passing earlier cuts.

Maximum S1 fraction

Definition: The fraction of S1 light in the maximum channel relative to the total light from all other PMTs does not exceed that in 95% of events

The purpose of this cut is to address the problem posed by Cherenkov light produced by γ particles scattering in the Teflon or in the fused silica of the anode and cathode windows. Cherenkov light observed in the TPC is very fast, with a very high f_{90}, and no ionization (S2) signal. When

the γ which caused the Cherenkov light also scatters in the TPC, so that the scintillation light of both sources is combined in a single pulse, the f_{90} value is biased upwards, towards the nuclear recoil region. Because the Cherenkov radiation does not produce an S2 signal, the ratio of S2 to S1 is biased downwards, also in the direction of nuclear recoils, making this a dangerous class of backgrounds for a WIMP search. For Cherenkov radiation produced in the fused silica, however, the light will be strongly concentrated in a single PMT. This allows for the definition of the S1 maximum fraction cut. Since the amount of concentration will depend on how close the pulse is to the PMTs, the cut is defined in the S1-t_{drift} plane, which is divided into a grid. For each grid point, the 95% quantile for the S1 maximum fraction is determined from the high statistics AAr data. Events with S1 maximum fractions above this threshold are discarded. By definition, this cut removes 5% of events which pass all previous cuts.

Valid S2

Definition: S2 charge $>$ 100 PE and S2 $f_{90} < 0.2$

The purpose of this cut is to remove events where the S2 pulse is not actually an S2 pulse. When the events are reconstructed, the first pulse is assumed to be S1, and the second S2. That is, the first pulse is assumed to be the scintillation light due to a particle scattering in the TPC, and the second pulse is assumed to be the ionization signal from that scatter. While this is almost always true, in particular after the application of all previous cuts, we can ensure that it is by requiring the S2 pulse to have the characteristics of the ionization signal, namely, a significant charge and a low f_{90}. A negligible fraction of events were removed by this cut.

Drift time

Definition: 40 μs $< t_{drift} <$ 334.5 μs

This cut creates an inner fiducial volume in order to remove surface background events from the top and bottom of the TPC. Most of these events are due to radiation in the PMTs. Since there has been no evidence of radiation from the TPC walls, an XY fiducialization cut is not applied.

5.2.3 Veto cuts

The purpose of this class of cuts is to reject any events in the TPC which may be due to background particles which transversed the veto, prior to interacting in the TPC. These cuts are especially essential for rejecting radiogenic or cosmogenic neutrons.

Prompt

Definition: No signal greater than 1 PE in the LSV in a 300 ns window around the TPC prompt time

The purpose of this cut is to detect the prompt neutron thermalization signal. As a result of this cut, there is a less than 1% acceptance loss due to accidental coincidences in the veto.

Delayed

Definition: No signal greater than 6 PE in the LSV any time between the TPC prompt and the end of the acquisition window (200 μs)

This cut is designed to detect the delayed neutron capture signal, and introduces a nuclear recoil acceptance loss of about 16%.

Pre-prompt

Definition: No signal greater than 2 PE in the LSV in the 500 ns from the start of the acquisition window to the TPC prompt time

The purpose of this cut is look for any signal which might precede a neutron scatter in the TPC, and thus mark it as such. The acceptance loss due to this cut is very small, at $\sim$0.1%.

5.3 Nuclear Recoil Acceptance

To determine the nuclear recoil acceptance, the Hinkley f_{90} model was used. For the purpose of this analysis, the same application used for the electron recoil leakage curves was applied also to nuclear recoils. Specifically, the model had two free parameters: the mean f_{90} value and the normalization factor, and 6 fixed parameters: μ, σ_{TPB}, σ_{SPE}, $\sigma_{elec,p}$ and $\sigma_{elec,l}$, and the Fano factor (see Section 7.1.1 for a full description). The values of the various noise parameters were fixed to those determined from electron recoil calibrations. The parameter μ was fixed to the center S1 bin value, and the Fano factor was fixed at 1.

At the time of this analysis, data from two AmBe neutron sources was available: the high-activity, 2000 n/s source, taken during the calibration campaign of October/November, 2014, and the low-activity, 10 n/s source, from the February, 2015 campaign. In both cases, for S1 energies less than $\sim$100 PE, the presence of the electron recoil band from ^{39}Ar and source induced gamma interactions introduced significant difficulties in fitting the model to the nuclear recoil region. This was especially true in the case of the low-activity source, which, while producing larger neutron statistics overall, was strongly dominated by the high ^{39}Ar rate. For this reason, the high-activity source was used.

In order to perform the fits, the AmBe f_{90} distributions were sliced into 10 PE wide bins in S1. The Hinkley model was found to be extremely sensitive to the presence of electron recoils in the low energy region of the nuclear recoil band, and was not as good a fit to the data overall compared to a simple Gaussian fit. Therefore, both the electron and nuclear recoil bands were fit with the sum of two Gaussians (see also Section 4.7, Figure 4.21). For S1 values below 130 PE, the f_{90} means of

the Hinkley model described above are fixed to those extrapolated from the ScENE data. Above 130 PE, where ScENE data is not available, the means are fixed to the nuclear recoil mean from the Gaussian fit. The normalization was set to the number of entries in the given histogram. After fixing the noise parameters, it was possible to extract the model quantiles in order to define the acceptance curves.

5.4 Results

At the completion of the analysis, no evidence for WIMP dark matter was found. Importantly, no events were seen in the WIMP expected signal region, demonstrating the ability to operate free of background (see Figure 5.1). This is a key result for the future of direct detection experiments, giving tonne scale liquid argon detectors an excellent prospect to make an unambiguous claim of dark matter discovery should a WIMP signal be seen. Furthermore, the background free status was achieved using the event discrimination provided by the S1 signal alone, and without a radial fiducial cut. Additional background rejection is available by making use of the information in the S2 signal, specifically, the S2/S1 ratio, which is substantially different for electron and nuclear recoils (see Figure 5.2).

After combining the data with the previous AAr search, a spin-independent WIMP exclusion limit was established at 2.0 x 10^{-44} cm^2 for a WIMP mass of 100 GeV/c^2, the best limit on an argon target to date (Figure 5.3).

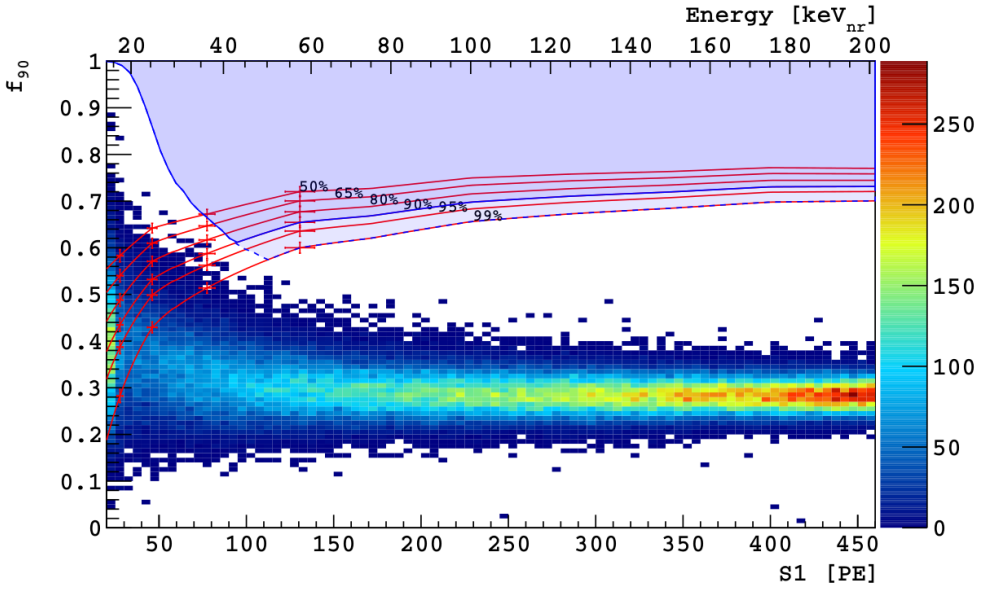

Figure 5.1: The full f_{90} region for all events which survive the cuts listed in Section 5.2, versus S1. The expected WIMP signal region is shaded in blue. The nuclear recoil acceptance curves below 130 PE are derived from ScENE values, while above this value they are taken from AmBe calibration data. [39]

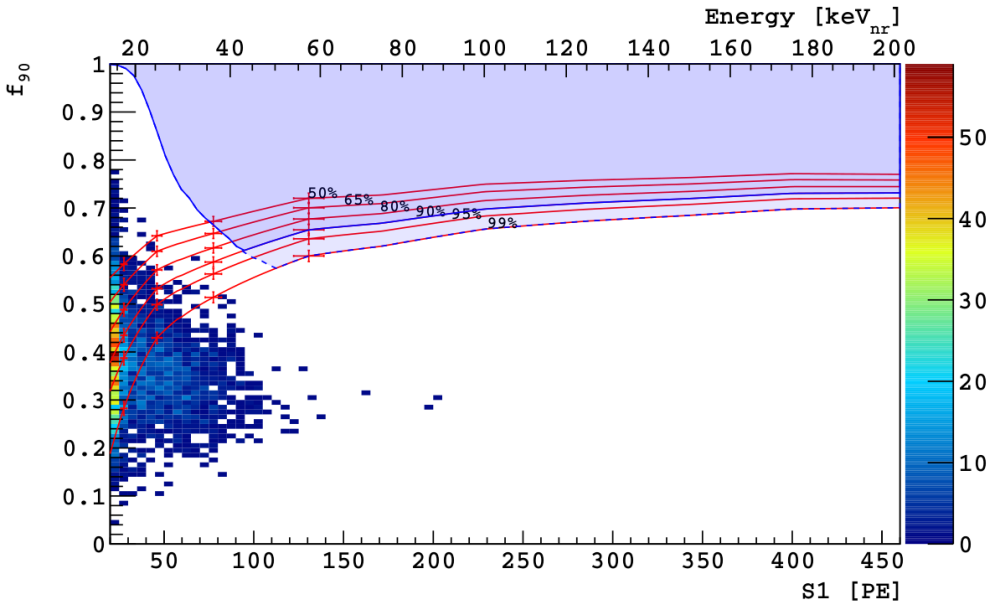

Figure 5.2: Events in the f_{90} versus S1 plane, after application of a radial cut (r $<$ 10 cm) and an S2/S1 cut, requiring the ratio to be less than the nuclear recoil median value. [39]

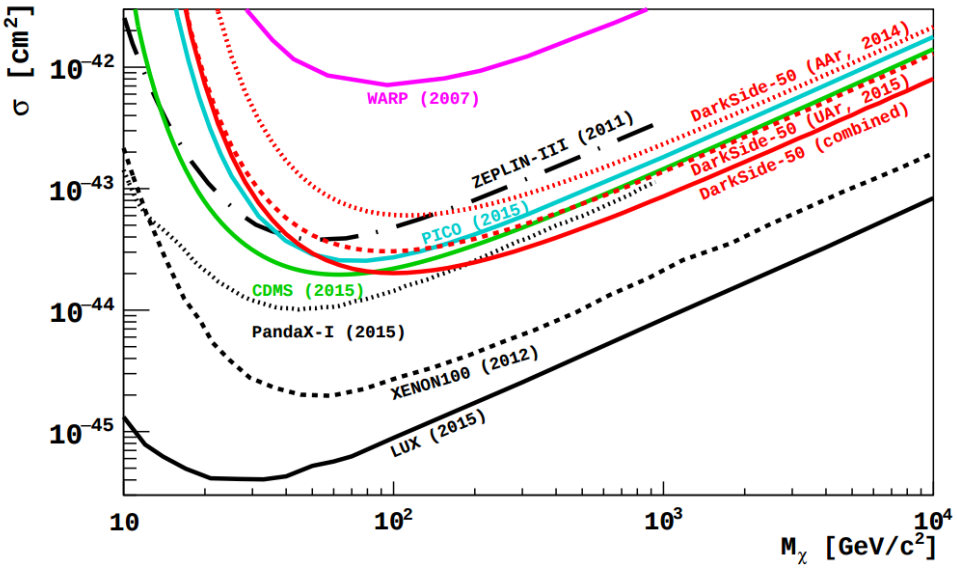

Figure 5.3: The current WIMP exclusion curve for the combined UAr and AAr runs in DarkSide-50 is the best limit by a liquid argon target to date. [39]

CHAPTER 6
NUCLEAR RECOIL CALIBRATION

6.1 Neutron Source Characterization

Before using neutron source data to characterize the DarkSide-50 response to nuclear recoils, we must first begin with a characterization of the sources themselves. Two sources have been used for nuclear recoil calibration: americium-241 beryllium (AmBe) and americium-241 carbon (AmC). While AmBe has an extensive history of use as a neutron source, AmC is comparatively less common. Both are compound sources which produce neutrons via an (α, n) reaction. The properties of each will be explored below.

Figure 6.1: Neutron kinetic energy spectrum from ^{241}Am^{9}Be.

6.1.1 Americium-241 Beryllium

AmBe produces neutrons through one of two channels:

$$\alpha + {}^{9}\mathrm{Be} \longrightarrow {}^{12}\mathrm{C}^{*} + n \tag{6.1}$$

$$\alpha + {}^{9}\mathrm{Be} \longrightarrow {}^{9}\mathrm{Be}^{*} + \alpha' \longrightarrow {}^{8}\mathrm{Be} + n + \alpha' \tag{6.2}$$

The second channel, Eqn. 6.2, produces low energy (less than 1.5 MeV) neutrons and no photons. The first channel, Eqn. 6.1, yields a neutron and a carbon atom in either the ground

state or an excited state. There are two potential excited states, at 4.4 and 7.65 MeV, however, only the 4.4 MeV state relaxes via gamma emission. This is then the source of the correlated gamma in 60% of decays, which occur with neutron energies between 2 and 6 MeV. The full neutron energy spectrum, shown in Figure 6.1, reaches energies near 11 MeV, with a mean energy of ∼4.5 MeV.

As was described in Section 4.3, three AmBe sources have been used for DarkSide-50 calibration: a low activity 10 n/s source, a very high activity, 2000 n/s source, and one with a mid-range 160 n/s rate. The detector conditions were different for each deployment. In the case of the 2000 and 10 n/s sources, the TPC was filled with AAr, while the 160 n/s source deployment occurred after replacing the AAr for UAr. Of interest is measuring the time constant for neutron capture on ^{10}B in the veto, and the relevant abundance of electron to nuclear recoil events, particularly correlated gamma events, as seen in the detector. These values for the 10 n/s source will be determined here. As the LSV had negligible TMB concentration at the time of the high activity calibration, this source is not analyzed. Following the discussion of the June, 2016 campaign, the results for the 160 n/s source will be presented.

Characterization of the 10 n/s AmBe Source

During the February, 2015 campaign and after, the LSV had a TMB concentration of 5%. At this level, from cross section calculations we expect more than 90% of neutron captures to occur on ^{10}B, with a mean capture time of approximately 22 μs [46]. To select neutron capture events, we first identify the peak in the LSV charge spectrum from neutron captures on ^{10}B (this spectrum, with the capture peak indicated, can be seen in Figure 6.7). The neutron capture peak is fit with a Gaussian, and events with veto clusters within $\frac{1}{2}\sigma$ of the mean which appear at least 50 ns after the prompt signal in the TPC are selected. We then examine the time profile of these clusters with respect to the TPC prompt time (δt prompt), for events in which either a gamma-like ($f_{90} < 0.45$) or neutron-like ($f_{90} > 0.5$) interaction took place in the TPC (Figure 6.2). As neutron capture times follow a falling exponential distribution, while background events are relatively constant in time, we fit the δt prompt spectrum with an exponential plus a constant term. The mean neutron capture time is then given by the coefficient on the exponential term for neutron-like events. For this source, we measure a capture time of $22.9 \pm 0.4 \mu$s, in good agreement with expectations. (Note that the uncertainty on this measurement is due to the fit error only, and does not include systematic effects.) Assuming all neutron-like events in the TPC are due to the neutron scattering prior to being captured in the veto, the constant term should be zero, since there is a 100% correlation between the TPC prompt signal and the LSV capture signal. This will not be precisely true, as low energy electron recoil events have f_{90} values which can be higher than 0.5, and thus be counted as a neutron-like event. Some uncorrelated events, therefore, will be included in the nuclear recoil δt prompt spectrum, although we expect the fraction to be small.

Examining the δt prompt spectrum for gamma-like events, we expect both a correlated and an

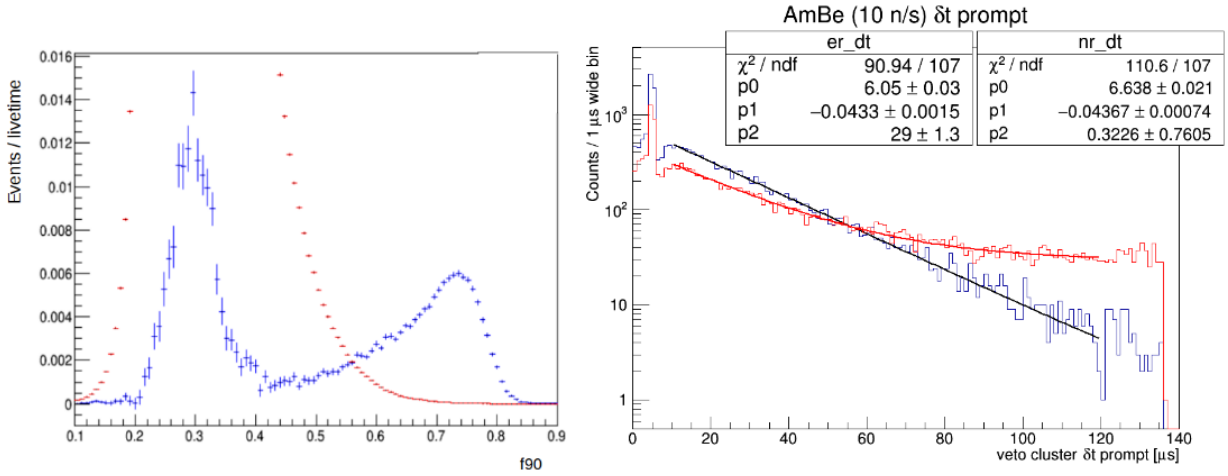

Figure 6.2: *Left:* The f_{90} distribution for the 10 n/s AmBe source. The background ^{39}Ar, shown overlaid in red, has been statistically subtracted. The gamma-like events are those with $f_{90} < 0.45$, while the neutron-like events have $f_{90} > 0.5$. *Right:* δt prompt spectra for gamma-like (er_dt, red) and neutron-like (nr_dt, blue) events, after selecting on the neutron capture signal. Each has been fit with an exponential plus a constant term.

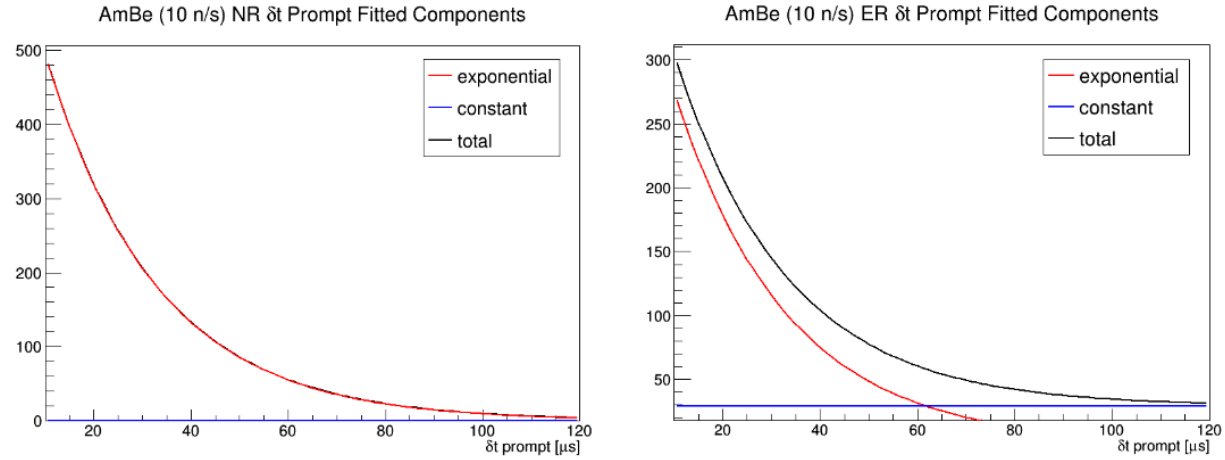

Figure 6.3: The exponential and constant components, as found from a fit to the δt prompt spectra. The ratio of the area under the exponential curve (red) to the total function area (black) provides a measure of the fraction of events which are correlated to the neutron capture.

uncorrelated component. In events where the neutron capture signal is seen in the LSV, gamma-like events in the TPC are caused by correlated gammas from the AmBe source, as well as inelastic neutron interactions in the detector materials, and uncorrelated electron recoils from the inherent detector background. This last is especially true for AAr, which has an ^{39}Ar rate of about 50 Hz in the TPC. Uncorrelated gammas are also produced in large number by ^{241}Am, the majority of which have an energy of 60 keV, along with a tail of higher energy photons. These are heavily

degraded by the Pb shield in the source holder as well as the stainless steel of the cryostat, and most do not make it into the TPC. By calculating the ratio of the area under the exponential curve to the total fitted area (exponential plus constant), we get a measure of the fraction of gammas which are correlated to the neutron.

Figure 6.3 shows the exponential and constant terms from the fit to both the nuclear and electron recoil δt prompt spectra. In the case of neutron-like events in the TPC, we find a 99.7% correlation, consistent with our expectations. For gamma-like events, we find a correlation of 66.4%. This means that, for events in which a neutron was produced but did not scatter in the TPC, about 33% of TPC triggers were due to the uncorrelated β and γ background, the vast majority of which come from ^{39}Ar. The size of this background relative to the source rate can be seen in Figure 6.2, left. Relative to all neutron capture events, the fraction of correlated gamma events in the TPC is found to be 30.4%.

6.1.2 Americium-241 Carbon

AmC was utilized by DarkSide specifically for the purpose of measuring the vetoing power of the LSV. Although the ability to efficiently detect captures had already been demonstrated with AmBe data (see Section 4.6), the full powers of the LSV should enable event vetoing based on the prompt neutron thermalization signal alone. This signal is obscured in the majority of events by correlated gammas in AmBe, which also accompany neutron decays from most (α, n) sources, impeding a direct measure of vetoing efficiency in this regime. As mentioned in Section 4.3, the results of evaluating the LSV vetoing efficiency based on the prompt thermalization signal from AmC will be released in an upcoming publication.

AmC neutrons are produced by the reaction:

$$\alpha + {}^{13}\mathrm{C} \longrightarrow {}^{16}\mathrm{O}^{*} + n \tag{6.3}$$

The oxygen atom is produced in either the ground state, or the first or second excited states. The first excited state relaxes via production of a β^{-}/β^{+} pair, which are stopped in the source holder. The second excited state relaxes via emission of a 6.13 MeV correlated gamma. However, the threshold for production of ^{16}O in the first excited state is 5.05 MeV, and the second excited state threshold is 5.11 MeV, while the α's from ^{241}Am have an energy of $\sim$5.5 MeV. By attenuating the energy of the α below $\sim$5 MeV, correlated gamma emission can be avoided.

The AmC source was constructed at LNGS, following the design implemented by the Daya Bay collaboration [51]. The ^{241}Am is a commercial 3.7 MBq source. Rather than a fine powder which is mixed with the α target material, as is done in AmBe, this source is a solid metal foil with a 2 μm thick Au cover. The ^{13}C is in the form of a solid graphite pellet, which is wrapped in a 1 μm

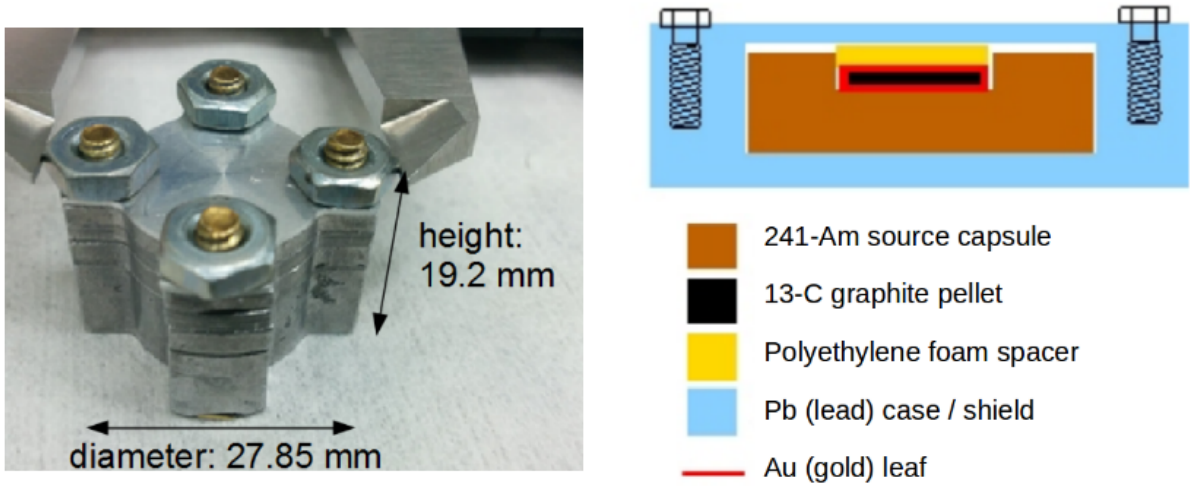

Figure 6.4: *Left*: Fully assembled source capsule. *Right:* Schematic of the AmC source components, viewed from the side.

high purity Au foil and placed in contact with the ^{241}Am capsule. The α's are attenuated by the gold prior to reaching the ^{13}C pellet, thus reducing their energy below the threshold required for gamma production.

The average neutron energy from AmC decay is 4.4 MeV, which is very close to the mean AmBe neutron energy. Unlike AmBe, however, the energy distribution is quite peaked, with an RMS of only 0.56 MeV (see Figure 6.5).

Characterization of the AmC Source

The AmC source was deployed in the LSV in December, 2015. At this time, the TPC had been filled with UAr. From calculations by SOURCES4A, the software program produced by Los Alamos National Lab, we expect a rate of a few neutrons per second, although analysis of the data shows a lower rate of less than 1 neutron per second. As can be seen in Figure 6.6, left, the rate of source-induced gamma-like interactions in the TPC is also considerably higher than was seen with the AmBe source.

We fit the δt prompt spectrum in the same manner as described for AmBe, and find a neutron capture time of $21.7\pm0.5\mu$s, in agreement with predictions (see Figure 6.6, right). Also as expected, the fraction of neutron-like events in the TPC which are correlated to the neutron capture signal is 98.5%. The correlated gamma fraction, however, is higher than expected: of gamma-like events, 75.2% are correlated, and 37.1% of all neutron capture events have a correlated gamma in the TPC. This correlated component may come from inelastic neutron interactions in the Pb shield, or the stainless steel of the source holder and cryostat. Such interactions would produce higher energy gammas which could trigger the TPC prior to the neutron capture. In the case that these

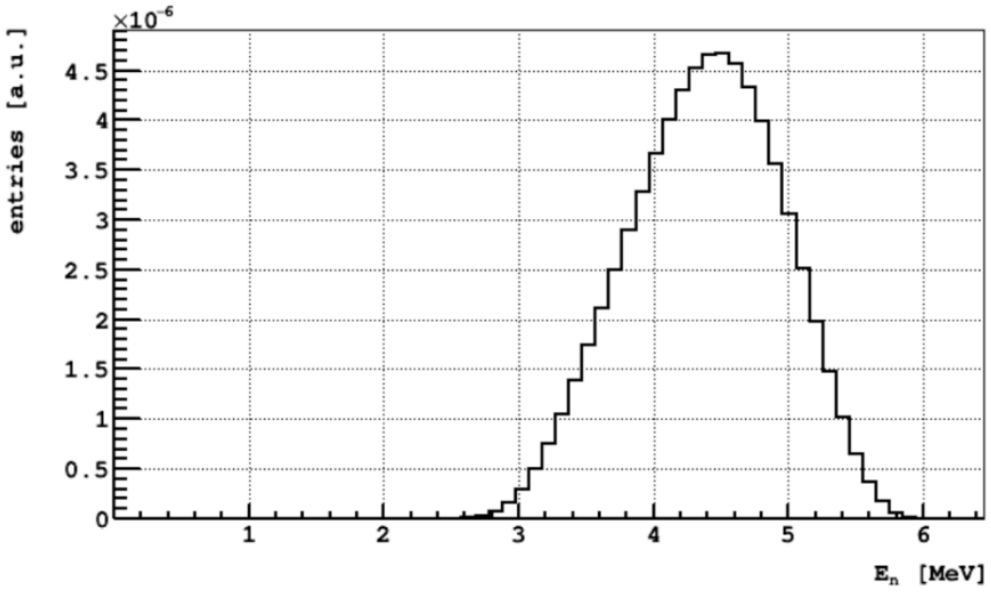

Figure 6.5: Neutron kinetic energy spectrum from ^{241}Am^{13}C.

are the sole source of the correlated gamma component, the rate of inelastic interactions would be markedly higher for AmC compared to the AmBe sources. This seems unlikely, given the cross sections for these interactions and the energy spectra of the sources. It is possible that, while the α's are sufficiently attenuated as whole, a tail of events reach energies above 5.05 MeV, yielding some energetic ^{12}C atoms and thus correlated gammas. This was seen in the Daya Bay experiment, for whom the addition of 1 μm of Au foil to the Au commercial cover removed the undesirable events.

As was pointed out by Bernd Reinhold, who first explored the correlated gamma component in the AmC source, the cyrostat complicates a clear characterization. This could be circumvented by deploying the AmC source in DarkSide-50's neighboring experiment, Borexino. The Borexino detector is a sphere filled with the scintillator pseudocumene, the same scintillator used in the LSV. By placing the source in the center of the detector, the only source of inelastic interactions would be the source holder itself. This would also allow for a clear determination of the neutron rate, as well as provide a dataset for the calibration of the Borexino detector.

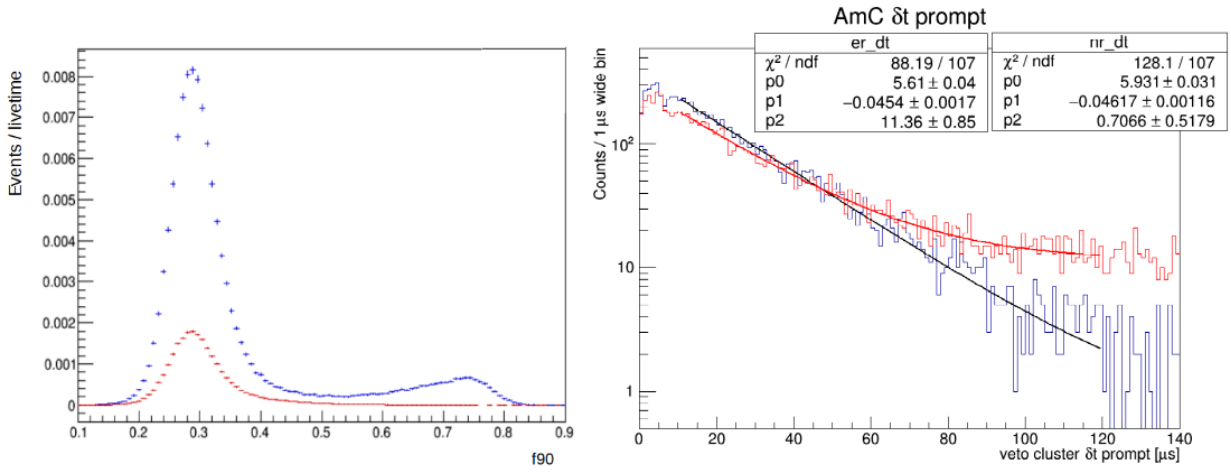

Figure 6.6: *Left:* The f_{90} distribution for the AmC source. The inherent UAr background, shown overlaid in red, has been statistically subtracted. *Right:* δt prompt spectra for gamma-like (er_dt, red) and neutron-like (nr_dt, blue) events, after selecting on the neutron capture signal. Each has been fit with an exponential plus a constant term.

6.2 Nuclear Recoil Optimized Event Selection

While electron recoils may be calibrated by the large sample of β interactions available from AAr data, nuclear recoil calibrations are contaminated by this same background, as well as source-induced gamma interactions. This is particularly true for lower energy events (less than approximately 100 PE in S1) where the electron and nuclear recoil f_{90} bands overlap. By restricting the focus to higher energy events, this contamination can be avoided. However, the ability to study the behavior of nuclear recoils in the low energy region, where most WIMP interactions are expected to occur, is then impaired. As was described in Section 5.3, this issue was encountered during the DarkSide-50 UAr analysis, during which the electron recoil contamination presented difficulties in fitting the nuclear recoil band in order to determine the WIMP accceptance. The challenge for nuclear recoil calibration, therefore, is to obtain a pure sample of nuclear recoils.

Neutron generators are an attractive option for this purpose. These small particle accelerators produce neutrons by either deuterium-deuterium or deuterium-tritium fusion:

$$D + D \rightarrow n\ (14.1\ \text{MeV}) + {}^4He$$
$$D + T \rightarrow n\ (2.5\ \text{MeV}) + {}^3He$$

In addition to producing mono-energetic neutrons, these devices can provide an event tag by detecting the charged helium nuclei emitted coincident with the neutron production. Requiring this tag to be present eliminates events which are triggered on background sources and thus produces a sample of nuclear recoil events which is pure up to accidental coincidences.

There are several barriers to their use, however. Because the LSV provides such effective shielding, calibrating the TPC with neutrons requires the sources to bypass this shielding entirely and be placed as close to the cryostat as possible, within the LSV itself. Neutron generators are both relatively heavy and require a power source to operate. Thus, it is necessary to put infrastructure in place for their operation at the time of detector construction, or to introduce structural modifications, possibly after data taking has already begun. In the absence of such infrastructure, most experiments are restricted to traditional radioactive neutron sources, such as AmBe.

Because the LSV in DarkSide-50 is an active neutron detector rather than a passive shield, it affords the opportunity for an alternative tagging method. There are two methods that may be employed, depending on the neutron source used. In the case of AmBe, 60% of AmBe decays emit a 4.4 MeV gamma coincident with the neutron, which typically introduces a large background to calibrations with this source. Rather than hindering neutron calibration, however, by selecting events in which the correlated gamma deposits all of its energy in the LSV, it can be utilized as a tag and thus make an effective tool for background rejection.

For a neutron source such as AmC, which we do not expect to have a correlated gamma, the delayed 478 keV gamma from neutron capture on ${}^{10}B$ may be used as the event tag.

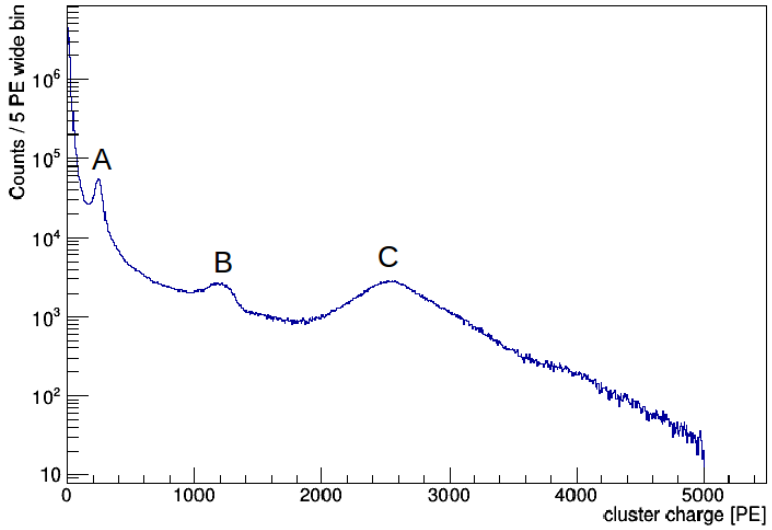

Figure 6.7: Energy spectrum of AmBe in the LSV. Region C is the 4.4 MeV gamma produced in 60% of neutron decays. Regions A and B are neutron capture peaks from capture on ^{10}B and ^{1}H at 478 keV and 2.2 MeV, respectively.

Figure 6.7 shows the energy spectrum of AmBe in the LSV. The large peak at approximately 2600 PE is the correlated 4.4 MeV gamma signal. Looking for this peak in the pre-prompt window, that is, the time before the prompt signal in the TPC, we can see in Figure 6.8, right, that its appearance is quite localized in time. This localization allows for the selection of efficient cuts in the δt prompt-cluster charge plane.

This technique was first investigated using the low-activity (10 n/s) AmBe data taken during the February, 2015 calibration campaign. The event selection cuts were optimized by looping over all possible cuts in the δt prompt-cluster charge plane, for charge values between 2000 and 3500 PE and δt prompt values between -0.05 μs and 0.03 μs, with the goal of maximizing the mean f_{90} value in the f_{90}-S1 plane. Additionally, it was required that the selection window be at least 10 ns wide in time and 250 PE wide in charge, and that at least 1000 events met the selection criteria. The optimal mean f_{90} found from this work was obtained by requiring the presence of a cluster in the veto between 20 and 30 ns before the TPC prompt and with a charge between 2000 and 3000 PE. Of the two cuts, one on the time window and one on the charge, the time cut is by far the most effective: excellent background mitigation is achieved with this cut alone, with the charge cut contributing a modest improvement (see Figure 6.24). Figure 6.9 shows the f_{90}-S1 plane before the application of event selection (left), and after (right). Almost all of the electron recoil background has been removed, making the low energy nuclear recoil f_{90} region clearly visible. Figure 6.10 shows the f_{90} distribution for S1 values between 20 and 440 PE. Before event selection (left), the spectrum is almost completely dominated by β interactions from ^{39}Ar. After event

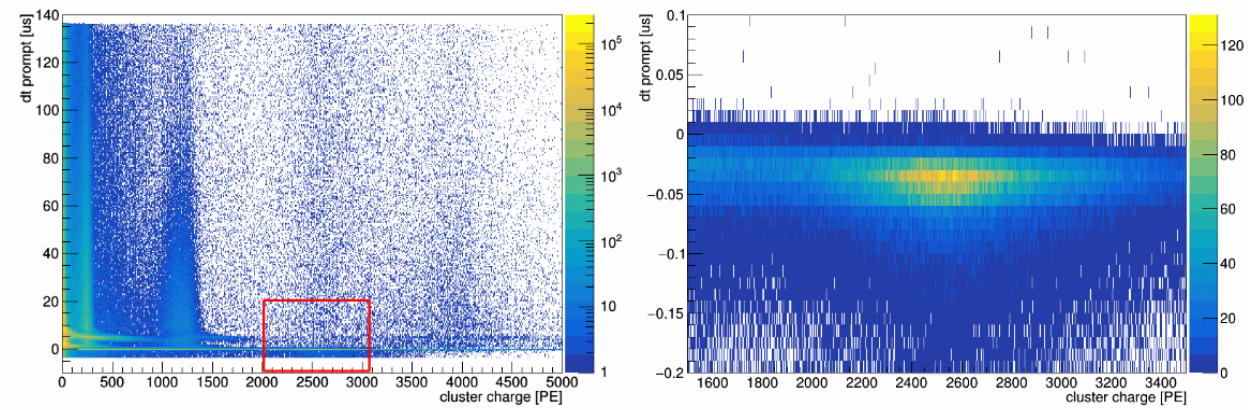

Figure 6.8: *Left*: The time difference between the prompt signal in the TPC and the veto cluster is shown versus the veto cluster charge. The neutron capture peaks at approximately 250 and 1100 PE are clearly visible. The red box indicates the region where the correlated gamma is seen. *Right*: A closer look at the correlated gamma region reveals its localization in time, appearing in the pre-prompt window with a spread of less than 1 tenth of a microsecond.

selection (right), only a tiny fraction of electron recoil events remain. This method is superior to standard background subtraction methods, in which a background spectrum is recorded without the calibration source present and used to statistically remove non-source induced events, because radioactive neutron sources have high rates of both correlated and uncorrelated photons which cannot be thus separated. This can be clearly seen by comparing the results of event selection in Figure 6.10, right, to statistical background subtraction for the same source, shown Figure 6.2, left.

In the case of AmC, without a correlated gamma, the delayed 478 keV gamma from neutron capture on ^{10}B provides the best event tag. The LSV energy spectrum from this source can be seen in Figure 6.11, with the capture peak visible at approximately 250 keV. Following the procedure used for AmBe, we look for this peak as a function of time relative to the prompt signal in the TPC (see Figure 6.12). Unlike the correlated gamma tag used for AmBe, the neutron capture signal is distributed in time, with a tail extending beyond 50 μs. The selection criteria which produced the optimal mean f_{90} value was found by requiring a veto cluster between 50 ns and 30 μs after the TPC prompt, with a charge of 220 to 270 PE. Figure 6.13 shows the f_{90}-S1 plane before event selection (left), and after (right). As with AmBe, the low energy f_{90} region is revealed following removal of background events via event selection. Although excellent electron recoil background mitigation is achieved, however, due to a lack of such a narrowly peaked tag it is not at the level obtainable with AmBe. This can also be seen in Figure 6.14, right, where a larger residual electron recoil band remains after event selection than in seen in AmBe data.

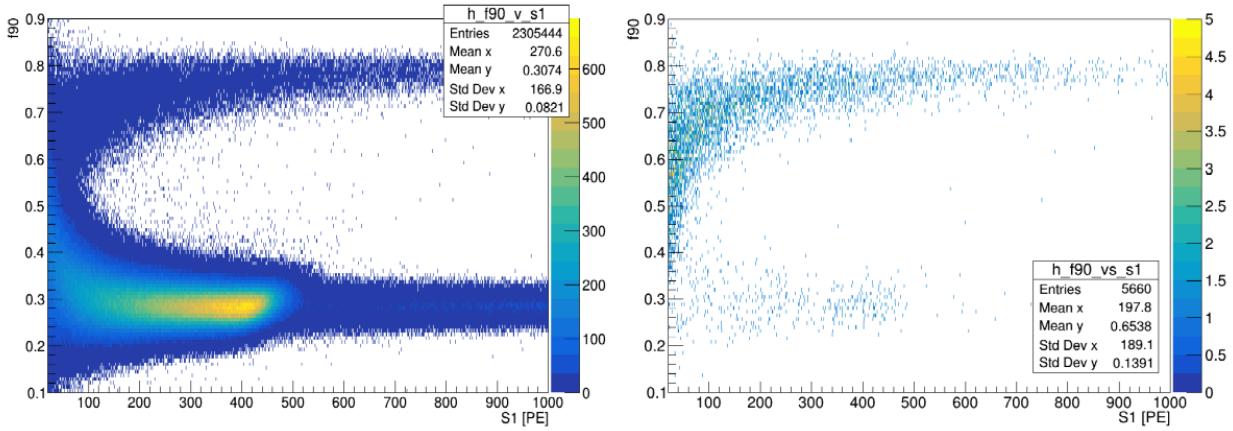

Figure 6.9: *Left:* Distribution of f_{90} vs S1 for AmBe 10 n/s data taken in February, 2015, before application of veto event selection. The vast majority of events are in the electron recoil band from AAr. The sudden decrease in entries in the ER band for values of S1 above 450 to 500 PE is due to applying a prescale and is not a feature of the source. *Right:* The same data after applying veto event selection. Note the increase in the mean f_{90} value from 0.307 to 0.654, consistent with the vast majority of remaining events being from nuclear recoils.

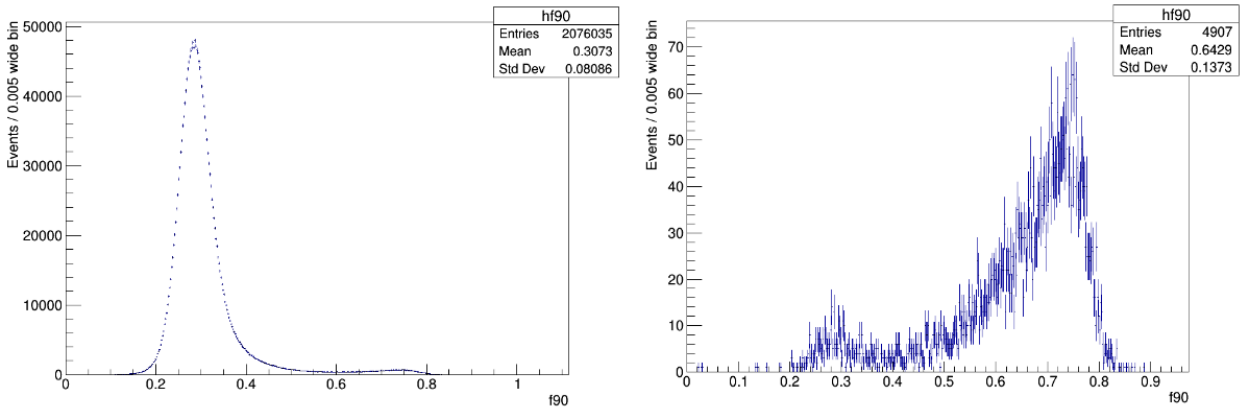

Figure 6.10: *Left:* f_{90} distribution of AmBe in AAr for values of S1 between 20 and 440 PE. The spectrum is strongly dominated by the rate of AAr events. *Right:* After event selection, almost all of the electron recoil band is removed, producing a much more pure neutron sample than is possible with traditional background subtraction (for comparison, see Figure 6.2, left).

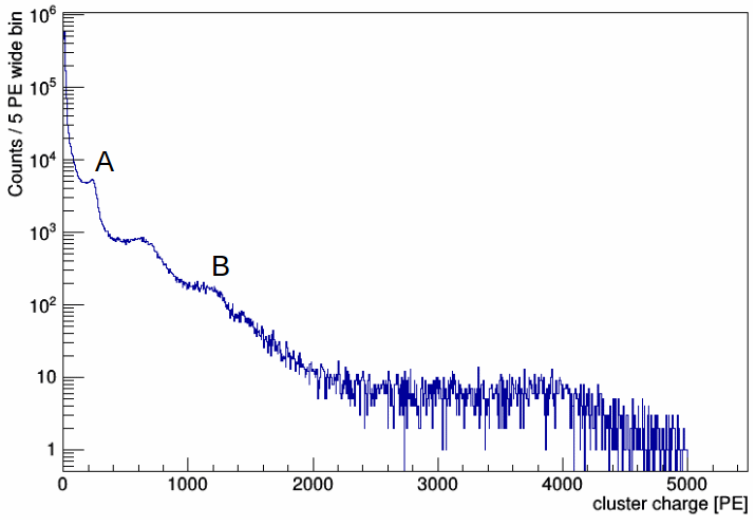

Figure 6.11: Energy spectrum of AmC in the LSV. Region A is the peak due to the neutron capture on ^{10}B. Region B is the ^{1}H neutron capture peak. The peak at approximately 600 PE is due to ^{60}Co in the intrinsic LSV background (see Section 4.1).

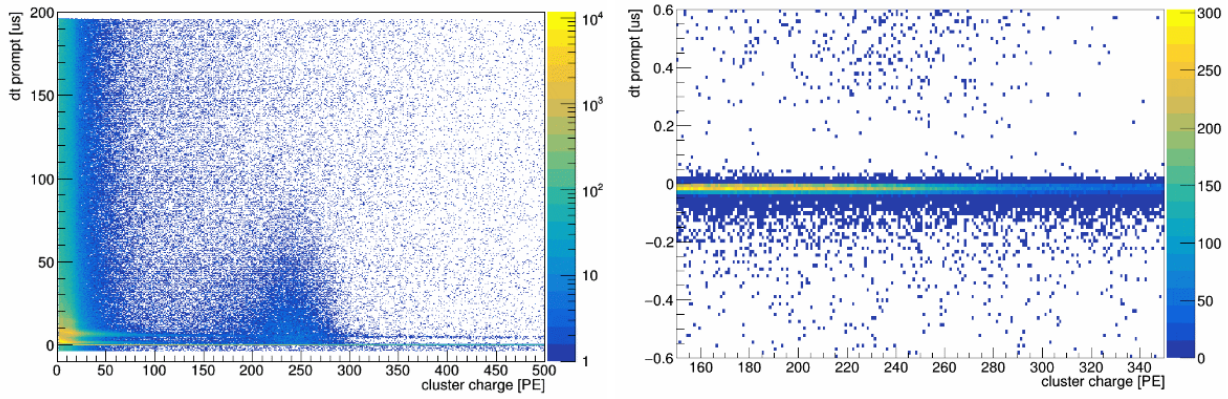

Figure 6.12: *Left:* Time distribution of clusters from an AmC source in the veto relative to the prompt TPC signal versus cluster charge. The neutron capture signal of interest is seen at approximately 250 PE. *Right:* A close look at the prompt region reveals a large number of clusters which are not associated with the capture signal. These are excluded by requiring the capture window to be at least 0.05 μs after the TPC prompt.

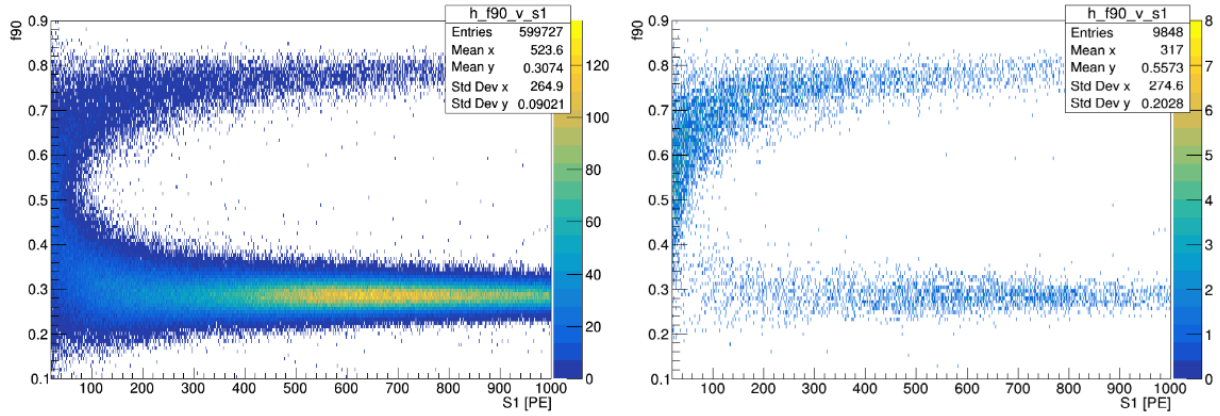

Figure 6.13: *Left:* Distribution of f_{90} vs S1 for AmC data taken in UAr, before application of event selection. Like AmBe, the spectrum is strongly dominated by electron recoil events. Rather than being from β decay, however, this band is predominantly composed of gamma interactions, both from the inherent detector background and from the source itself. *Right:* The same data after applying veto event selection. While there is a large reduction in the electron recoil background, revealing the low energy region of the nuclear recoil band, this method is more efficient for a correlated gamma source such as AmBe.

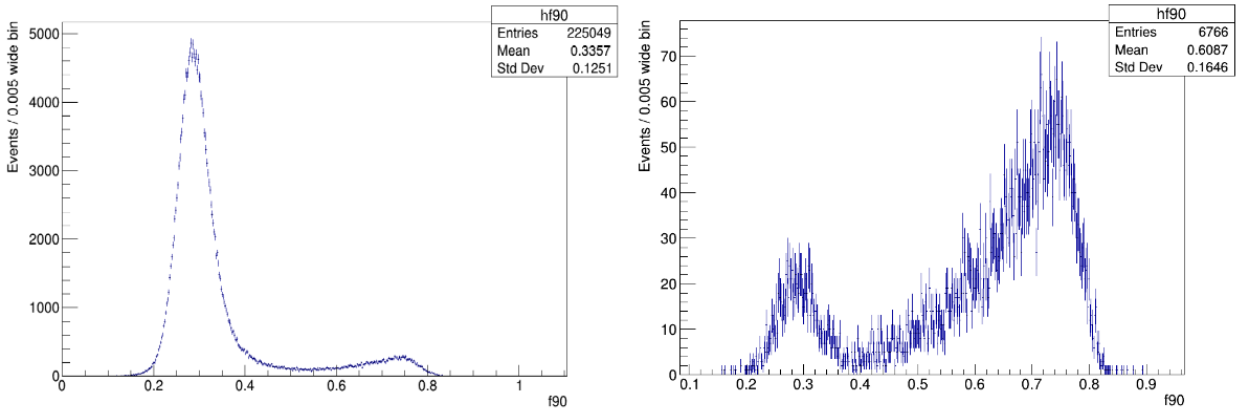

Figure 6.14: *Left:* f_{90} distribution of AmC in UAr for values of S1 between 20 and 440 PE. *Right:* After application of event selection cuts, most of the electron recoil band has been removed, leaving a remnant peak in the background region.

6.3 TPC Calibration with AmBe

Following the success of the event selection techniques described above in removing the obscuring electron recoil events, a new AmBe campaign was performed in June, 2016. The goal of this campaign was to obtain a larger statistics data set of nuclear recoils in UAr, primarily for the purpose of f_{90} studies. Because this campaign was to take place during a WIMP search period, a campaign lasting longer than approximately one week was not an option. Both the 10 n/s AmBe source and the AmC source had neutron rates which were too low to gather sufficient statistics in the time frame available. The 2000 n/s source, on the other hand, had such a high rate that it posed a significant risk to the PMTs, as well as to personnel. An AmBe source owned by the XENON collaboration, with an ideal mid-range activity of 160 n/s rate, was chosen for the calibration. As it was still possible that this rate would be too high for the PMTs, a 50 n/s source, owned by the Borexino collaboration, was selected as an alternative.

6.3.1 Looking for Evidence of Neutron Activation

Because the neutron campaign was to take place in the middle of a WIMP search, rather than at the beginning or end, as is standard, it was critical to verify that no radiation would be introduced from neutron activation. To check that this would be the case, data taken both during and immediately following previous AmBe campaigns was examined for signs of any effect. Because previous campaigns had not been planned with this study in mind, the data available which met the criteria was limited. During the February, 2015 AmBe campaign, data was taken immediately following the removal of the source from the LSV, with the source still inside the organ pipe. The LSV had the same 5% TMB concentration at the time of the campaign as at the time of this study, allowing a direct comparison of the LSV energy spectra to see if any peaks were visible which would indicate the presence of shorter-lived isotopes from the neutron source, which had then decayed away. No indication of additional radioactivity was found. Additionally, the TPC data taken at this time did not contain any events in the nuclear recoil band. Because it was possible that the low 10 n/s source rate was not high enough to induce noticeable effects, data from the 2000 n/s AmBe source was also examined. There was a 3 hour window between the time of source removal and the first available data, making it impossible to look for very short lived isotopes. The data was also taken with the TPC at null field, and the LSV had a negligible TMB concentration. However, any added radiation which decayed following the removal of the source should produce an effect on the trigger rate. Figure 6.15 shows a plot of the trigger rate in the TPC as a function of time after the source was removed. As can be seen, the variation in the trigger rate is consistent with zero.

A search was also performed for the ^{41}Ar line from neutron captures on ^{40}Ar. ^{41}Ar has a half-life of 109 minutes, and decays with the emission of a 1294 keV γ. At this energy, we should see a peak in the S1 spectrum at approximately 8,000 to 10,000 PE. For the 10 n/s source, which had a

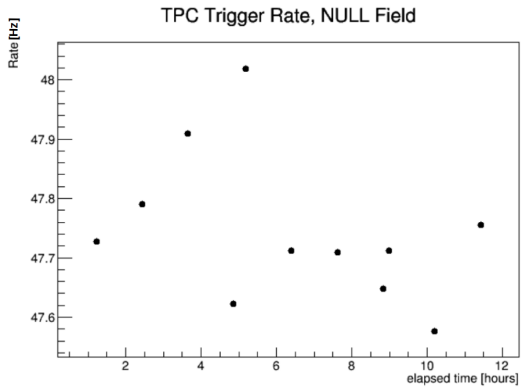

Figure 6.15: The trigger rate in the TPC, as a function of time following the removal of the source. The variation in the rate is consistent with zero.

total source-induced trigger rate in the TPC of 2 Hz, we would expect that in the time immediately following the removal of the source, ∼13 decays would be seen in the TPC. This is actually an overestimation, because it assumes all source-induced triggers in the TPC result from neutrons, whereas in fact there is a mix of neutron and gamma interactions. The best chance of seeing this peak, therefore, is during actual source running.

A small peak was observed in the 10 n/s AmBe data (see Figure 6.16). No evidence of this peak was seen in any other neutron calibrations.

As a result of this study, we conclude that the introduction of an AmBe source does not result in any lasting effects from neutron activation, which may modify the known backgrounds and thus be detrimental to the ongoing WIMP search.

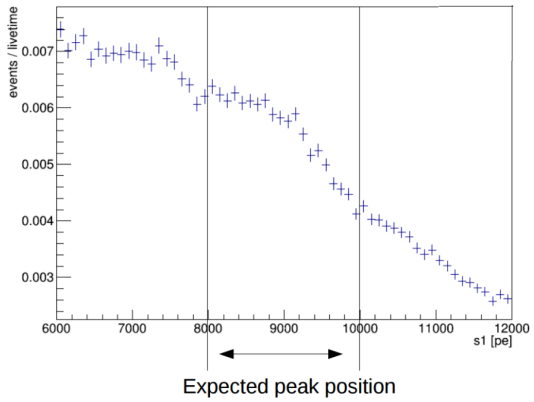

Figure 6.16: S1 spectra in the TPC, in the energy range corresponding to ^{41}Ar decays. This data represents 5.8 live days of AmBe data, during which time 500 to 1000 decays are expected, based on a rate of 1 to 2 neutrons in the TPC per second.

6.3.2 Estimating the Fraction of Electron Recoil Events in the Nuclear Recoil Band via Monte Carlo Simulation

Since the goal of this campaign was to obtain a more statistically significant nuclear recoil sample, it is important that we ensure the events remaining after the selection criteria are applied are, in fact, nuclear recoils, and not low energy electron scatters. It is instructive, therefore, to make an estimation of the level of electron recoil contamination that remains in the nuclear recoil band, after veto event selection. Prior to the June, 2016 AmBe campaign, a Monte Carlo study was performed for this purpose. In addition to estimating the number of pure electron recoil events contaminating the nuclear recoil band, this study also attempted to determine the fraction of events which were mixed, that is, had both electron and nuclear recoils occurring such that they would be reconstructed as a single event. Along with inelastic scatters, these types of events are expected to be the source of the population of mid-f_{90} events, which fall between the electron and nuclear recoil bands.

Using the full spectrum of the g4ds AmBe generator described in Section 3.3, 1 M AmBe decays were generated. The source was placed just outside the cryostat, in a position similar to that of the actual source. The decays were produced with an isotropic distribution. Rather than simulating the optics, which is CPU intensive, estimates were made based on the energy deposits. In order to imitate the resolution and reconstruction effects of the TPC, energy deposits which were within 200 ns and $\Delta Z < 2$ cm were clustered together, with no radial criteria. Each cluster approximated a single pulse in the TPC. In the veto, clusters were formed by any energy deposit within 20 ns of each other, with no spatial cut.

Figure 6.17 shows the simulation output, compared to data. In order to mimic the veto event selection process outlined above, cuts were chosen in the veto δt prompt-cluster energy plane. For each event included in the analysis, we require a cluster in the veto with an energy between 4000 and 6000 keV (corresponding to a signal in the veto 2000 to 3000 PE), which occurs prior to the prompt signal in the TPC (δt prompt < 0). Because optics and electronics effects were not simulated, it is not possible to have as stringent event selection criteria in the Monte Carlo as in data. Thus, we can expect that the level of electron recoil contamination predicted will be higher. Nevertheless, we acquire an estimate which will serve as an upper limit and be useful for comparison to model predictions, to be shown in Section 7.3.1.

To separate classes of events (nuclear recoil, electron recoil, or mixed), in each cluster we count the number of "neutron-like" and "electron-like" energy deposits. A "neutron-like" signature is any deposit made by a particle with a Particle Data Group (PDG) number greater than 30. For example, the PDG number for a neutron is 2112, and that of an argon nucleus is 1000180400. An "electron-like" signature is then any deposit made by a particle with PDG number less than 30 (electrons = 11, photons = 22). Results can be seen in Figure 6.18. For S1 energies up to $\sim$1300 PE, out of a total of 17531 qualifying events, 163, or 0.9%, were mixed. For S1 energies up to 100

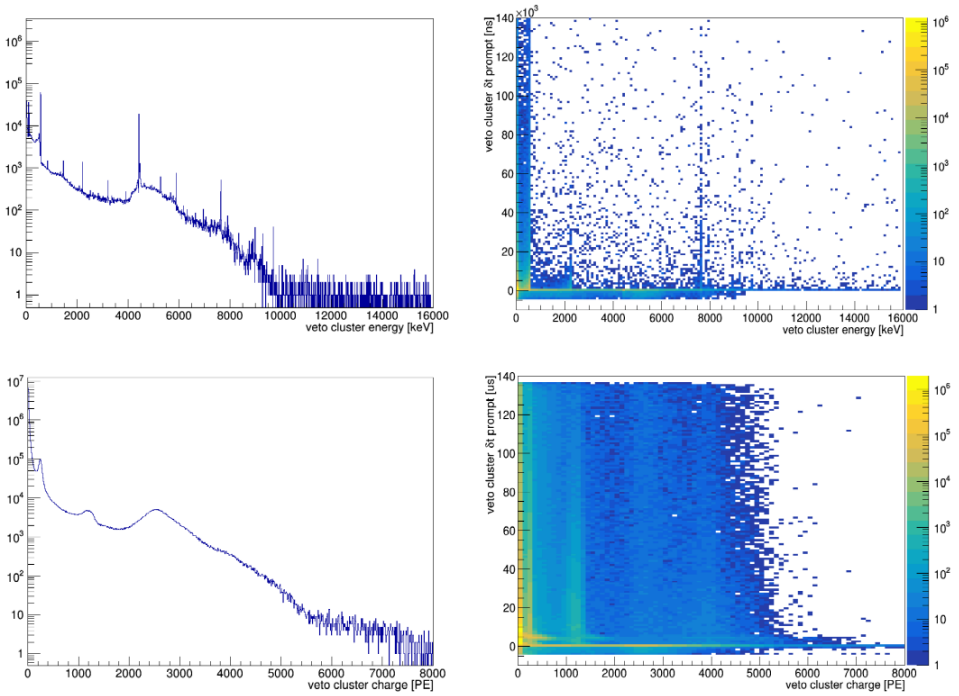

Figure 6.17: Comparison of veto cluster distributions from Monte Carlo (top) and data (bottom). A cluster energy of 4000 keV corresponds to a charge of ∼2000 PE in the veto.

PE, where the f_{90} bands overlap, the ratio of electron to nuclear recoil events was 0.16, and the fraction of mixed events was 0.002.

One drawback to this study is that it does not discriminate between energy deposits from elastic and inelastic interactions. The reason for this is because, at the present time, g4ds does not track the process which produces each energy deposit. Future studies with the goal of examining the fraction of inelastic scatters will require the addition of this information to the DarkSide Monte Carlo.

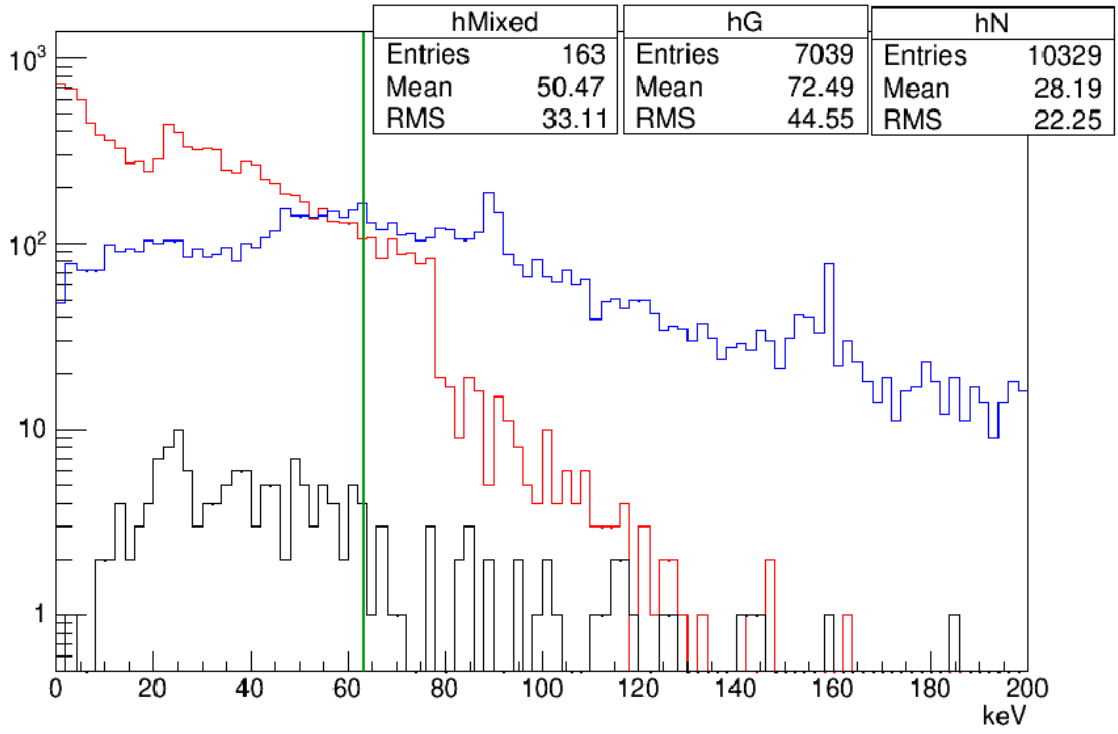

Figure 6.18: Energy of clusters in the TPC from AmBe Monte Carlo. Nuclear recoil events are indicated in red (statistics box labeled hN), electron recoil events are shown in blue (hG statistics box), while mixed events are shown in black. The green line shows the approximate position of the upper edge of the WIMP search box. The full scale of 0 to 200 keV represents a range up to ∼1300 PE in S1.

6.3.3 June, 2016 Campaign

Proposal and Run Plan

Prior to the start of data taking, a detailed plan was created for all aspects of the campaign. The source would be placed at the nominal central TPC position (CALIS motor step value of 731000), in contact with the cryostat. Pb shielding would be included in the source holder, as in earlier campaigns, to attenuate the 60 keV photons produced at a high rate by ^{241}Am. A prescale of 33 would be applied to all events with a trigger digital sum (TDS) greater than 250 and less than 1200, corresponding approximately to S1 values between 450 and 2400 PE. Thus, for events in this energy range, only every 33rd trigger would be allowed, preventing the trigger rate from becoming too high for the DAQ. This prescale primarily affects gamma events, which have substantially higher S1 values relative to neutrons for recoils of the same energy. The LSV would operate in slave mode, so that all events were triggered on the TPC. Finally, because saturation is not an issue for the energy range of interest, the V1724 digitizers would not be used, markedly reducing the amount of disk space required for the campaign.

Based on the AmBe data from the February, 2015 campaign, which had a source-induced trigger rate of 2 Hz in the TPC and used the same prescale values, we expected a rate from the 160 n/s source of 32 Hz. For S1 energies between 20 and 400 PE, 48% of all events in the earlier AmBe data were neutron-like, ie: had an f_{90} value of greater than 0.45. Therefore, we expect to accumulate a total of $\sim$8 M nuclear recoils in 6 days of running, with $\sim$1.2 M between 20 and 400 PE in S1 surviving all analysis cuts. Should it have become necessary to use the 50 n/s source, these values would reduce to 5.2 M and 2.5 M, respectively.

Laser calibration runs were planned to occur every 6 hours, each lasting about 15 minutes, or about an hour per 24 hour period. When accounting for the time to prepare the source, the insertion (removal) of the source into (from) CALIS, pumping and purging the system with N_2, and the time to deploy (retrieve) the source, an additional 20.5 hours were envisioned to be required for the campaign. The total amount of disk space needed for the data was calculated to be 30 Tb. This was also the maximum amount of space available for the campaign, so was a hard limit.

In order to "rest" the PMTs, they are routinely shut down overnight once per month. Since the high source rate was expected to be taxing for the PMTs, this shutdown was scheduled immediately following the removal of the source. Finally, one day of unblinded data taking was planned both before and after the campaign, in order to record any background effects (the current WIMP search is operating in "blinded" mode, meaning that the expected signal region is masked from analyzers).

Source Insertion and Data Taking

On Monday, May 30th, 2016, both the 160 n/s of 50 n/s AmBe sources were brought into Hall C at LNGS. During the evening, the 160 n/s source was deployed. After articulating the source arm,

pictures taken from within the LSV showed that the arm was not horizontal, due to a kink in the cables (see Figure 6.19). After several attempts to release this kink and articulate the arm were unsuccessful, the source was deployed to it fullest length overnight in order to release any tension in the cables.

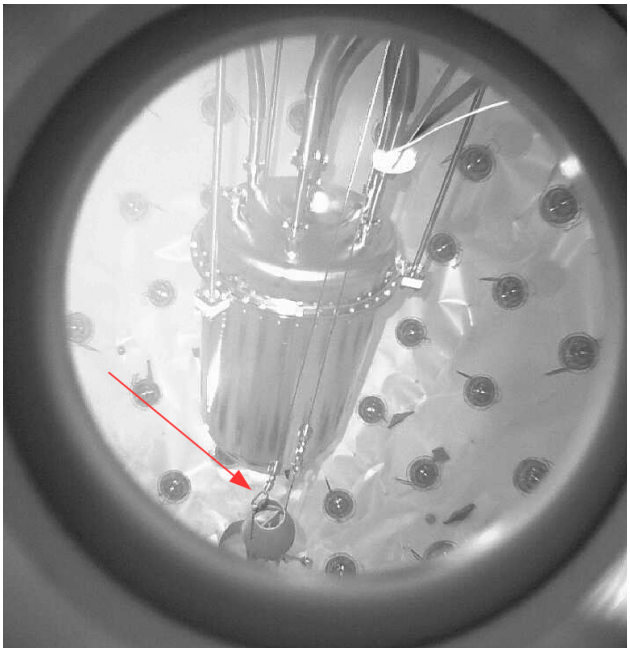

Figure 6.19

On Tuesday, May 31st, after some effort, the source was positioned against the cryostat wall, in a position lower than in previous campaigns. The PMT rates initially increased, and then remained stable for ∼3 hours, before decreasing approximately 25% (see Figure 6.20). The reason for this decrease was hypothesized to be due to the cables relaxing, and thus shifting the position of the source. While it would have been possible to verify this by photographing the source inside the LSV, the use of the cameras necessitates turning the LSV PMTs off, both during the photo taking and for a period of 3 hours afterwards. Since the rates remained stable, the loss in data taking time was not deemed justifiable.

The high rate initially caused several crashes of the ODAQ. To mitigate this, the majority trigger in the TPC was changed from 2 to 3, and the veto data acquisition gate was shortened from 200 μs to 140 μs. Additionally, the prescale was modified to include all events with TDS values greater than 250.

Data taking continued from Tuesday, May 31st, until Wednesday, June 8th. At the end of the campaign, photos were taken of the source position, verifying that the source had, indeed, shifted slightly away from the cryostat, leading to the decrease in PMT rates (see Figure 6.21). The shift in position led the trigger rate to be 10.5 Hz, rather than the expected 32 Hz. In total, 6.3 M

events were gathered, requiring about 10 Tb of disk space. For this source, ∼60% of events are neutron-like, with f_{90} values greater than 0.45. After all analysis cuts, 765,000 neutron events with S1 energies between 20 and 400 keV were recorded. Although this was less than originally planned, it represented a substantial improvement over previous campaigns.

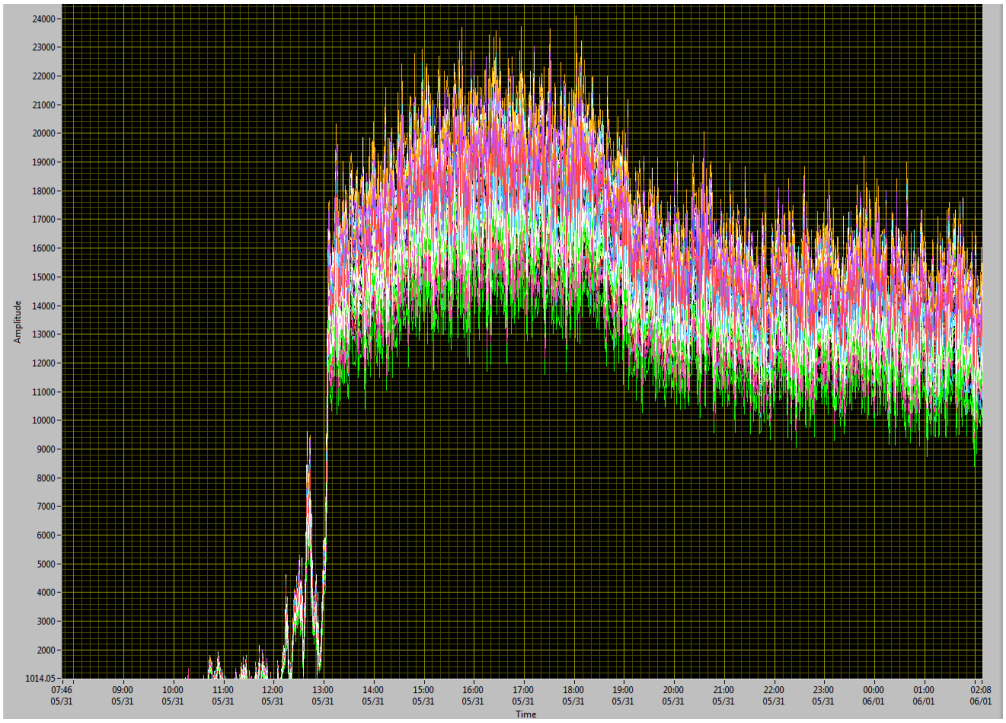

Figure 6.20: PMT rates during and after source insertion. The decrease beginning at 19:00 on May 31st is due to the source shifting position.

Characterization of the 160 n/s AmBe source

We proceed with an analysis of the higher activity AmBe data, following the procedure outlined in Section 6.1. The high source rate can be seen in Figure 6.22, left, which shows the f_{90} spectrum of this source, along with the comparatively tiny UAr background. Fitting the δt prompt spectrum (Figure 6.22, right) for neutron-like events yields a mean neutron capture time in the veto of $22.7 \pm 0.1\mu$s, consistent with the results of the previous campaign. As this campaign took place in UAr, which has a 1400 fold reduction in ^{39}Ar [39], we expect that most events in which a neutron was captured in the LSV but was triggered in the TPC by a gamma-like event to be caused by the AmBe source itself, and thus be correlated with the neutron. Taking the ratio of the exponential curve area to the total fitted area we find that, indeed, 94.8% of gamma-like events and 96.2% of neutron-like events are correlated. As with the 10 n/s AmBe source, out of all neutron capture events, 30.0% produced correlated gamma triggers in the TPC.

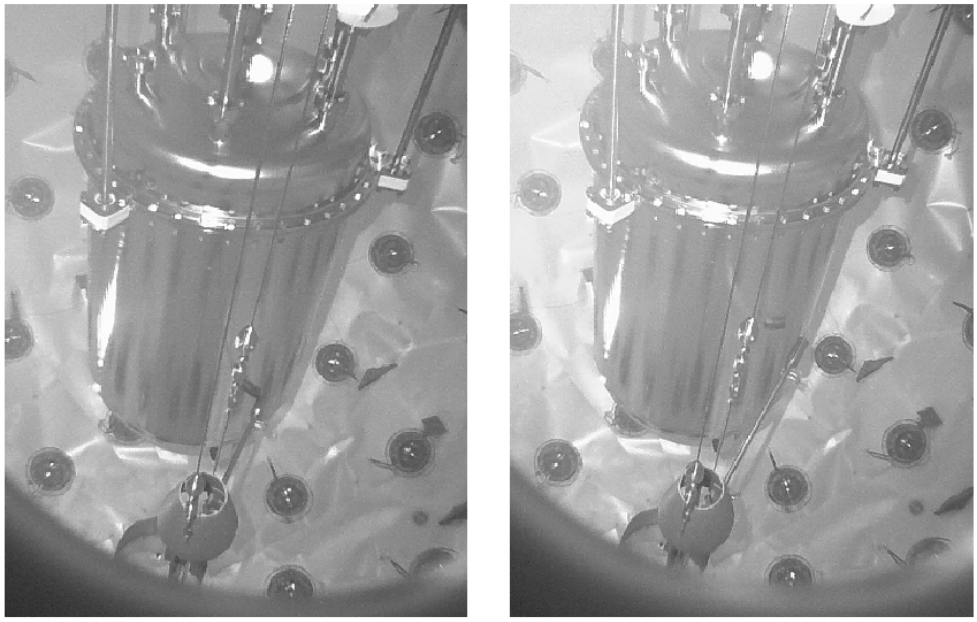

Figure 6.21: The position of the source at the start of the campaign (left) is compared with the position at the conclusion (right).

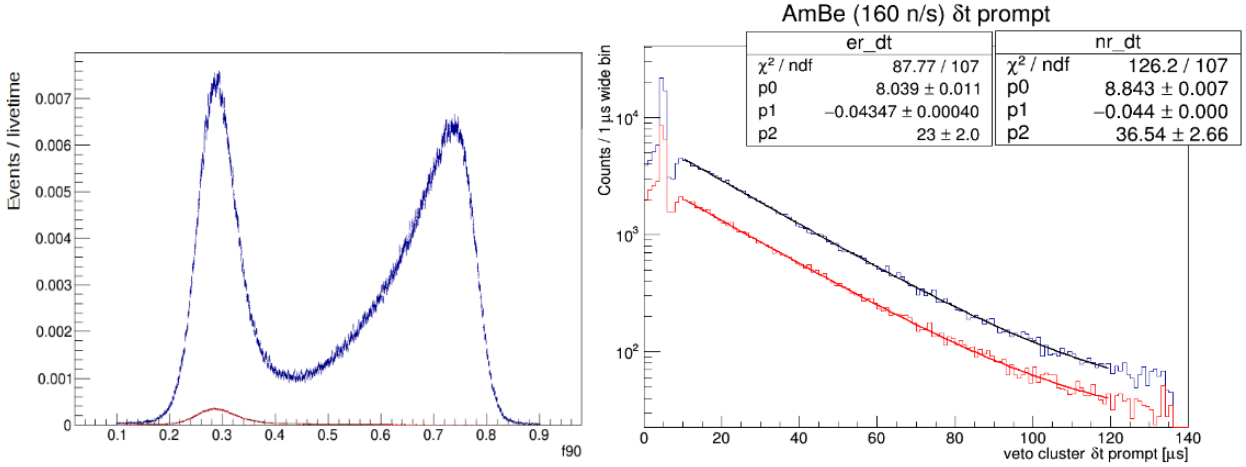

Figure 6.22: *Left:* The f_{90} distribution for the 160 n/s AmBe source. The background UAr spectrum is shown in red. *Right:* δt prompt spectra for gamma-like (er_dt, red) and neutron-like (nr_dt, blue) events, after selecting on the neutron capture signal. Each has been fit with an exponential plus a constant term.

6.3.4 Nuclear Recoil Optimized Event Selection

Nuclear recoil event selection was again utilized to obtain as pure a sample of nuclear recoils as possible from the 160 n/s AmBe data. To optimize selection criteria, rather than aiming for a maximum mean f_{90}, the goal was to minimize the ratio of events in the electron recoil band to those in the nuclear recoil band (see Figure 6.23). The reason for this change was the observation that at low energies, nuclear recoils have low f_{90} values. Thus, selection criteria which maximize the mean f_{90} value may bias the resulting nuclear recoil sample to higher energies. The optimal ratio was found to result from requiring a veto cluster between 40 and 50 ns before the TPC prompt, with a charge between 2400 and 3800 PE. Additionally, a small improvement (with minimal loss of statistics) was achieved by requiring that there was only one cluster in the pre-prompt window. As with the earlier AmBe data, excellent background removal is achieved with the selection on the time window alone, with modest improvement provided by the charge and single-cluster requirements. The efficacy of the time cut is demonstrated in Figure 6.24, which shows the ratio of electron recoil to nuclear recoil events as a function of the minimum time requirement. Figure 6.25 shows the f_{90}-S1 plane before application of event selection (left) and after (right), while Figure 6.26 shows the same for the f_{90} distribution for S1 values between 20 and 440 PE. As with the earlier AmBe campaign, the vast majority of the substantial electron recoil band, in this case almost entirely source-induced, is removed. This data also benefits from the substantially higher source rate, yielding a sample of nuclear recoils for f_{90} distribution studies which is an order of magnitude larger than was previously available.

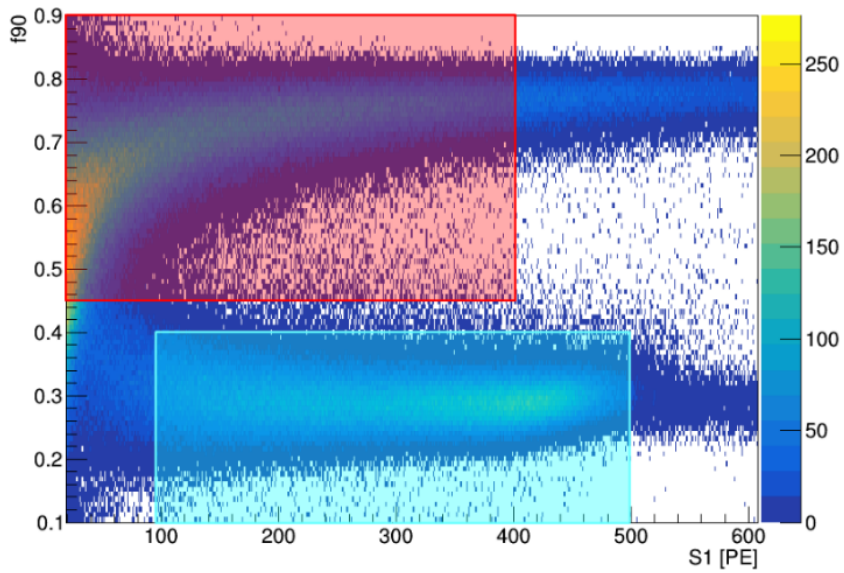

Figure 6.23: Event selection criteria for the most recent AmBe calibration data were chosen by requiring the minimum ratio of electron recoil events (light blue box) to nuclear recoil events (red box).

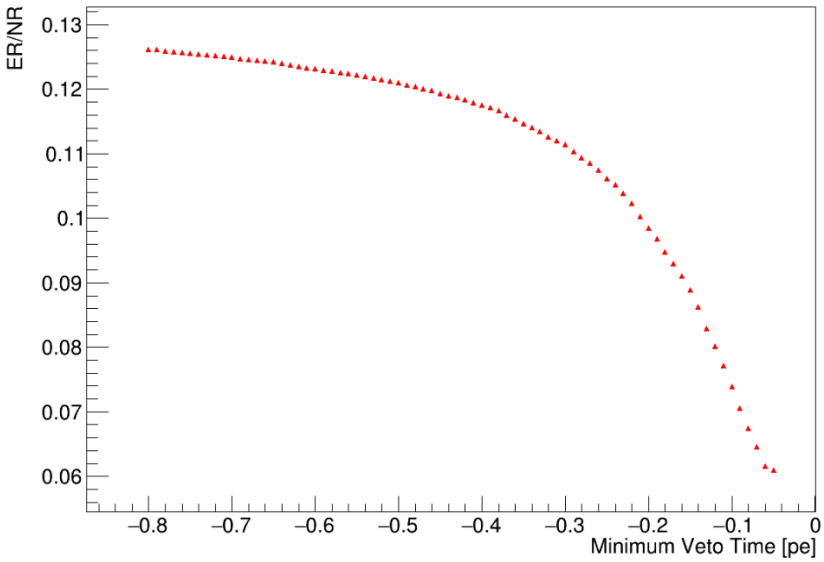

Figure 6.24: Illustration of the effect of the δt prompt selection criteria. The ratio of electron recoil to nuclear recoil events (light blue and red boxes in Figure 6.23, respectively) is shown as a function of the minimum time cut in the veto. Here the cluster charge requirement has already been applied. The maximum veto δt prompt time is held constant at -40 ns. The fraction of electron recoil events relative to nuclear recoils decreases to a minimum for a δt prompt value of -50 ns.

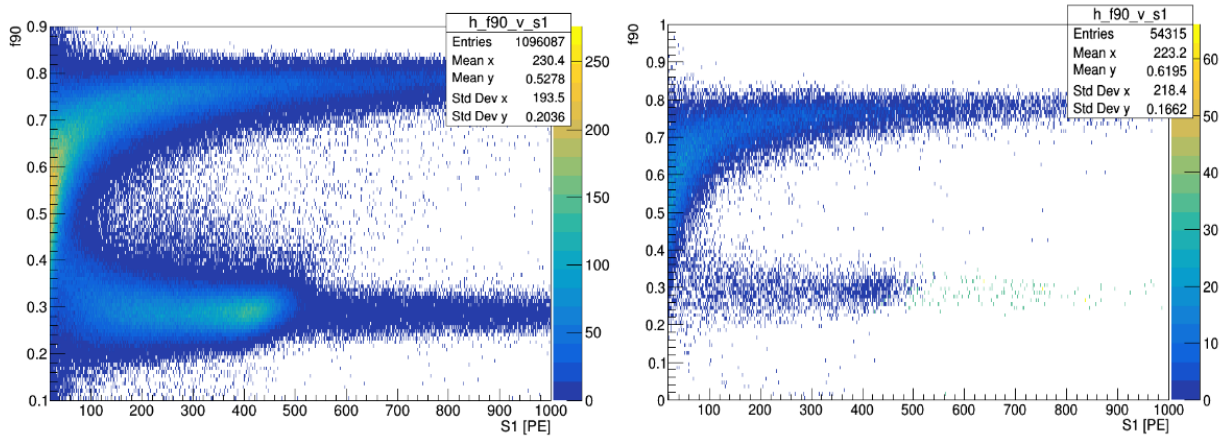

Figure 6.25: *Left:* Distribution of f_{90} vs S1 for AmBe data taken in UAr, before application of event selection. For this calibration, the same prescale was used as in the previous AmBe campaign, which is the source of the loss of statistics in the electron recoil band for values of S1 larger than approximately 450 PE. *Right:* After application of event selection cuts, the majority of the background events have been removed.

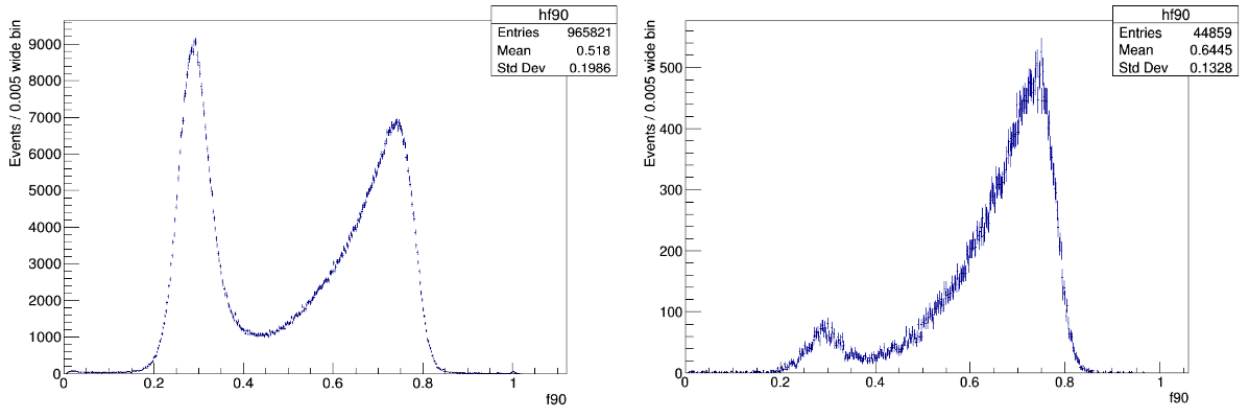

Figure 6.26: *Left:* f_{90} distribution of AmBe in UAr for values of S1 between 20 and 440 PE. *Right:* After application of event selection cuts, most of the electron recoil band has been removed.

CHAPTER 7
NUCLEAR RECOIL F_{90} DISTRIBUTION

7.1 Analytical f_{90} Models

Two analytical f_{90} models are currently under consideration for use in DarkSide-50: the Hinkley model, and the Covariance (or Tail) model. The Hinkley model has been used in all DarkSide publications to date. Both are described below.

7.1.1 The Hinkley Model

The Hinkley model of f_{90}, also called the ratio of Gaussians model, has been used to describe the pulse shape discrimination statistic by multiple dark matter experiments utilizing liquid argon [30] [50] [52] [53]. In this model, the number of prompt and late photoelectrons, N_p and N_l, are assumed to be independent random variables, normally distributed with means μ_p and μ_l and variances σ_p^2 and σ_l^2. Their sum, then, N_{tot}, is also a normally distributed random variable, with mean $\mu_{tot} = \mu_p + \mu_l$ and variance $\sigma_{tot}^2 = \sigma_p^2 + \sigma_l^2$. Thus, in this model f_{90} is the ratio of two normally distributed random variables, N_p and N_{tot}, with correlation:

$$\rho = \frac{\sigma_p}{\sigma_{tot}} = \frac{\sigma_p}{\sqrt{\sigma_p^2 + \sigma_l^2}} \tag{7.1}$$

The distribution of such a ratio has been thoroughly described by D. V. Hinkley [54], for whom the model has been named. We use the approximation to the full probability density function:

$$g(x) = \frac{\mu_p x \sigma_l^2 + \mu_l (1-x)\sigma_p^2}{\sqrt{2\pi (x^2\sigma_l^2 + (1-x)^2\sigma_p^2)^3}} \exp\left[- \frac{(\mu_l x - \mu_p(1-x))^2}{2(x^2\sigma_l^2 + (1-x)^2\sigma_p^2)} \right] \tag{7.2}$$

where x is the f_{90} variable. We recover the fit parameter, $\hat{f}_p$, the mean f_{90} value, by rewriting μ_p and μ_l as:

$$\mu_p = \mu_{tot}(\hat{f}_p) \tag{7.3}$$

$$\mu_l = \mu_{tot}(1 - \hat{f}_p) \tag{7.4}$$

In order to apply this model to the DarkSide-50 data, the σ_p^2 and σ_l^2 terms are written to explicitly include the known contributions to the spread of the number of photoelectrons. These contributions include Poisson counting statistics, the width of the PMT single photoelectron response, the spread due to the TPB, and electronics and reconstruction effects (see Section 7.2). The prompt and late variances are then:

$$\sigma_p^2 = \mu_p(F + \sigma_{TPB}^2 + \sigma_{SPE}^2) + \sigma_{elec,p}^2 \tag{7.5}$$

$$\sigma_l^2 = \mu_l(F + \sigma_{TPB}^2 + \sigma_{SPE}^2) + \sigma_{elec,l}^2 \tag{7.6}$$

The Hinkley model as applied to electron recoil data in DarkSide-50 has parameters: μ_{tot}, $\hat{f}_p$, σ_{TPB}, σ_{SPE}, $\sigma_{elec,p}$, $\sigma_{elec,l}$, the Fano factor, F, and an overall normalization. The value of μ_{tot} is fixed to the mean of the S1 bin being fit. The Fano factor is fixed to 1, the standard value for a Poisson process (it is explicitly listed here purely for historical reasons). The SPE resolution is taken from the laser calibration and fixed to $\sigma_{SPE} = 0.4$, while the TPB value, modeled as a Poisson process, is fixed to $\sigma_{TPB} = 0.47$. The values of $\sigma_{elec,p}$ and $\sigma_{elec,l}$ are taken from high statistics studies of the single-sited β interactions from AAr data and are also fixed. Thus, in this application the model has only 2 free parameters: the mean f_{90} value, $\hat{f}_p$, and the normalization. While this produced good fits to the electron recoil data for the purpose of establishing leakage curves, it was a poor fit to nuclear recoil data. A good fit of the model to nuclear recoil data is recovered by recasting it with 4 free parameters: $\hat{f}_p$, σ_p^2, σ_l^2 and the normalization (see Section 7.3).

This model is known to overestimate the tails of the fitted f_{90} distributions, particularly at low energies [30]. The reason for this is because, although Eqn 7.2 is expressed in terms of N_{tot}, the true number of photoelectrons, in practice the model is fit to f_{90} distributions which have been binned in S1, the reconstructed number of photoelectrons. In order to perform the fit, the value of S1 is fixed to the mean of the bin. Each bin, then, contains events with a range of values of N_{tot}. Because the overestimation is a conservative effect, and due to the fact that, for data which in unconstrained in S1, ie: the full range of the f_{90} distribution, the Hinkley model does describe the correct statistics, the Hinkley model has continued to be employed to establish electron recoil leakage limits.

7.1.2 The Covariance Model

The Covariance (or Tail) model was proposed by Davide Franco and Paolo Agnes to address the tail overestimation by the Hinkley model [55]. In this model, f_{90} is also assumed to be the ratio of two random variables, P, the prompt signal, and P + L, the total signal. The key difference is the constraint:

$$P + L = S1$$

which reflects the actual process of fitting the model to data, wherein we fix the S1 value to the mean of the bin. As a result of this constraint, the variables P and L are fully anti-correlated, with correlation -1 and a covariance given by:

$$Cov(P, L) = -\sigma_p \sigma_l \tag{7.7}$$

We can then parameterize P and L as functions of the f_{90} variable, x:

$$P = xS1$$
$$L = (1-x)S1$$

and determine the model variance from the relation:

$$Var\big(f(P,L)\big) = \left(\frac{\delta f}{\delta P}\right)^2 Var(L) + \left(\frac{\delta f}{\delta L}\right)^2 Var(P) + 2\left(\frac{\delta f}{\delta P}\right)\left(\frac{\delta f}{\delta L}\right) Cov(P,L)$$

The f_{90} variable, then, is distributed as:

$$g(x) = \frac{A}{\sqrt{2\pi}\sigma} \exp\left[-\frac{(x-\hat{f}_p)^2}{2\sigma^2}\right] \tag{7.8}$$

with width:

$$\sigma(x) = \frac{1}{S1}\sqrt{(1-x)^2\sigma_P^2 + x^2\sigma_L^2 + 2\sigma_P\sigma_L} \tag{7.9}$$

The variance of the prompt and late terms, σ_p^2 and σ_l^2, are assumed to be proportional to S1:

$$\sigma_P^2 = k_P^2 S1 \tag{7.10}$$
$$\sigma_L^2 = k_L^2 S1 \tag{7.11}$$

The empirical values k_P and k_L encompass all of the statistical effects, such as SPE and TPB variance, included in Eqns 7.16 and 7.17, without expressly associating the physical values, which are functions of the true number of photoelectrons and not the reconstructed S1. This model is then fit to the data with 4 free parameters: $\hat{f}_p$, k_P, k_L and the normalization constant, A.

7.2 f_{90} Variance

The width of the f_{90} distribution is determined by contributions to the variance of the S1 signal, in both charge and timing. These contributions come from statistical effects, such as photon counting, and electronic effects, such as digitization and reconstruction noise. f_{90} is given by the ratio:

$$f_{90} = \frac{\mu_p}{\mu_p + \mu_l} \tag{7.12}$$

where μ_p is the prompt signal, that is, the integrated light in the first 90 ns, and μ_l is integrated signal in the late region, such that:

$$\mu_{tot} = \mu_p + \mu_l \tag{7.13}$$

$$\mu_p = \mu_{tot}(f_{90}) \tag{7.14}$$

$$\mu_l = \mu_{tot}(1 - f_{90}) \tag{7.15}$$

where μ_{tot} is the total integrated pulse, S1. The variance of f_{90}, therefore, will be a function of the width of the prompt and late signals. For an ideal detector with perfect energy resolution, the sole source of variance is from Poisson counting statistics, ie: $\sigma_p^2 = \mu_p, \sigma_l^2 = \mu_l$. For a real detector, the variance can be modeled as:

$$\sigma_p^2 = \mu_p(1 + \sigma_{stat}^2) + \sigma_{elec,p}^2 \tag{7.16}$$

$$\sigma_l^2 = \mu_l(1 + \sigma_{stat}^2) + \sigma_{elec,l}^2 \tag{7.17}$$

Here σ_{stat}^2 includes all sources of noise which are proportional to μ, such as, for example, the PMT single photoelectron charge response (SPE). The $\sigma_{elec,l/p}^2$ terms account for variance introduced by both electronics and reconstruction effects.

7.2.1 Electronics Monte Carlo

In order to study the effect of statistical and reconstruction noise in both electron and nuclear recoils, a Monte Carlo simulation of these events was performed. The simulations were produced using the g4ds package (described in Section 3.3). For each type of interaction, 20,000 events were simulated with uniform distribution throughout the TPC active volume. The electron recoil events were simulated with energies between 1 and 50 keV, while the nuclear recoil events were simulated with energies between 20 and 200 keV (since nuclear recoils are quenched relative to electron recoils, these energy ranges yield values of S1 which are similar). The simulation models such things as the microphysics of LAr and photon propagation, including TPB effects. The final output contains a

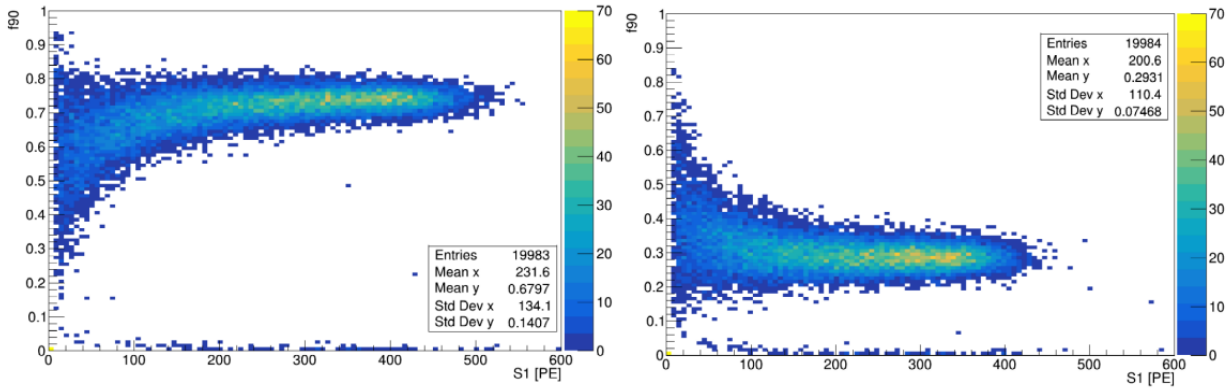

Figure 7.1: *Left:* Results of a nuclear recoil electronics Monte Carlo after reconstruction. The data in these plots includes the SPE width. *Right:* The same process was repeated for simulated electron recoils.

list of each photoelectron PMT hit, as well as the time of the hit relative to the event start time. This initial simulation output is processed by the electronics Monte Carlo package in darkart. First, each PE is assigned a charge. The charge may be sampled from a realistic exponential + Gaussian distribution with parameters input from SPE calibration data, or a delta function to remove all SPE variance, or another distribution of choice. For the purposes of this study, this step was performed twice: once with the delta function in order to study electronics and reconstruction effects alone, and once with the standard SPE spread in order to approximate the true total variance.

Once the charges have been assigned, each PE is given a time profile response, and a signal waveform is created. The waveform is overlayed on a real baseline, which has been smeared with a uniform distribution with a width of one ADC count in order to mimic an analog signal. Finally, the waveform is digitized, yielding a final product in an identical format to actual data.

The last step is to process the simulated waveforms in darkart. The reconstructed f_{90} vs S1 distributions are shown in Figure 7.1.

To analyze the effect of SPE width and reconstruction noise, the difference between the reconstructed $\mathrm{S1_{prompt}}$ and $\mathrm{S1_{late}}$ are compared to the true number of photoelectrons simulated in the prompt and late time windows. Figure 7.2 shows the distribution of these differences for electron recoils as a function of the total number of photoelectrons simulated, while Figure 7.3 shows the same for nuclear recoils. For an ideal detector which introduces no variance from the true number of photoelectrons, either from the PMT SPE charge width or during reconstruction, the difference between the simulated and reconstructed $\mathrm{S1_{prompt/late}}$ should be exactly zero. For a real detector, the difference between the true and reconstructed signal should be Gaussian distributed, with mean, $\mu = 0$, and variance, σ^2. The width of this distribution provides a measure of the integrated noise, while any deviation of the mean from zero measures bias (see Figure 7.4).

The prompt and late electronics noise is shown for both nuclear and electron recoils in Figures

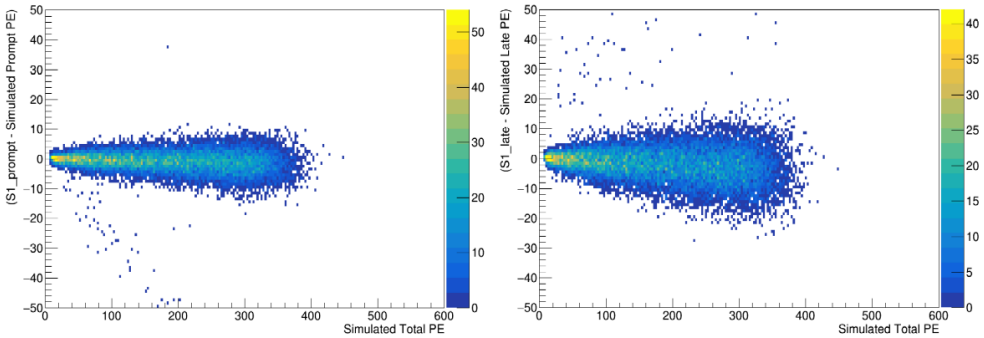

Figure 7.2: Simulated electron recoils, including the SPE charge width. Above is the difference in the reconstructed prompt (left) or late (right) signal and the true number of photoelectrons simulated in the respective time window, versus the total number of simulated PE.

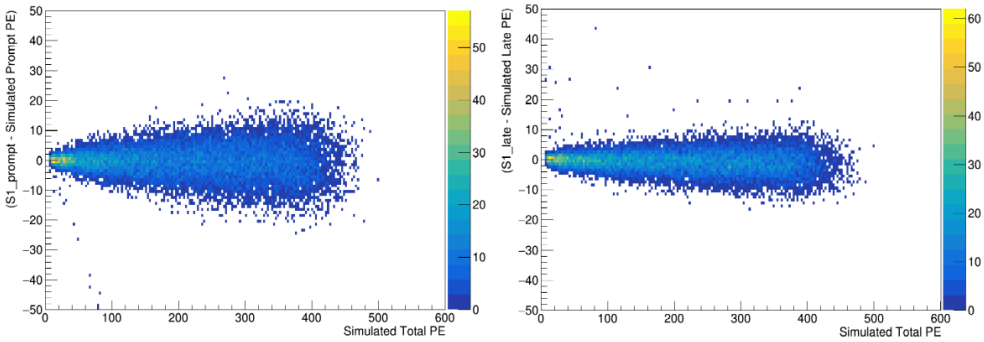

Figure 7.3: Simulated nuclear recoils, including the SPE charge width. Above is the difference in the reconstructed prompt (left) or late (right) signal and the true number of photoelectrons simulated in the respective time window, versus the total number of simulated PE.

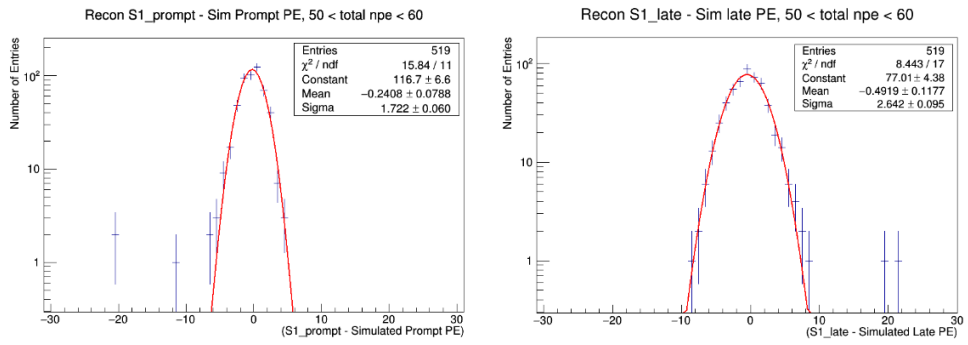

Figure 7.4: Distribution of difference in simulated prompt (left) or late (right) PE and the true number of simulated PE in the respective time window, for electron recoils with S1 energies between 50 and 60 PE. The distributions have been fit with a Gaussian. The variance of such Gaussian fits across all simulated energies is plotted in the following figures.

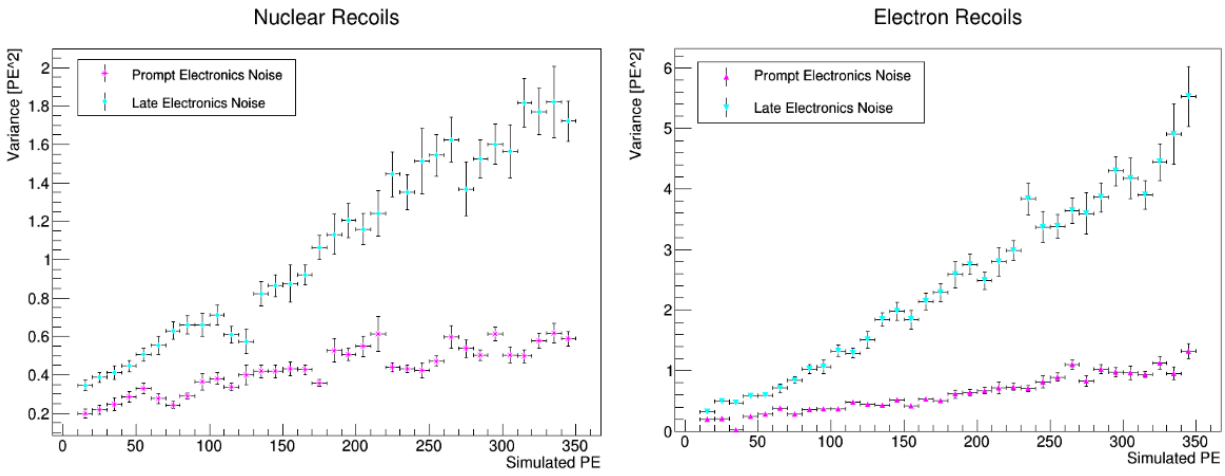

Figure 7.5: Variance of the difference between the reconstructed prompt / late S1 values and the true number of photoelectrons simulated in each time window, versus the total number of simulated photoelectrons. For both nuclear and electron recoils, the integrated electronics noise is larger in the late window than in the prompt.

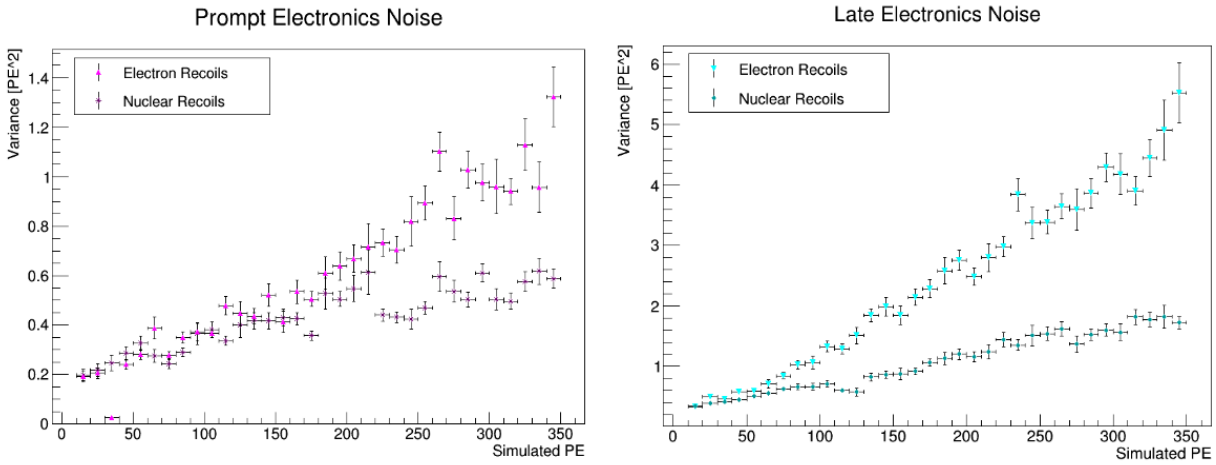

Figure 7.6: Comparison of the prompt (left) and late (right) electronics noise for nuclear and electron recoils.

7.5 and 7.6. As can be seen, for both types of interactions, the late integrated noise is larger than the prompt. However, the late noise for a given S1 value is larger for electron recoils than nuclear recoils. This can be explained by noting that the late time window is larger than the prompt, and electron recoils have tails which extend much longer in time. The prompt electronics noise is also different for the two classes of events. Given that the prompt time window is always the same length (90 ns) regardless of the magnitude of S1, we would expect the integrated prompt noise to be the same for electron and nuclear recoils. As can be seen in Figure 7.6, this is the case for S1 $< \sim$200 PE, after which the two distributions begin to diverge. Additionally, neither distribution

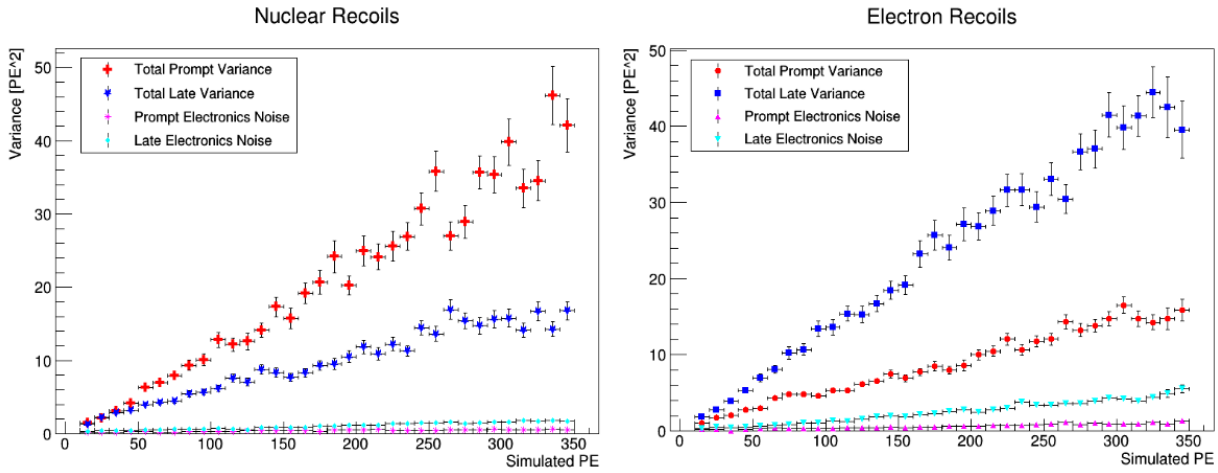

Figure 7.7: The total variance, including both the SPE width and electronics noise, is compared with the electronics noise alone in both the prompt and late time windows, for nuclear recoils (left) and electron recoils (right).

is truly flat, as one would expect if the noise integration was purely a function of integration time window and not also the magnitude of integrated charge. This finding is contrary to the method employed in the 70-day WIMP analysis, wherein the electronics noise terms were fixed to those determined for electron recoils, prior to fitting the nuclear recoil distributions. Future analyses will need to either perform a full characterization of variance for nuclear recoils in addition to electron recoils, or leave the noise terms as free parameters in the f_{90} fits.

The total (reconstruction + SPE) variance and electronics noise are shown for both nuclear and electron recoils in Figure 7.7. In both cases, the electronics noise is negligible compared to the SPE width. Note that the trend lines for total prompt and late variance are inverted for nuclear recoils relative to electron recoils. The reason for this inversion can be understood by observing that, from the data, we have a mean f_{90} value of 0.7 for nuclear recoils, and an electron recoil mean f_{90} of 0.3 (Figure 7.8). Thus, we make the approximation:

$$f_{90}^{NR} \approx 1 - f_{90}^{ER} \tag{7.18}$$

so that for a given S1,

$$\mu_p^{NR} \approx \mu_l^{ER}$$

In this approximation, equations 7.16 and 7.17 reduce to:

$$(\sigma_p^2 - \sigma_{elec,p}^2)^{NR} = (\sigma_l^2 - \sigma_{elec,l}^2)^{ER} \tag{7.19}$$

Neglecting electronics noise, we have:

$$(\sigma_p^2)^{NR} = (\sigma_l^2)^{ER} \tag{7.20}$$

This relation is demonstrated in Figure 7.9. After including the electronics noise terms (Eqn 7.19), most values agree within the uncertainty (Fig 7.10).

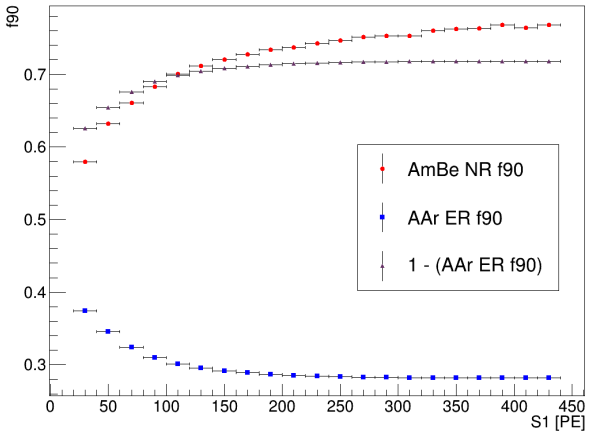

Figure 7.8: The mean f_{90} for nuclear recoils from AmBe calibration data is shown, along with the electron recoil f_{90} mean from AAr data. The third curve tests the approximation in Eqn 7.18.

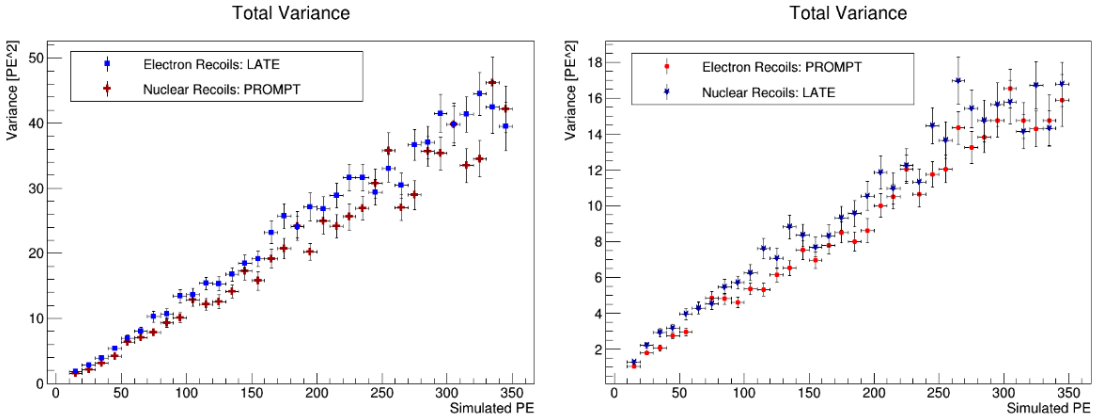

Figure 7.9: The prompt (late) variance in nuclear recoil events is approximately equal to the late (prompt) electron recoil variance, as predicted in Eqn 7.20.

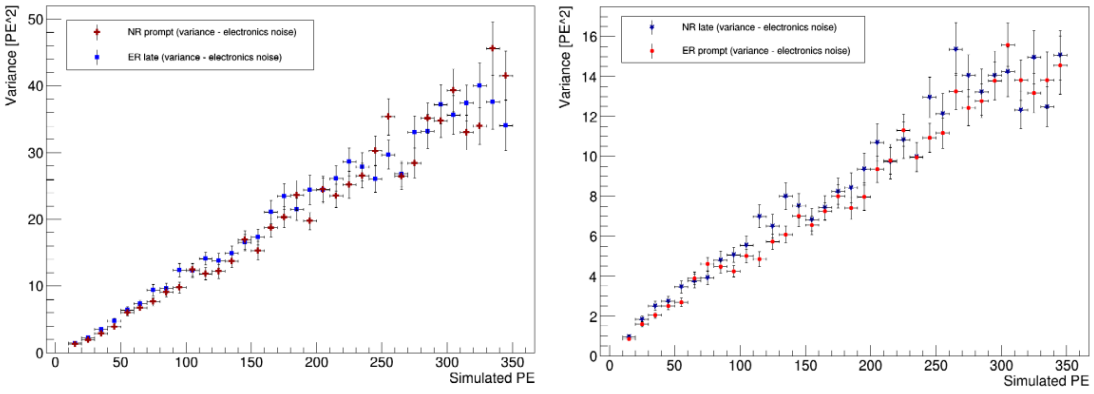

Figure 7.10: Subtracting the electronics noise, as in Eqn 7.19, improves the agreement between the two distributions.

7.3 Results of f_{90} Model Fits to the Nuclear Recoil Band

We can now proceed to comparing the results of fitting both models to the nuclear recoil band. While extensive studies have been performed examining model predictions and goodness-of-fit measures to the electron recoil band, there has been comparably little work doing the same for nuclear recoils. In general, electron recoil data has substantially more statistics available, making a close examination of behavior in the far tails of the distributions possible. This is especially true for single-sited interactions which form the basis of analytical models. Additionally, it is essential to have detailed knowledge of the limits of the background region in order to confidently identify or eliminate candidate WIMP events. Arguably of equal importance, however, is a clear understanding of the expected signal region, and both nuclear recoil acceptance and electron recoil leakage curves are required to establish a WIMP exclusion limit. While it is not strictly necessary to have the same model applied to electron and nuclear recoil events, any model which correctly describes the statistics of the pulse shape discrimination parameter is expected to work in both regimes.

For the purposes of this study, we use the higher statistics (160 n/s) AmBe data taken during the June, 2016 calibration campaign. After the majority of background electron recoil events have been removed by the optimized veto event selection (see Section 6.2), we have a nearly pure set of nuclear recoils. However, as can be seen in Figure 6.25, a residual electron recoil band remains. We begin our study by first simply removing the residual band, by requiring all events to be above the red curve shown in Figure 7.11, which is the 99% acceptance curve from the 70-day UAr analysis, shifted down in f_{90} by 0.05 and to the right in S1 by 10 PE. Note that this shift is essentially arbitrary, and is intended to avoid cutting into the tail of the nuclear recoil band. With only the nuclear recoil band remaining, albeit with some residual electron recoil contamination, we proceed to fit three f_{90} models to the data: the Hinkley model as applied in the 70-day UAr analysis, the 5 parameter Hinkley model, and the Covariance (or Tail) model. As described earlier, the Hinkley model as applied in all previous DarkSide analyses has only 2 free parameters, the f_{90} mean and the normalization; all other parameters are fixed to values determined by β/γ calibrations. The 5 parameter Hinkley model is the same basic model, but has 4 free parameters: the f_{90} mean, the normalization, and σ_p^2 and σ_l^2, the prompt and late variances. The Covariance model, likewise, has 4 free parameters: the f_{90} mean, the normalization, and k_P and k_L, the prompt and late standard deviation coefficients.

In order to perform the fits, the f_{90} distribution is sliced into 20 PE wide bins in S1, and the default fitting methods provided in the ROOT TH1 class are used. The results for a typical S1 bin of 60-80 PE are shown in Figure 7.12. As can be clearly seen, the original application of the Hinkley model is not a good fit to the nuclear recoil data. Because there are some bins in the tails of the f_{90} distributions which have less than 10 entries, for these bins, the assumption that the errors in each bin are normally distributed will not hold. Therefore, the value of the reduced χ^2 statistic cannot be relied upon as an absolute measure of the goodness of fit. Keeping this limitation in mind, and

noting that the assumption of normal errors is valid for most bins, we can nevertheless employ the reduced χ^2 to make an approximate comparison of the fit results of each model, shown in Figure 7.13. The original Hinkley application shows systematically worse values across all energy bins. Given this result, and its consistency with earlier findings, the original application of the Hinkley model is not considered further for nuclear recoils. Any further reference to the Hinkley model is to the 5 parameter application.

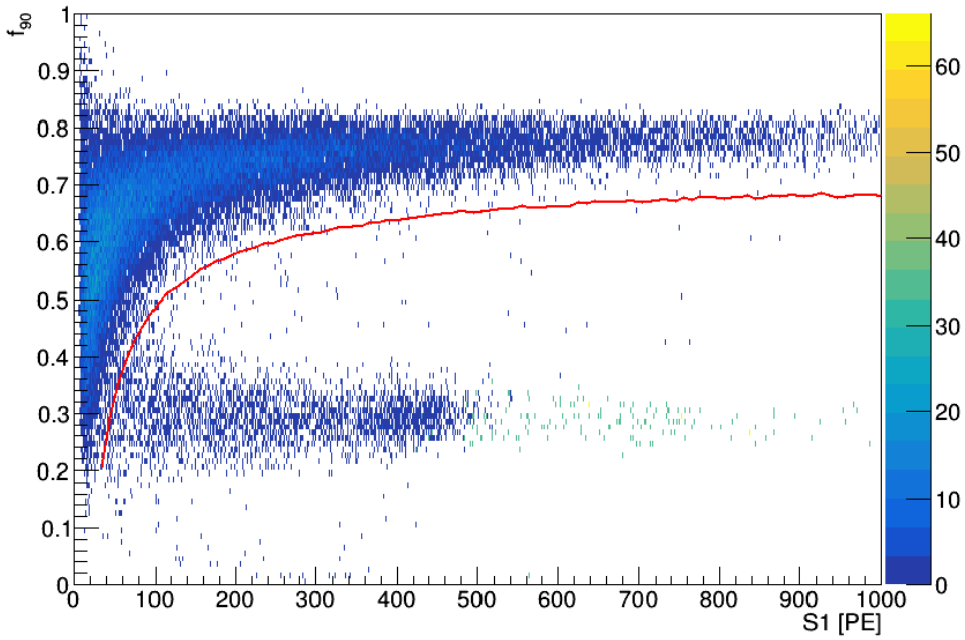

Figure 7.11: AmBe data, after veto event selection, along with the curve used to remove the residual electron recoil band. The red curve is the 99% acceptance curve from the 70-day UAr analysis, which has been shifted by +10 PE in S1 and -0.05 in f_{90}. The shift is arbitrary and is meant to avoid removing tail nuclear recoil events.

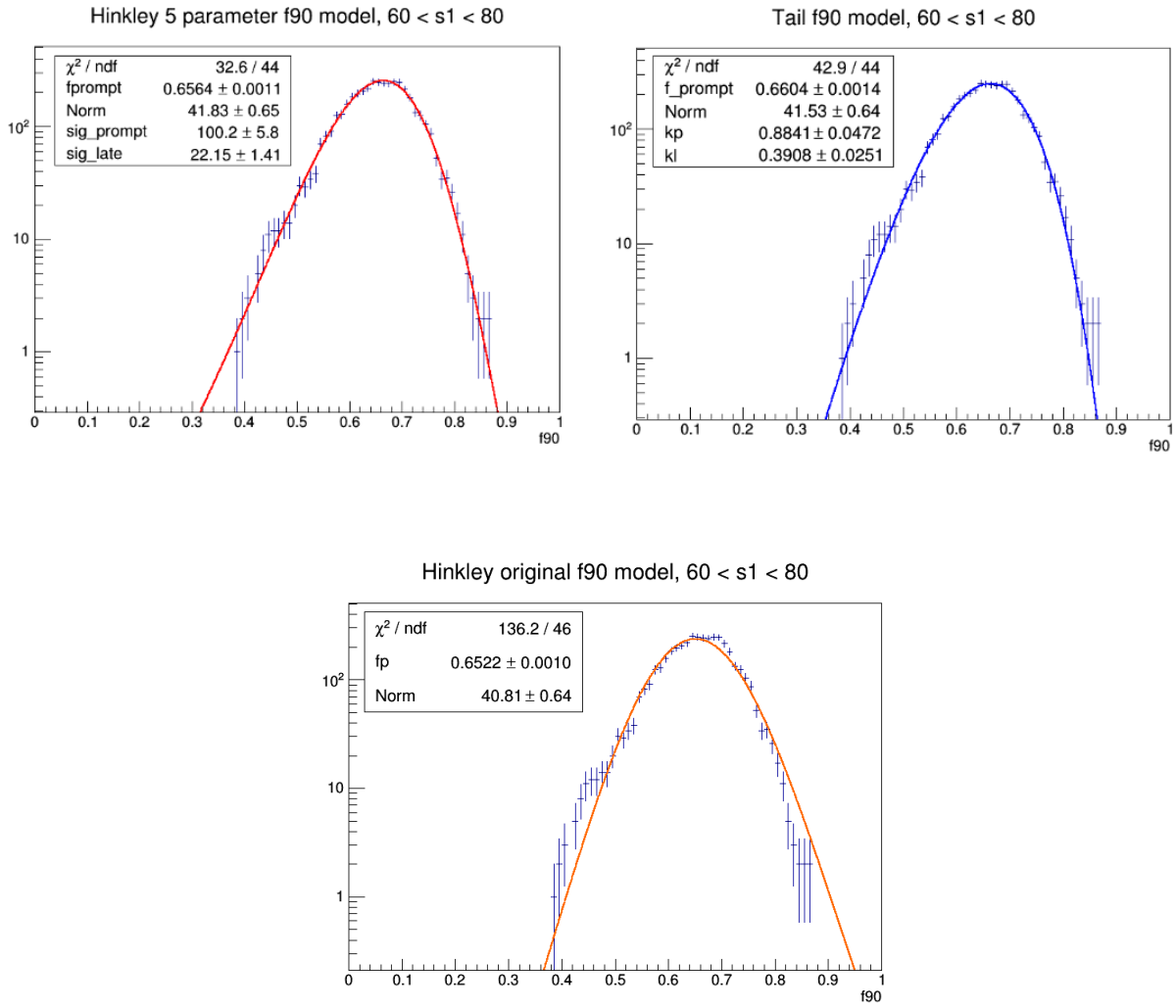

Figure 7.12: Model fits for a typical S1 bin of 60-80 PE. The orginal application of the Hinkley model (bottom) is not a good fit to the data, relative to both the Hinkley model with free noise parameters and the Covariance model.

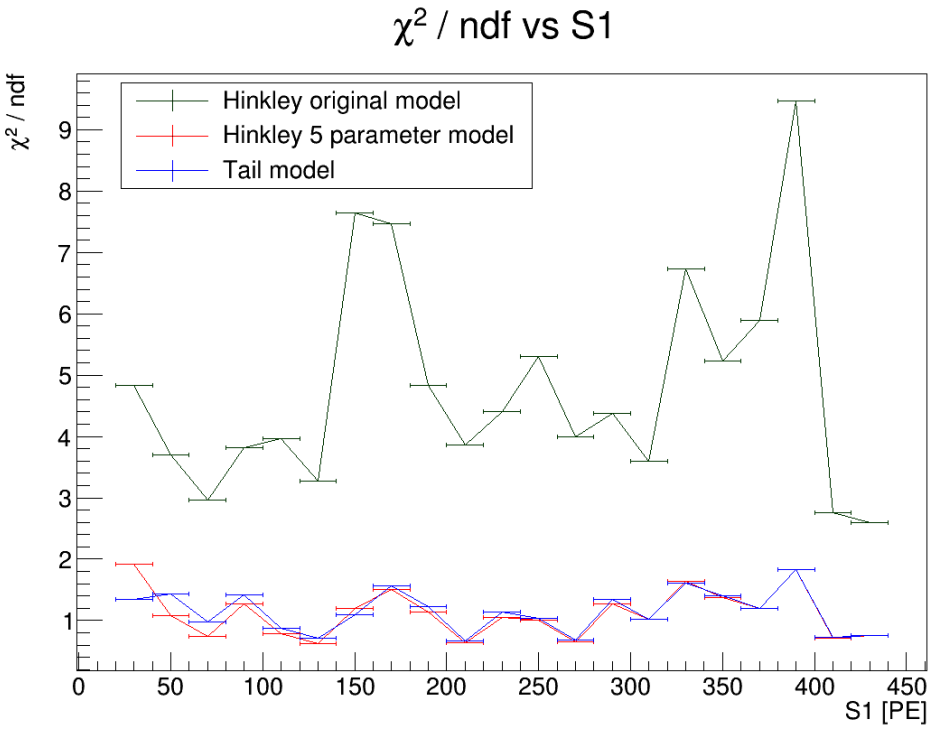

Figure 7.13: Reduced χ^2 values for both applications of the Hinkley model and the Covariance model. The poor results from the original Hinkley application to nuclear recoils is demonstrated by the systematically higher values across all energy bins fitted.

While removing the residual electron recoil band allows for a simple fitting process, it ignores the fact that electron recoil events will still remain in the low S1 region, and possibly bias the fits there. The solution, therefore, is to fit both bands simultaneously with a summed model, either the sum of two Covariance models or the sum of two Hinkleys.

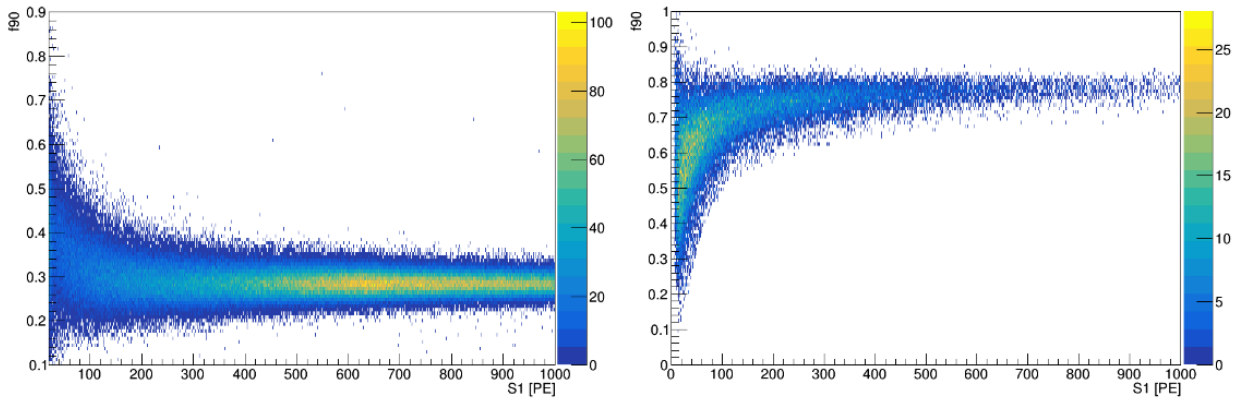

Figure 7.14: *Left:* UAr data is first fit to extract the electron recoil parameter values. *Right:* AmBe data, after veto event selection. The residual electron recoil band has been removed by excluding all event below the 99% acceptance curve from the 70-day UAr analysis, which has been shifted by +10 PE in S1 and -0.05 in f_{90}. This data is then used for a model fit to extract initial nuclear recoil parameter values. The final summed model is fit to the data shown in Figure 6.25, right.

In order to properly initialize the parameter values, the model under consideration is first fit to the electron recoil band. The data chosen for this fit is the UAr 70-day data, which established the first WIMP exclusion limit with low radioactivity argon [39] (Figure 7.14, left). Next, the model is fit to the June, 2016 AmBe data, after veto event selection and with the residual electron recoil band cut away (Figure 7.14, right). Finally, the summed model is fit to both bands, using the parameter values found in the previous two fits. Because of the very low statistics in the residual electron recoil band, the electron recoil f_{90} mean, prompt and late noise terms are fixed to the values from the UAr fit, leaving only the electron recoil normalization term free. For the nuclear recoil band, all the parameters are initialized to the values found in the first AmBe fit, although none are fixed, save the mean S1 value.

The minimization is performed using the Minuit2 package in ROOT. The distribution shown in Figure 6.25, right, was sliced into 20 PE wide bins in S1, and each resulting f_{90} histogram fit with the summed model. In order to control all aspects of the fit, the ROOT::Fit classes are employed, rather than the default fitting methods in the TH1 histogram class. Although there are some bins with low statistics in the tails of the f_{90} distributions, for both models a likelihood fit did not converge for all energy bins. For this reason, a χ^2 fit is performed. The results of all the fits can be see in Appendix A.

Figure 7.15 shows the fitted models in the lowest energy bins, for S1 values between 20 and

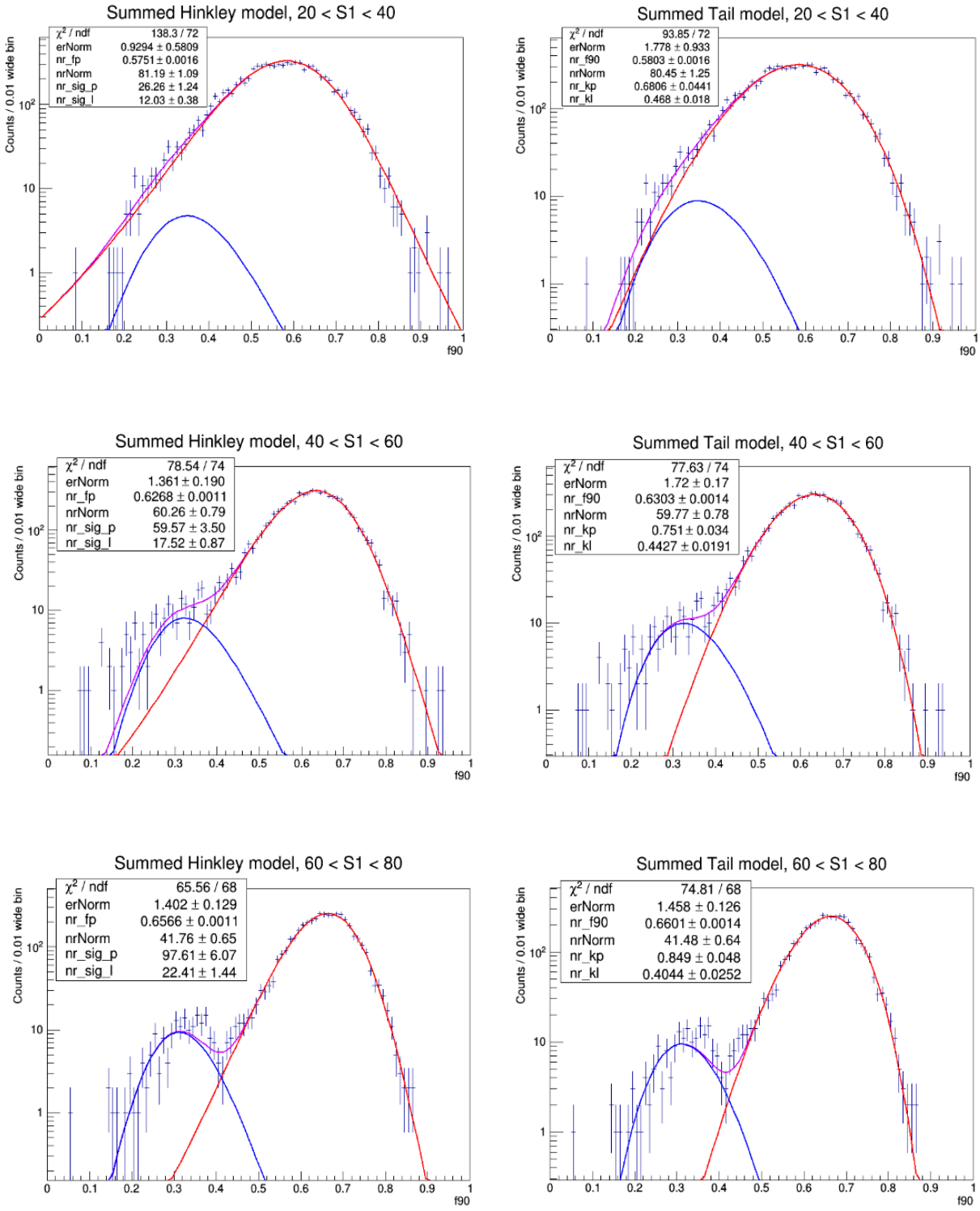

Figure 7.15: Results of the summed model fits for the first three energy bins.

80 PE. The summed model fit is the purple curve shown, along with the component nuclear and electron recoil band fits in red and blue, respectively. As was described in Section 7.1.1, the Hinkley model overestimates the tails at low energies. For S1 values greater than approximately 120 PE, the predictions of both models converge and are effectively identical.

This convergence is also seen in goodness-of-fit measures. As was stated above, given the presence of bins with low statistics, the value of the reduced χ^2 is not reliable as an absolute measure of fit performance. We choose, instead, to use the unbinned Kolmogorov-Smirnov test [56]. This test evaluates the likelihood that two data sets were drawn from the same parent distribution by comparing the cumulative distribution functions for each. Randomly sampled data for which this is true can be expected to have p-values distributed between 0 and 1. Very low p-values are associated with non-compatible distributions. This test has the advantage of being unaffected by binning effects or low statistics in the tails, and does not depend on the underlying distribution.

To compare the models to the data, for each bin in S1, we randomly generate events from the model, for the same number of events as are available in the data. This model-generated data set is then compared to the actual data, and a p-value is calculated. For individual comparisons, the randomly generated model data naturally varies, and the p-values range between 0 and 1, as expected. In order to obtain a stable evaluation of the model's performance, this process is repeated N times, and the average p-value for a given bin is used as the final test statistic. Results were evaluated for N = 10, 100, 1000 and 10,000 trials, with convergence occurring by 100 trials and virtually no variation in the results thereafter. The results are shown in Figure 7.16.

In the lowest energy bin, for S1 fixed to 30 PE, the Covariance (Tail) model performs significantly better than the Hinkley model. At this energy, the Hinkley model overestimates the abundance of nuclear recoils relative to electron recoils. This is reflected in the fitted electron recoil normalization constant, which is lower in the first energy bin than the second, suggesting that there are more electron recoils for S1 values between 40 and 60 PE than there are between 20 and 40 PE. This is contrary both to intuition and what is seen in data, as well as what is predicted by the Covariance model. However, for S1 values greater than $\sim$60 PE, the model performances are indistinguishable.

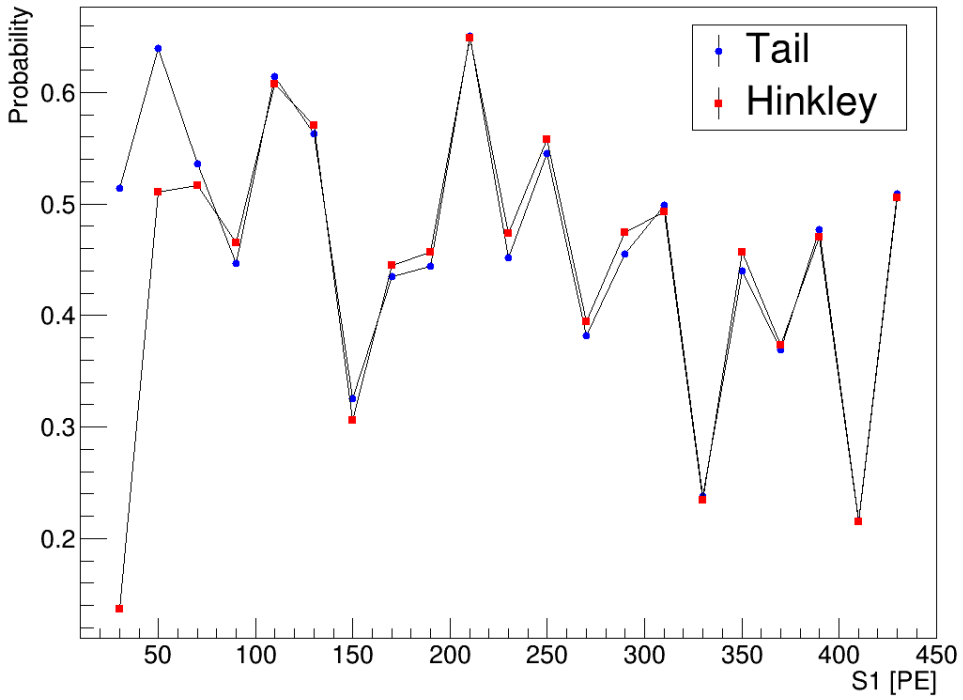

Figure 7.16: Comparison of probability values from a Kolmogorov-Smirnov test for fits of the summed Covariance (Tail) and summed Hinkley models.

Fitted Noise Parameters

When comparing the prompt and late noise terms predicted by each model (shown in Figure 7.17), recall that for the Hinkley model as applied to nuclear recoils, the fit parameters are σ_p^2 and σ_l^2, the total prompt and late variance, whereas from the Covariance model we extract k_p and k_l, the coefficients on the prompt and late standard deviations. Thus, to make a direct comparison, in Figure 7.18 we plot the total variance from each model, which for the Covariance model is given by Eqns. 7.10 and 7.11. As can be seen, the values are in overall agreement. However, the Hinkley model predicts both a larger late noise component and smaller prompt than expected from the Covariance model. This difference is more significant for the late variance, as the prompt values, while systematically smaller in the Hinkley model, are consistent within the uncertainty.

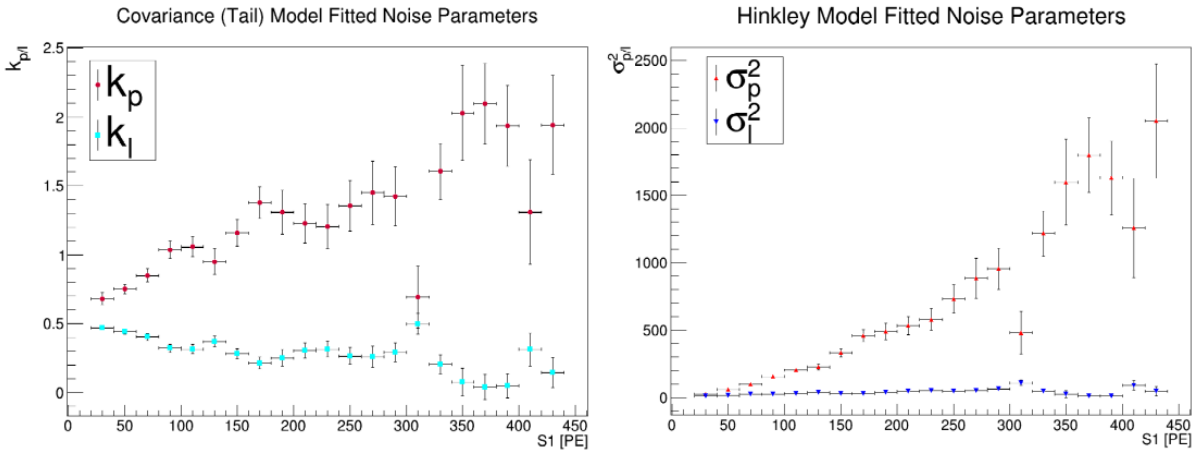

Figure 7.17: Fitted noise parameters from the Covariance model (left) and Hinkley model (right). Recall that $k_{p/l}$ in the Covariance model are the coefficients on the prompt and late standard deviations, whereas the fitted parameters in the Hinkley model are the total prompt and late variances, $\sigma^2_{p/l}$.

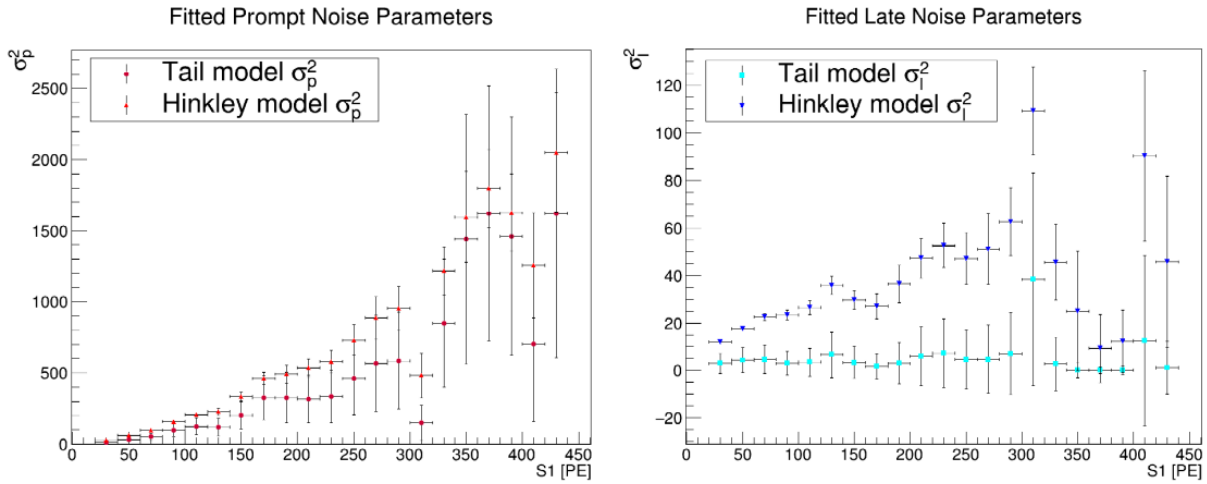

Figure 7.18: *Left:* The prompt variance from each model. Although the Covariance model values are higher than those of the Hinkley model, all agree within the uncertainty. *Right:* The late variance from each model. The late variance predicted by the Hinkley model is systematically higher than that from the Covariance model.

7.3.1 Estimation of Fraction of Electron Recoil Events in the Nuclear Recoil Band from f_{90} Models

Based on the area of overlap between the fitted electron and nuclear recoil bands (blue and red curves in Figure 7.15), we can obtain an estimate of the fraction of contaminating electron recoil events. This value can then be compared with the results from Section 6.3.2. For each energy bin up to a median S1 value of 110 PE, after which the bands no longer overlap, we calculate the ratio of the shaded area in Figure 7.19, left, to the total area under nuclear recoil curve. In the case of the Covariance model, the maximum contamination is estimated to be ∼2.2% in the lowest energy bin corresponding to a median S1 value of 30 PE. The poor performance of the Hinkley model in the same bin, however, is reflected in an unrealistically low estimation of the electron recoil curve area there. For S1 values greater than 40 PE, both models give consistent results.

The value of less than 2.5% is much less than the 16% value for the ER/NR ratio found in Section 6.3.2. However, the event selection criteria applied in the Monte Carlo were significantly more lax than those applied in the data (δt prompt < 0 in the MC, compared to -50 $< \delta$t prompt $<$ -40 ns in data). We can make a more direct comparison by relaxing the minimum δt prompt event criteria in the data and evaluating the effect on the ER/NR ratio, as was done in Figure 6.24. When we allow veto clusters up to 4 μs before the TPC prompt (the full pre-prompt window, as was done in the Monte Carlo), we obtain an ER/NR ratio of ∼15%. Based on the small fraction of mixed events found in the Monte Carlo of less than 1%, we conclude that the incidence of mixed (nuclear plus electron recoils in a single pulse) events in data after event selection is vanishingly small.

The low level of residual electron recoil events is also supported by comparing the nuclear recoil acceptance predicted by a single model fit after simply cutting away the electron recoil band, as was done above, to that predicted by the summed model fits. The difference is only seen in the very tails of the distributions, at greater than 95% acceptance, and only in the two lowest energy bins (see Figure 7.20).

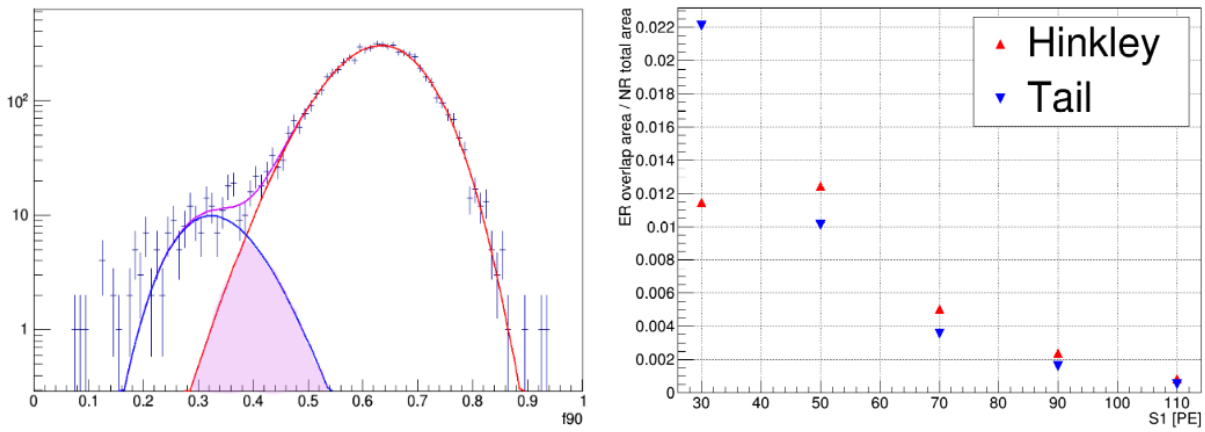

Figure 7.19: Area of overlap between electron and nuclear recoil bands as predicted by each f_{90} model provides an estimate of the fraction of electron recoil contamination in the nulcear recoil band. The unrealistically low estimation by the Hinkley model of the fraction of electron recoil events in the lowest energy bin is a reflection of the poor fit there.

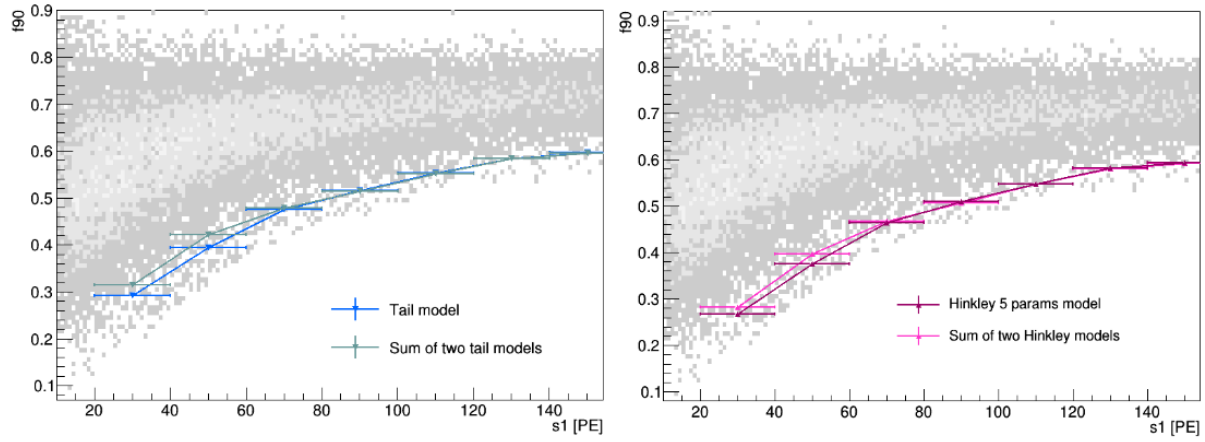

Figure 7.20: 99% acceptance curves, as predicted by a single model fit to the nuclear recoil band, and a summed model fit which includes the residual electron recoil band. The evidence for a bias introduced by ignoring the residual electron recoils is seen in the lowest two energy bins.

7.4 Nuclear Recoil Acceptance

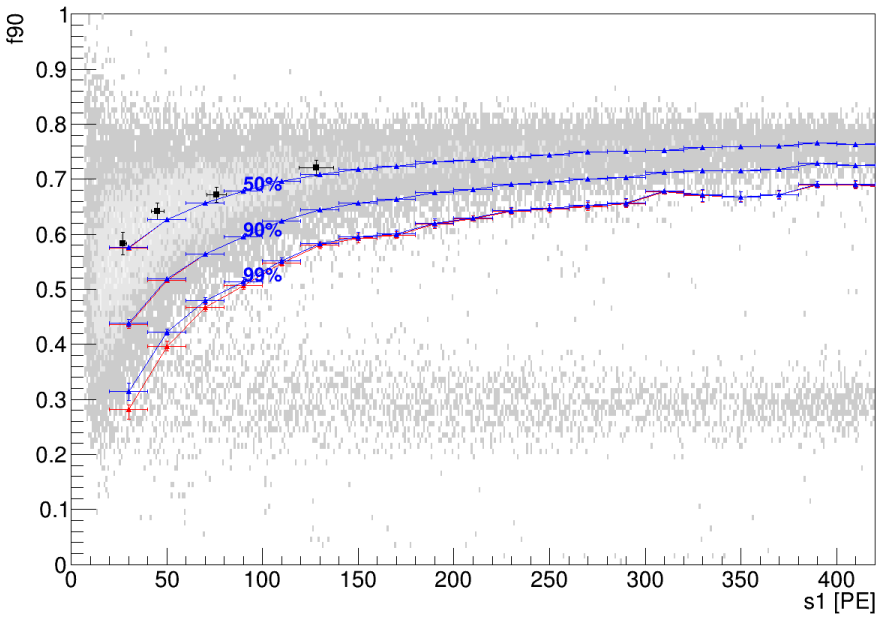

Figure 7.21: Nuclear recoil acceptance curves from both the Hinkley and Covariance models, along with the median f_{90} values extrapolated from ScENE to DarkSide-50.

To determine the nuclear recoil acceptance, we calculate the quantiles predicted by each model. As expected from the fit results, the model predictions are only different in the low energy tail of the f_{90} distributions, for acceptance values greater than 90%.

The uncertainty in the acceptance values is estimated via bootstrap resampling [56] [57]. We assume, first, that the sample of AmBe data after event selection is representative of the true nuclear recoil f_{90} distribution. We can then generate an empirical distribution of parameters which describe f_{90}, such as the median, by randomly sampling (with replacement) from the data. For a given range of S1 with n events, we generate $N = 10{,}000$ bootstrap samples of the f_{90} distribution, each containing n events drawn with replacement. To each bootstrap sample, we fit the respective model and extract the parameters.

The parameter bias, or systematic deviation from its true value, is given by:

$$\textbf{Bias}(\hat{\theta}) = \mathbf{E}[\hat{\theta} - \theta] = \mathbf{E}[\theta] - \theta \tag{7.21}$$

Here $\hat{\theta}$ is the parameter estimation from the model and θ is the (unknown) true parameter value. The parameter variance is likewise given by;

$$\textbf{Variance}(\hat{\theta}) = \mathbf{E}\Big[(\hat{\theta} - \mathbf{E}[\hat{\theta}])^2\Big] \tag{7.22}$$

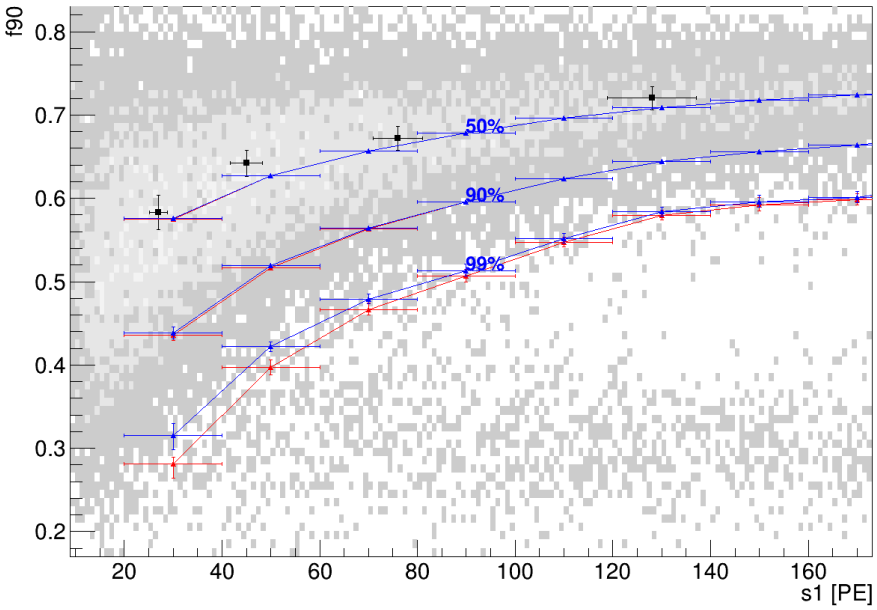

Figure 7.22: A zoomed in view of the low energy region from Figure 7.21, where the difference between the model predictions becomes apparent.

Since the true values are unknown, we approximate the bias and variance using the bootstrap parameter distribution, $\hat{\theta}^*$:

$$\textbf{Bias}(\hat{\theta}) \approx \frac{1}{N}\sum_i \hat{\theta}_i^* - \hat{\theta} \tag{7.23}$$

$$\textbf{Variance}(\hat{\theta}) \approx \frac{1}{N-1}\sum_i (\hat{\theta}_i^* - \hat{\theta})^2 \tag{7.24}$$

A full listing of the acceptance values shown and their estimated bias and variance can be found in Appendix B.

The acceptance curves are shown in Figures 7.21 and 7.22, along with the median f_{90} values as extrapolated from the ScENE data to DarkSide-50, for comparison. As can be seen, all values agree with the ScENE data within the uncertainty. Because the ScENE data is robust against the inclusion of inelastic scatters, this agreement suggests that such events do not constitute enough of a contribution to bias the DarkSide-50 results. Additionally, this result demonstrates the ability to define the nuclear recoil acceptance region in DarkSide-50 exclusively from *in-situ* measurements, without reliance on an external measurement such as that provided by the ScENE experiment.

CHAPTER 8
NEXT STEPS: THE FUTURE OF DARKSIDE

Currently, data is being accumulated for a blind analysis, the results of which will be published later this year. This analysis will benefit from the improved nuclear recoil calibration data now available, as well as improved understanding of the intrinsic backgrounds and detector response. DarkSide-50 is planning to obtain a total of 3 live years of WIMP search data, allowing it to achieve an additional order of magnitude sensitivity.

8.0.1 DarkSide-20k

Building on the success of DarkSide-50, the next stage in the program is DarkSide-20k. DarkSide-20k will be a 30 tonne (20 tonne fiducial) liquid argon TPC, encased in a nested active veto design modeled after that used in DarkSide-50. The detectors will be assembled and installed beginning in 2019, with data taking scheduled to begin at the end of 2020. All components are being designed for ultra-low backgrounds, including the development of silicon photomultipliers (SiPMs), which will replace traditional PMTs in the TPC. Rather than stainless steel, the TPC will be constructed of high-purity titanium, and filled with depleted argon (DAr). Although the level of ^{39}Ar in UAr has been substantially reduced relative to AAr, it will still produce 1.8 x 10^8 β decays in the exposure planned for DarkSide-20k. In order to obtain the quantity of UAr required, and further purify it to the degree necessary, dedicated operations have been initiated, and are described below.

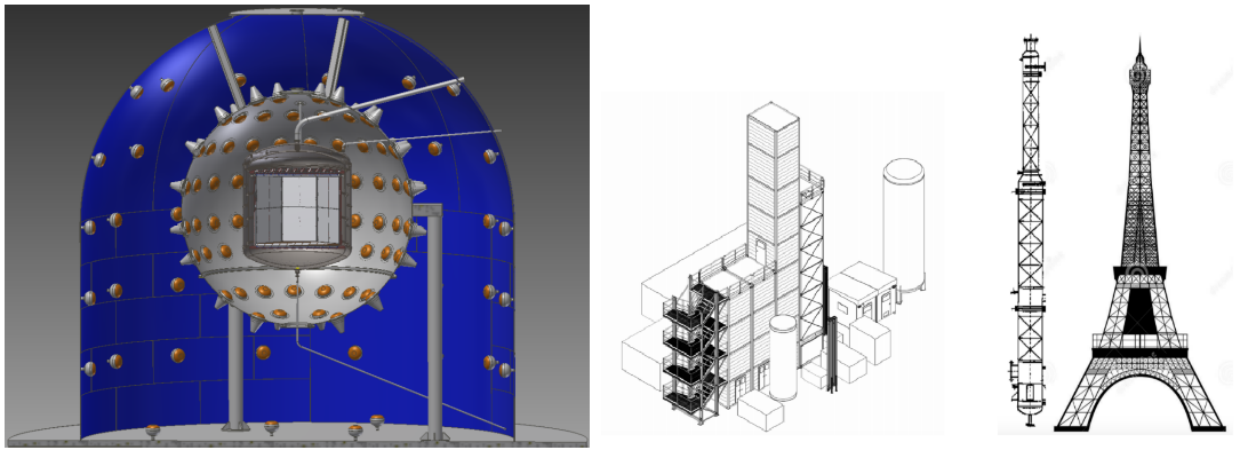

Figure 8.1: *Left:* Cross section of DarkSide-20k. In the center is the titanium cyrostat, surrounded by an LSV and WCV, with similar designs to those in DarkSide-50. *Right:* Conceptual drawings of the Urania plant (left) and Aria (right). The Aria column is shown next to the Eiffel Tower, for scale.

8.0.2 Urania and Aria

Given that the 155 kg of UAr currently in use in DarkSide-50 required 6 years to procure, the first step in acquiring the 30 tonnes of DAr necessary for DarkSide-20k is to increase the rate of production. This will be achieved by the expansion of the Kinder Morgan Doe Canyon Facility located in Cortez, CO. This expansion is made possible in part because of the industrial value of the gases being extracted. After the DarkSide collaboration provided the Kinder Morgan corporation an analysis of the components of the gas stream used to produce UAr, which identified the presence of helium, a partnership was formed between Kinder Morgan and Air Products, allowing Air Products to extract the helium. Of the gas returned to Kinder Morgan by Air Products, 6% is then purified in the Urania plant for DarkSide. In addition to being commercially profitable, this agreement has the added benefit of removing the helium as well as any traces of water vapor from the UAr. When operating at design capacity, Urania will produce ∼100 kg of UAr a day.

From there, the UAr will be shipped to the Aria project, located in Sardinia, Italy. Aria is two, 350 m tall cryogenic distillation columns constructed in underground shafts which are a part of the Seruci mine. Construction of the first column began in September, 2015. Each pass of the UAr through the columns is expected to yield a factor of 10 reduction in residual ^{39}Ar. Other impurities, such as O_2 and Kr, will be reduced by a factor of 10^3 per pass.

With a planned exposure of 100 tonne-year, DarkSide-20k will obtain a sensitivity of 10^{-47} cm^2 for a WIMP mass of 100 GeV/c^2. The final story in the DarkSide saga will be told by Argo, a planned 200 tonne DAr TPC, which will reach the level of 10^{-48} cm^2 sensitivity, beyond which is the limit imposed by coherent neutrino-nucleus scattering.

8.1 Conclusions

This work presents the system for insertion of radioactive sources into the DarkSide-50 LSV, CALIS, from its design and testing, to installation and commissioning. CALIS has been successfully operated multiple times for the calibration of both the TPC and the LSV, producing data vital to the experiment. Among these results, the nuclear recoil acceptance curves extrapolated from ScENE were verified, contributing to the establishment of the best WIMP exclusion limit on an argon target to date.

In this work, the response of the DarkSide-50 TPC pulse shape to nuclear recoils has been thoroughly characterized, including the variance with respect to the true number of photoelectrons, and a distinction between that for electron recoils identified. Furthermore, a new analysis method for neutron calibration with radioactive sources, which removes the obscuring electron recoil background, has been developed. A high statistics data set of nuclear recoils from AmBe was obtained, and used to produce nuclear recoil acceptance curves, independent of ScENE results. The definition of the DarkSide-50 signal region will aid in the establishment of the next WIMP exclusion limit,

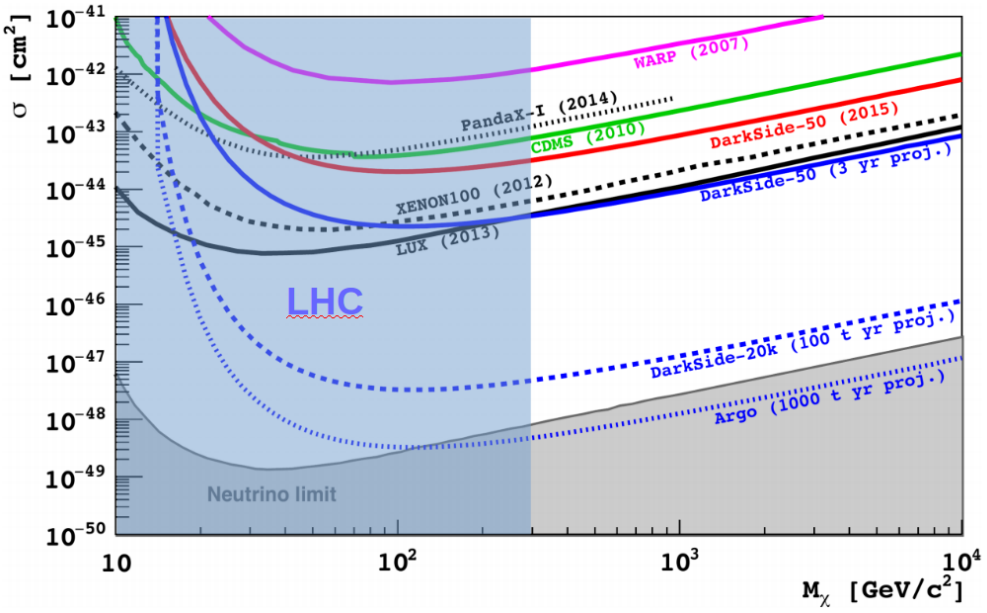

Figure 8.2: Projected sensitivities of DarkSide-50 (following the conclusion of 3 years running), DarkSide-20k and Argo.

or identification of a WIMP signal, should one be discovered.

APPENDIX A
F_{90} MODEL FITS

A.1 Hinkley Model Fits

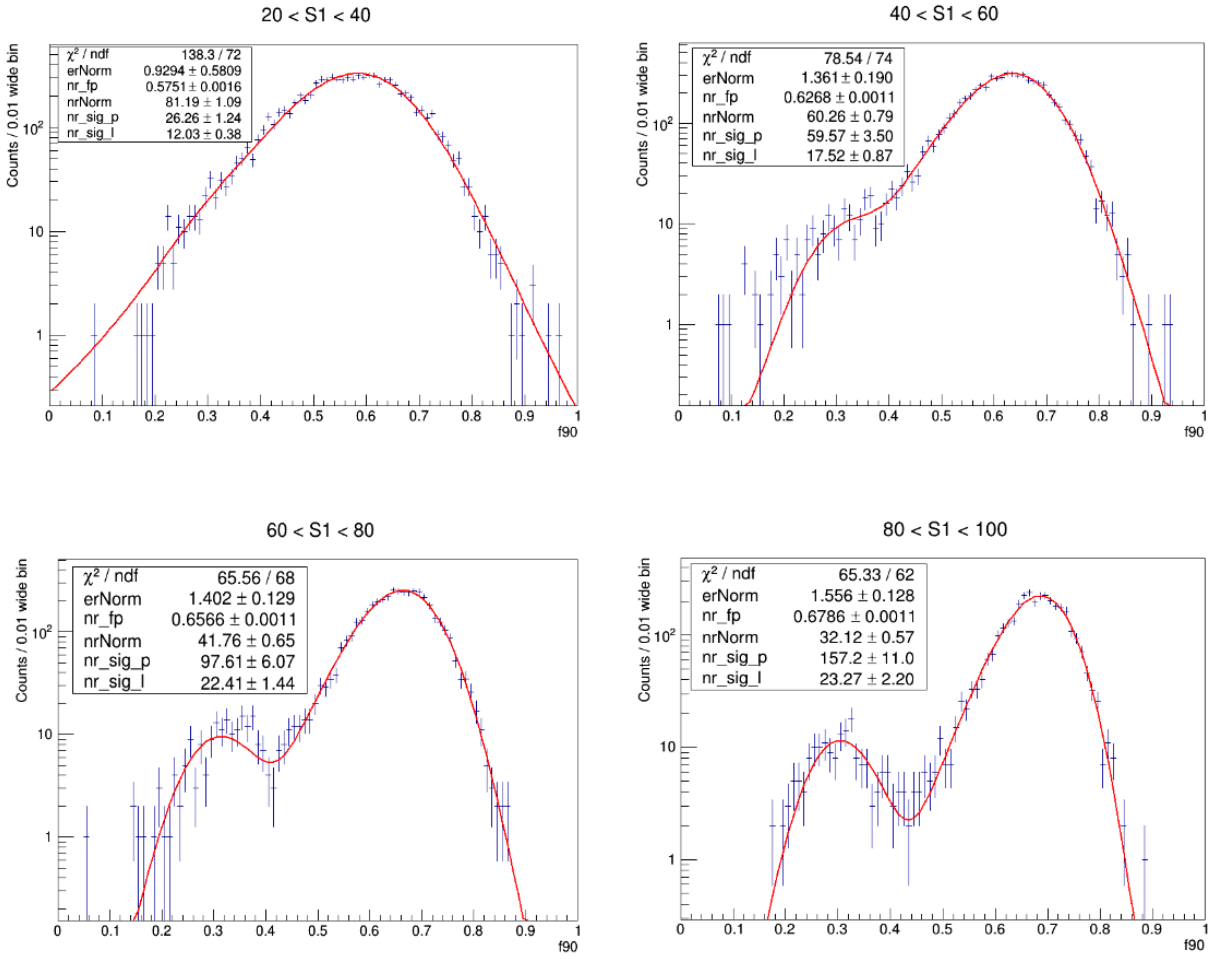

100 < S1 < 120

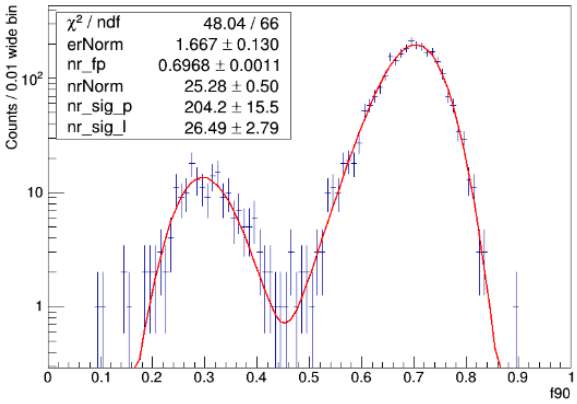

120 < S1 < 140

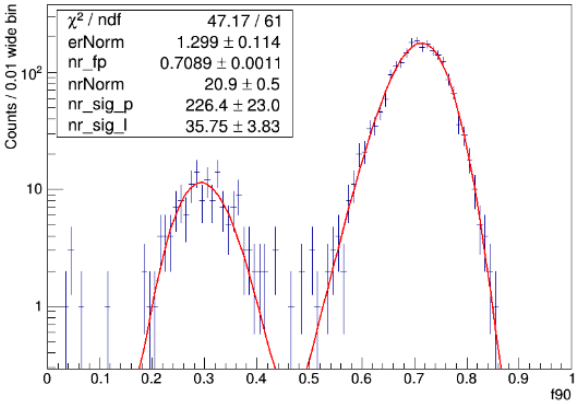

140 < S1 < 160

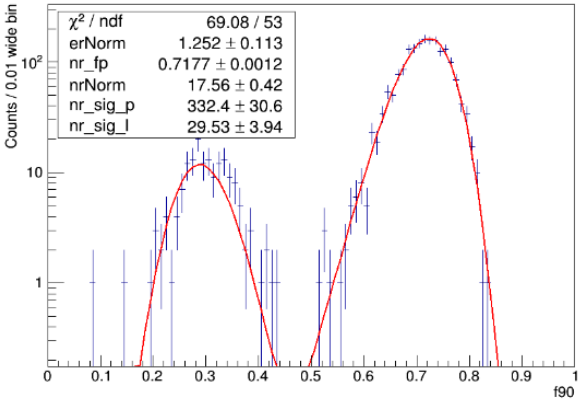

160 < S1 < 180

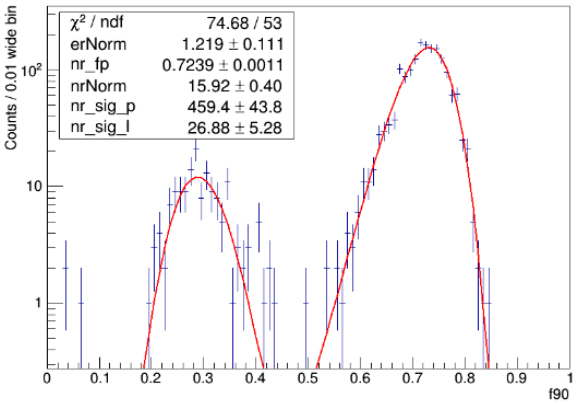

180 < S1 < 200

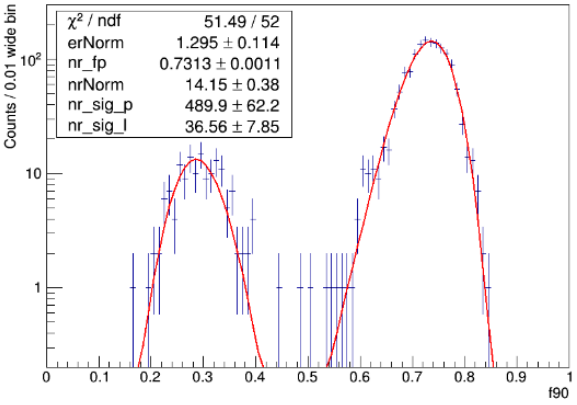

200 < S1 < 220

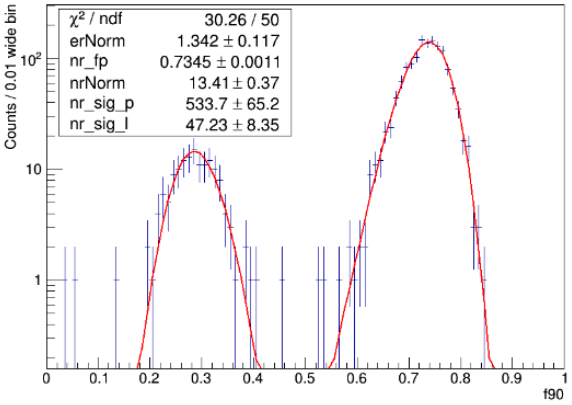

220 < S1 < 240

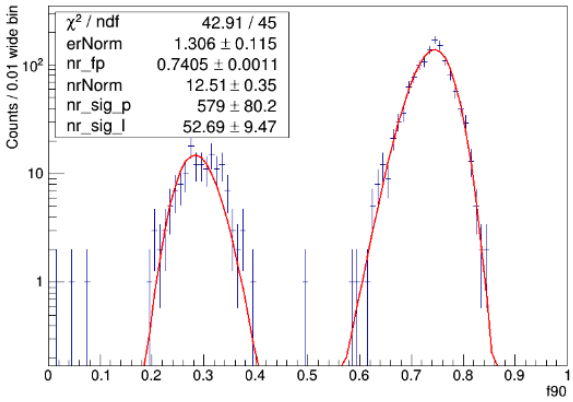

240 < S1 < 260

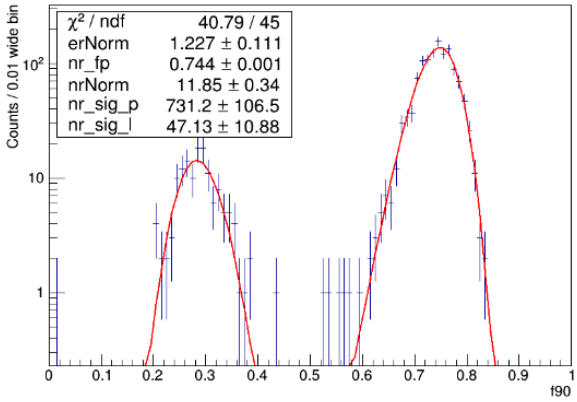

260 < S1 < 280

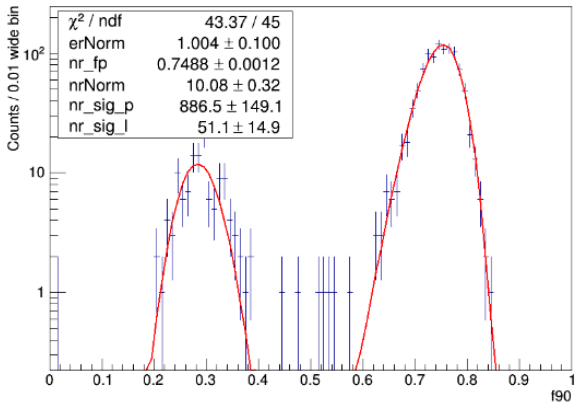

280 < S1 < 300

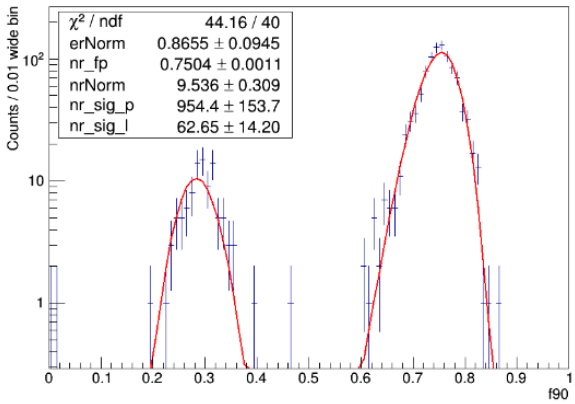

300 < S1 < 320

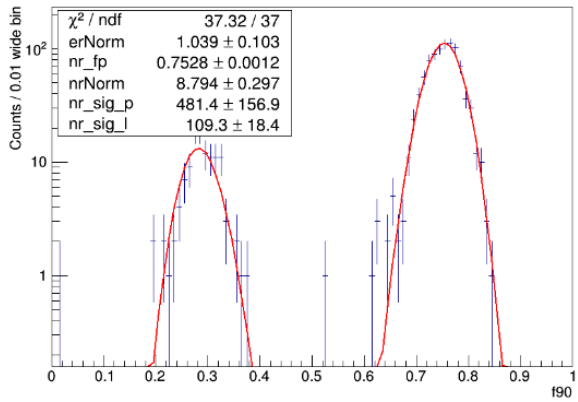

320 < S1 < 340

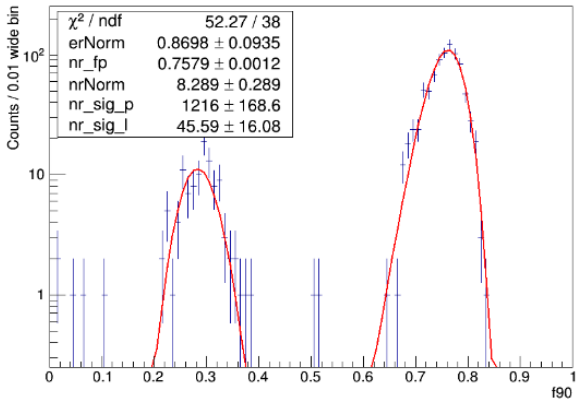

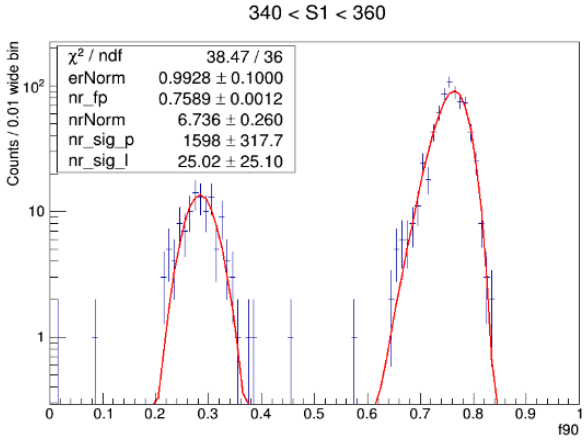
340 < S1 < 360
χ² / ndf 38.47 / 36
erNorm 0.9928 ± 0.1000
nr_fp 0.7589 ± 0.0012
nrNorm 6.736 ± 0.260
nr_sig_p 1598 ± 317.7
nr_sig_l 25.02 ± 25.10
Counts / 0.01 wide bin
f90

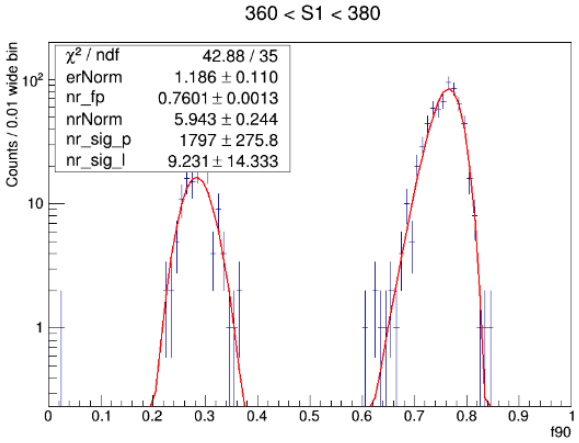
360 < S1 < 380
χ² / ndf 42.88 / 35
erNorm 1.186 ± 0.110
nr_fp 0.7601 ± 0.0013
nrNorm 5.943 ± 0.244
nr_sig_p 1797 ± 275.8
nr_sig_l 9.231 ± 14.333
Counts / 0.01 wide bin
f90

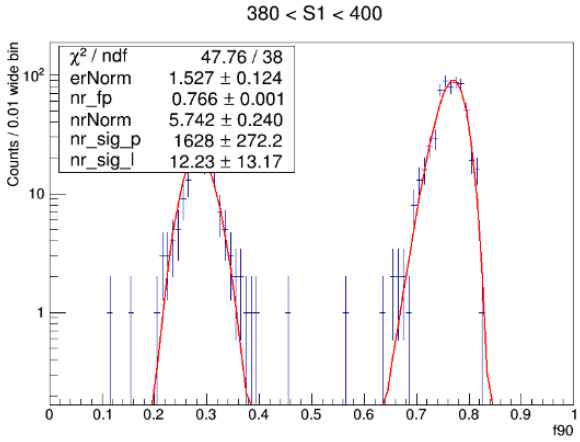
380 < S1 < 400
χ² / ndf 47.76 / 38
erNorm 1.527 ± 0.124
nr_fp 0.766 ± 0.001
nrNorm 5.742 ± 0.240
nr_sig_p 1628 ± 272.2
nr_sig_l 12.23 ± 13.17
Counts / 0.01 wide bin
f90

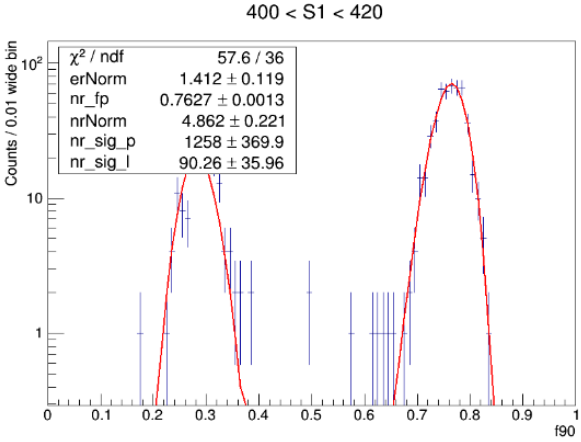
400 < S1 < 420
χ² / ndf 57.6 / 36
erNorm 1.412 ± 0.119
nr_fp 0.7627 ± 0.0013
nrNorm 4.862 ± 0.221
nr_sig_p 1258 ± 369.9
nr_sig_l 90.26 ± 35.96
Counts / 0.01 wide bin
f90

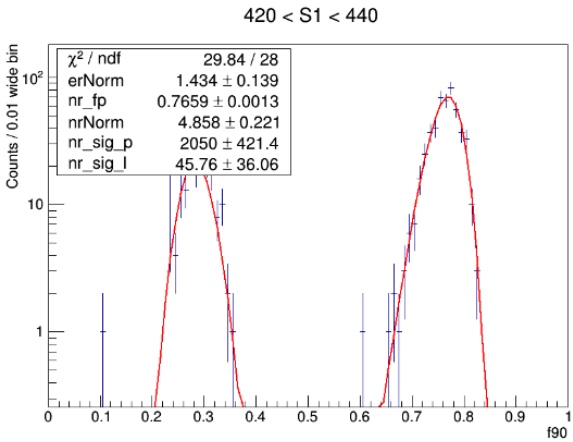
420 < S1 < 440
χ² / ndf 29.84 / 28
erNorm 1.434 ± 0.139
nr_fp 0.7659 ± 0.0013
nrNorm 4.858 ± 0.221
nr_sig_p 2050 ± 421.4
nr_sig_l 45.76 ± 36.06
Counts / 0.01 wide bin
f90

A.2 Covariance Model Fits

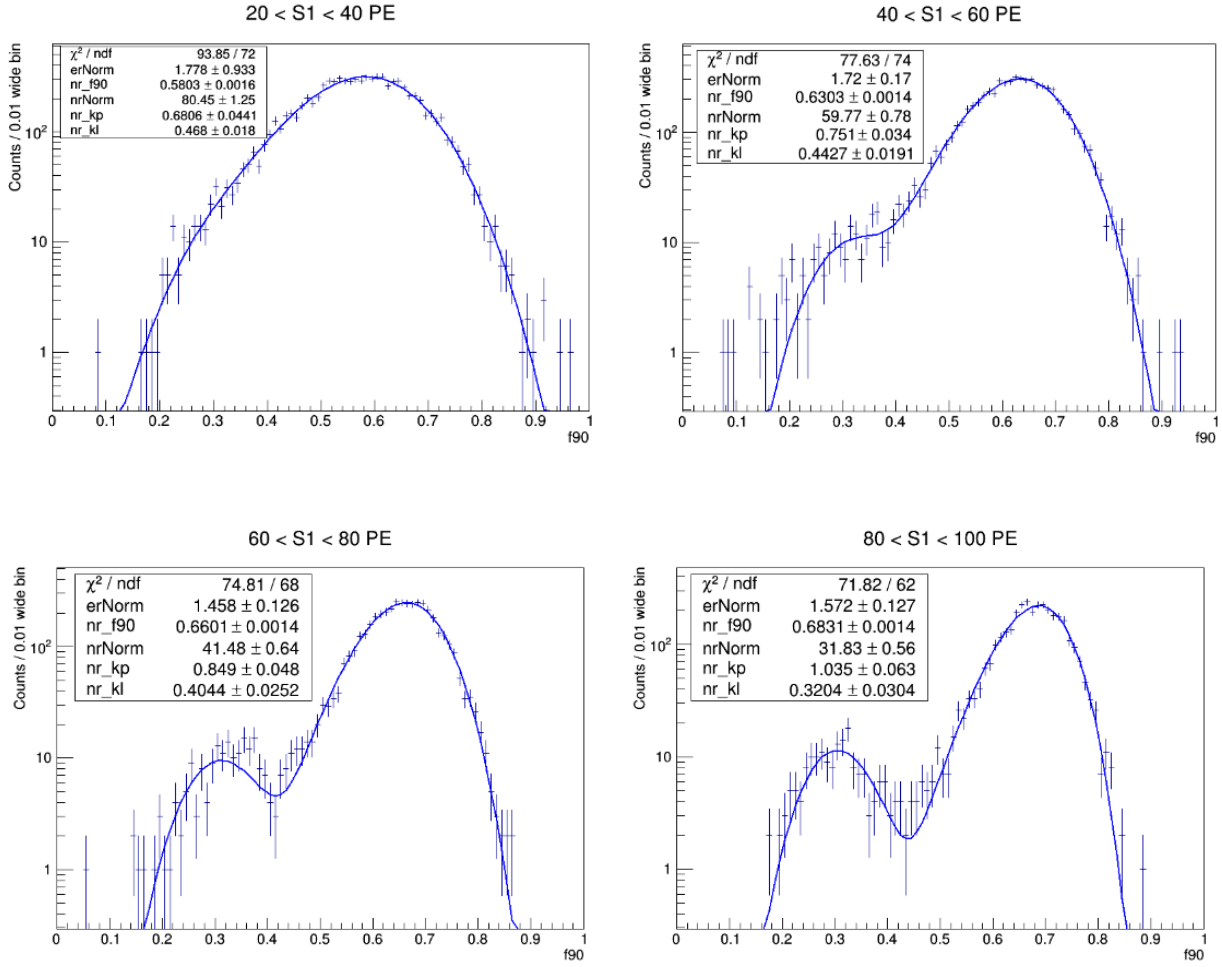

100 < S1 < 120 PE

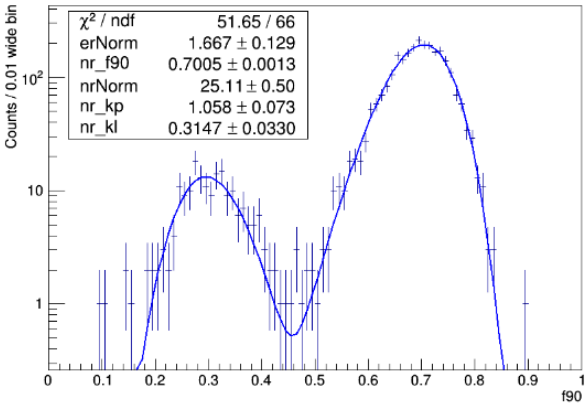

120 < S1 < 140 PE

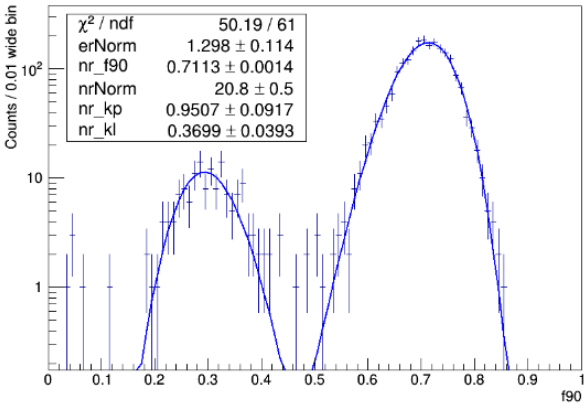

140 < S1 < 160 PE

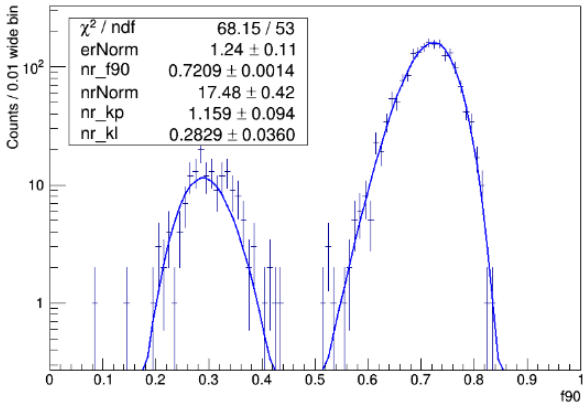

160 < S1 < 180 PE

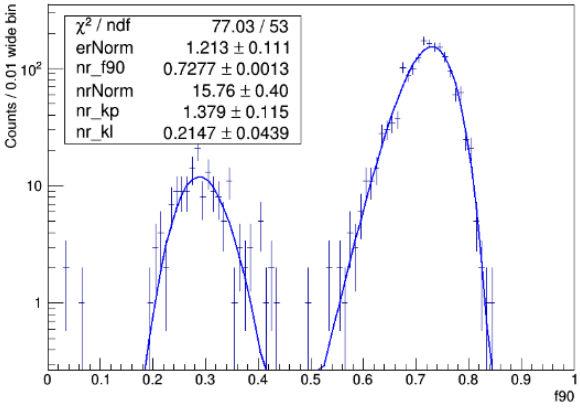

180 < S1 < 200 PE

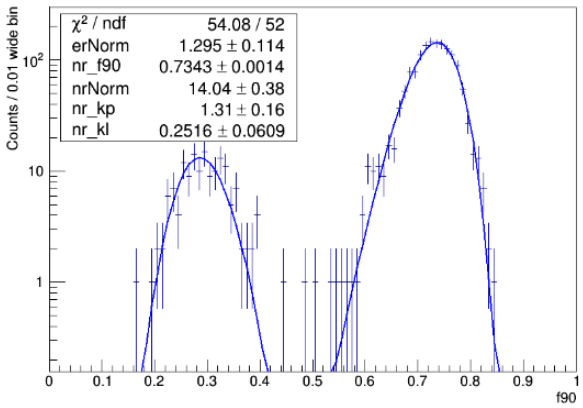

200 < S1 < 220 PE

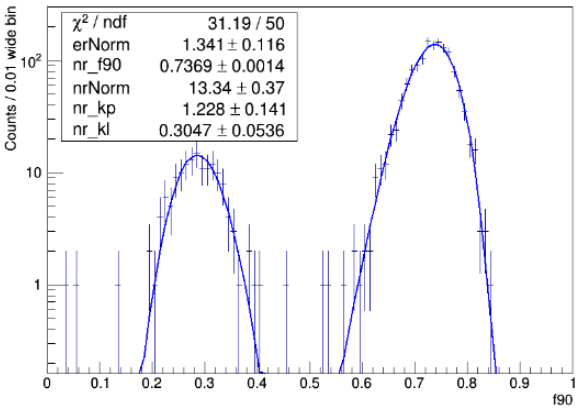

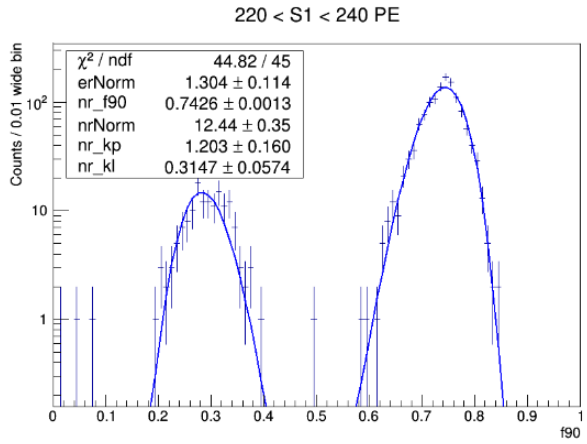
220 < S1 < 240 PE
χ² / ndf 44.82 / 45
erNorm 1.304 ± 0.114
nr_f90 0.7426 ± 0.0013
nrNorm 12.44 ± 0.35
nr_kp 1.203 ± 0.160
nr_kl 0.3147 ± 0.0574
Counts / 0.01 wide bin
f90

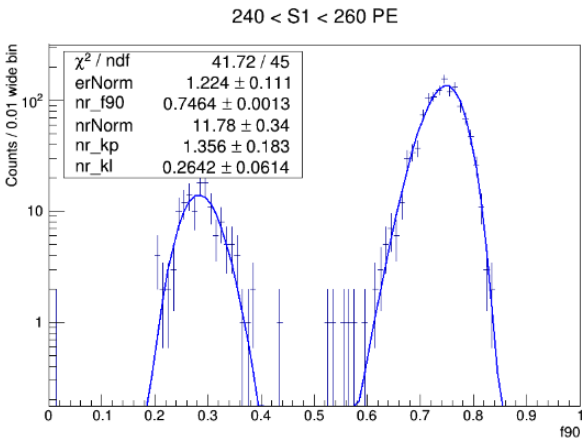
240 < S1 < 260 PE
χ² / ndf 41.72 / 45
erNorm 1.224 ± 0.111
nr_f90 0.7464 ± 0.0013
nrNorm 11.78 ± 0.34
nr_kp 1.356 ± 0.183
nr_kl 0.2642 ± 0.0614
Counts / 0.01 wide bin
f90

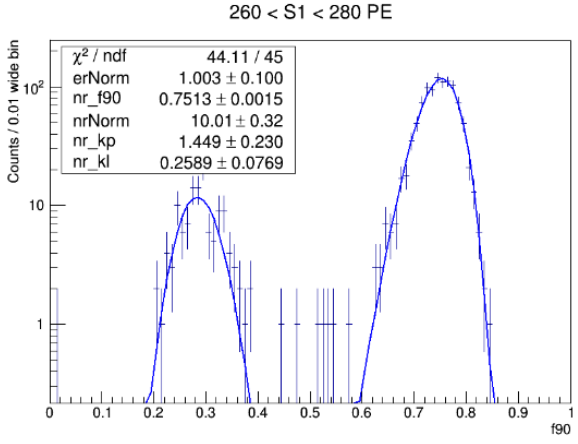
260 < S1 < 280 PE
χ² / ndf 44.11 / 45
erNorm 1.003 ± 0.100
nr_f90 0.7513 ± 0.0015
nrNorm 10.01 ± 0.32
nr_kp 1.449 ± 0.230
nr_kl 0.2589 ± 0.0769
Counts / 0.01 wide bin
f90

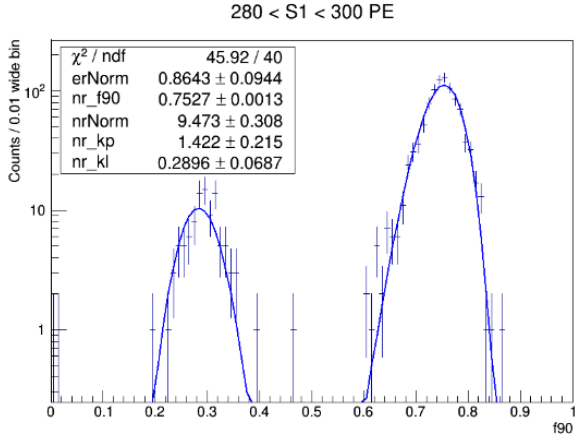
280 < S1 < 300 PE
χ² / ndf 45.92 / 40
erNorm 0.8643 ± 0.0944
nr_f90 0.7527 ± 0.0013
nrNorm 9.473 ± 0.308
nr_kp 1.422 ± 0.215
nr_kl 0.2896 ± 0.0687
Counts / 0.01 wide bin
f90

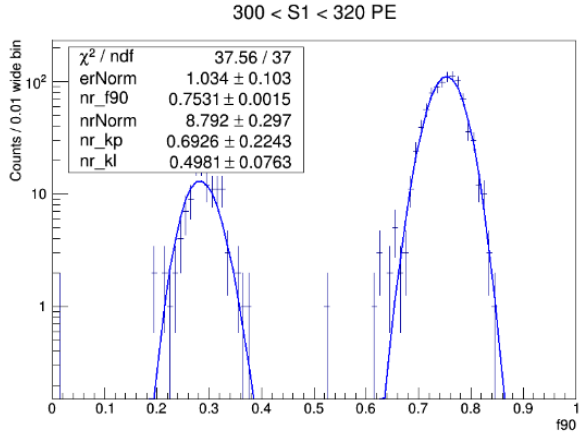
300 < S1 < 320 PE
χ² / ndf 37.56 / 37
erNorm 1.034 ± 0.103
nr_f90 0.7531 ± 0.0015
nrNorm 8.792 ± 0.297
nr_kp 0.6926 ± 0.2243
nr_kl 0.4981 ± 0.0763
Counts / 0.01 wide bin
f90

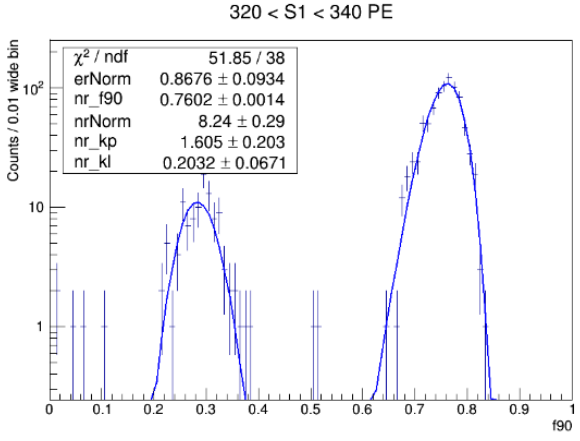
320 < S1 < 340 PE
χ² / ndf 51.85 / 38
erNorm 0.8676 ± 0.0934
nr_f90 0.7602 ± 0.0014
nrNorm 8.24 ± 0.29
nr_kp 1.605 ± 0.203
nr_kl 0.2032 ± 0.0671
Counts / 0.01 wide bin
f90

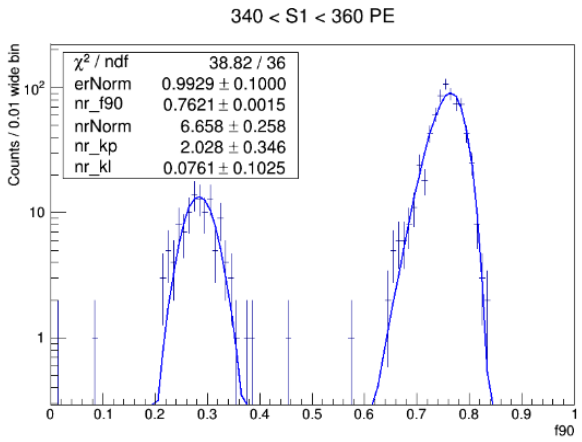
340 < S1 < 360 PE
χ² / ndf 38.82 / 36
erNorm 0.9929 ± 0.1000
nr_f90 0.7621 ± 0.0015
nrNorm 6.658 ± 0.258
nr_kp 2.028 ± 0.346
nr_kl 0.0761 ± 0.1025
Counts / 0.01 wide bin
f90

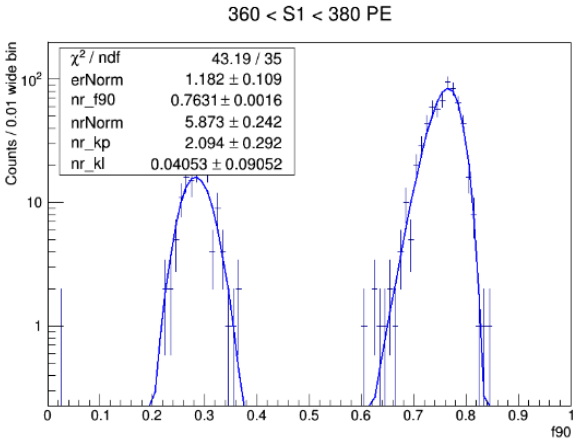
360 < S1 < 380 PE
χ² / ndf 43.19 / 35
erNorm 1.182 ± 0.109
nr_f90 0.7631 ± 0.0016
nrNorm 5.873 ± 0.242
nr_kp 2.094 ± 0.292
nr_kl 0.04053 ± 0.09052
Counts / 0.01 wide bin
f90

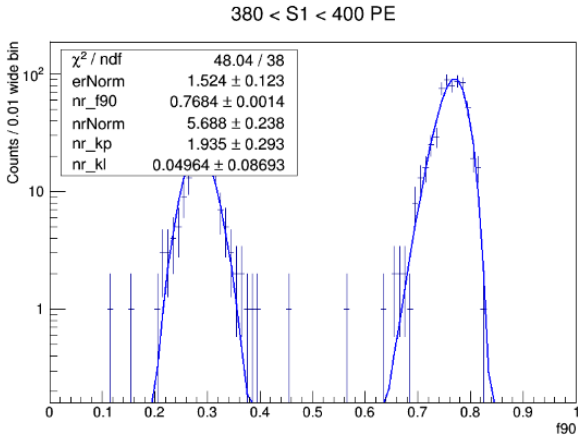
380 < S1 < 400 PE
χ² / ndf 48.04 / 38
erNorm 1.524 ± 0.123
nr_f90 0.7684 ± 0.0014
nrNorm 5.688 ± 0.238
nr_kp 1.935 ± 0.293
nr_kl 0.04964 ± 0.08693
Counts / 0.01 wide bin
f90

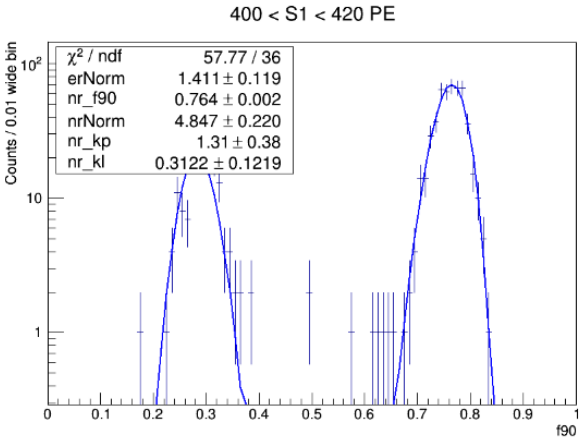
400 < S1 < 420 PE
χ² / ndf 57.77 / 36
erNorm 1.411 ± 0.119
nr_f90 0.764 ± 0.002
nrNorm 4.847 ± 0.220
nr_kp 1.31 ± 0.38
nr_kl 0.3122 ± 0.1219
Counts / 0.01 wide bin
f90

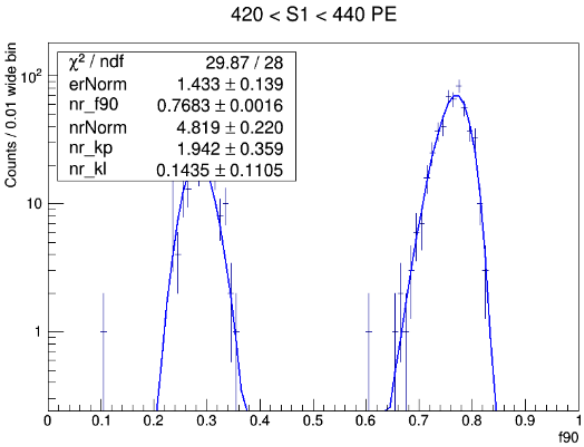
420 < S1 < 440 PE
χ² / ndf 29.87 / 28
erNorm 1.433 ± 0.139
nr_f90 0.7683 ± 0.0016
nrNorm 4.819 ± 0.220
nr_kp 1.942 ± 0.359
nr_kl 0.1435 ± 0.1105
Counts / 0.01 wide bin
f90

APPENDIX B
NUCLEAR RECOIL ACCEPTANCE VALUES

B.1 Tail Model

50% Acceptance

S1 [PE]	f_{90}	Bias	Variance
30	0.576381	-0.000960881	3.6368e-06
50	0.626859	1.88411e-05	1.30093e-06
70	0.656529	0.000123641	1.3075e-06
90	0.678732	0.000154655	1.27046e-06
110	0.696786	0.000143815	1.27445e-06
130	0.708917	8.54469e-05	1.33859e-06
150	0.717736	0.000108741	1.49295e-06
170	0.723937	0.000172114	1.4243e-06
190	0.731324	0.000144556	1.33637e-06
210	0.7345	0.000145113	1.37516e-06
230	0.740469	9.76952e-05	1.2799e-06
250	0.743991	7.88638e-05	1.29013e-06
270	0.748814	0.000135589	1.49294e-06
290	0.750492	0.000225176	1.50514e-06
310	0.752764	2.3963e-06	1.46073e-06
330	0.757871	-0.000386325	1.79752e-06
350	0.759004	0.000199468	1.77197e-06
370	0.760126	2.67807e-05	2.07752e-06
390	0.765972	-0.000102842	1.59272e-06
410	0.762651	6.95152e-05	2.02076e-06

Table B.1: 50% nuclear recoil acceptance values predicted by the Covariance (Tail) model for the given S1 bin, along with the bias and variance of the acceptance as determined by bootstrap resampling (Section 7.4).

90% Acceptance

S1 [PE]	f_{90}	Bias	Variance
30	0.438639	-0.00322931	4.29418e-05
50	0.519457	0.000233026	5.25436e-06
70	0.56453	0.00111552	4.91172e-06
90	0.595705	0.00177176	5.98e-06
110	0.623587	0.00107622	4.78605e-06
130	0.643827	0.000840528	4.5396e-06
150	0.656122	0.00141778	7.08388e-06
170	0.663596	0.00122053	5.73968e-06
190	0.675502	0.00117141	8.41928e-06
210	0.68118	0.000691761	4.37243e-06
230	0.690375	0.000682153	5.50993e-06
250	0.695257	0.00137959	5.54288e-06
270	0.700415	0.00136012	6.59029e-06
290	0.703085	0.00177011	7.27484e-06
310	0.712443	0.000452534	3.90381e-06
330	0.714952	-0.00277155	1.25681e-05
350	0.714899	0.00218213	1.12852e-05
370	0.718088	0.000819978	1.1133e-05
390	0.729057	-0.000642986	6.30036e-06
410	0.725418	0.000568588	6.66849e-06

Table B.2: 90% nuclear recoil acceptance values predicted by the Covariance (Tail) model for the given S1 bin, along with the bias and variance of the acceptance as determined by bootstrap resampling (Section 7.4).

99% Acceptance

S1 [PE]	f_{90}	Bias	Variance
30	0.315173	-0.00773116	0.000223323
50	0.421983	-0.000324843	3.29562e-05
70	0.478877	0.00203159	3.07473e-05
90	0.513454	0.00417657	4.38606e-05
110	0.552005	0.00203692	3.09852e-05
130	0.583594	0.00133337	2.79077e-05
150	0.595751	0.00456481	4.56289e-05
170	0.601249	0.00247642	3.99127e-05
190	0.619956	0.00224834	6.55893e-05
210	0.630065	0.000910408	2.73808e-05
230	0.643056	0.000924641	3.21152e-05
250	0.64782	0.00328047	3.79765e-05
270	0.652879	0.00286939	4.8631e-05
290	0.657262	0.00482531	4.46942e-05
310	0.678662	0.000702882	2.16494e-05
330	0.672231	-0.00822784	8.74699e-05
350	0.667064	0.0055462	7.59065e-05
370	0.672179	0.00232821	6.4854e-05
390	0.690194	-0.00146611	3.23562e-05
410	0.691138	0.000519526	4.37925e-05

Table B.3: 99% nuclear recoil acceptance values predicted by the Covariance (Tail) model for the given S1 bin, along with the bias and variance of the acceptance as determined by bootstrap resampling (Section 7.4).

B.2 Hinkley Model

50% Acceptance

S1 [PE]	f_{90}	Bias	Variance
30	0.57511	-0.00122371	1.83951e-06
50	0.626787	1.2738e-05	1.32021e-06
70	0.656555	0.000132483	1.29228e-06
90	0.678606	0.000167678	1.30355e-06
110	0.696772	0.000147189	1.30749e-06
130	0.708933	8.85344e-05	1.29672e-06
150	0.717745	8.59879e-05	1.48807e-06
170	0.723895	0.000161713	1.42102e-06
190	0.731256	0.000139418	1.37673e-06
210	0.734533	0.00011436	1.36363e-06
230	0.740475	0.000109364	1.2621e-06
250	0.743955	9.66429e-05	1.2926e-06
270	0.748801	0.000129313	1.54161e-06
290	0.75044	0.000257897	1.50149e-06
310	0.752821	-6.36986e-05	1.54343e-06
330	0.757952	-0.000411216	1.83148e-06
350	0.758934	0.000236834	1.78869e-06
370	0.760147	0.000112024	2.24201e-06
390	0.765968	-5.78382e-05	1.6382e-06
410	0.762678	0.000116057	2.10005e-06

Table B.4: 50% nuclear recoil acceptance values predicted by the Hinkley model for the given S1 bin, along with the bias and variance of the acceptance as determined by bootstrap resampling (Section 7.4).

90% Acceptance

S1 [PE]	f_{90}	Bias	Variance
30	0.435913	-0.00566251	7.99813e-06
50	0.51622	0.000511925	8.55632e-06
70	0.563743	0.00135744	5.70189e-06
90	0.595631	0.0018713	6.12061e-06
110	0.62382	0.000890283	4.95694e-06
130	0.643886	0.000850043	4.87591e-06
150	0.656119	0.00143362	7.20319e-06
170	0.663678	0.00115641	5.79035e-06
190	0.675528	0.00100782	7.68621e-06
210	0.681289	0.000563771	4.51311e-06
230	0.690455	0.000594183	5.34312e-06
250	0.69513	0.00138782	5.58347e-06
270	0.700224	0.00137118	6.84405e-06
290	0.703033	0.00171343	7.1392e-06
310	0.712477	0.000447843	4.10015e-06
330	0.715042	-0.00307932	1.30247e-05
350	0.715237	0.00180367	1.07877e-05
370	0.718065	0.000793997	1.06649e-05
390	0.729062	-0.000543308	5.79054e-06
410	0.725392	0.000480128	6.89937e-06

Table B.5: 90% nuclear recoil acceptance values predicted by the Hinkley model for the given S1 bin, along with the bias and variance of the acceptance as determined by bootstrap resampling (Section 7.4).

99% Acceptance

S1 [PE]	f_{90}	Bias	Variance
30	0.281399	-0.01532	6.75334e-05
50	0.396916	0.000771477	8.19756e-05
70	0.466674	0.00303534	4.60792e-05
90	0.506728	0.00474958	4.97714e-05
110	0.547613	0.00162044	3.5346e-05
130	0.579911	0.0014803	3.42708e-05
150	0.592074	0.00507656	5.28274e-05
170	0.598758	0.00257104	4.02139e-05
190	0.618078	0.00196983	5.53413e-05
210	0.627982	0.000744357	2.93578e-05
230	0.641297	0.000794554	3.1998e-05
250	0.645733	0.003412	3.90976e-05
270	0.650625	0.0031477	5.03147e-05
290	0.655456	0.00490517	4.4829e-05
310	0.677671	0.00102358	2.67985e-05
330	0.671007	-0.00872567	8.33198e-05
350	0.667928	0.00413132	6.75302e-05
370	0.671749	0.00192851	5.24367e-05
390	0.68995	-0.00132607	2.62133e-05
410	0.690067	0.000366303	4.63034e-05

Table B.6: 99% nuclear recoil acceptance values predicted by the Hinkley model for the given S1 bin, along with the bias and variance of the acceptance as determined by bootstrap resampling (Section 7.4).

BIBLIOGRAPHY

[1] V. Rubin, N. Ford. Rotation of the andromeda nebula from a spectroscopic survey of emission regions. *The Astrophysical Journal*, 159:379–403, February 1970.

[2] V. Rubin, W. K. Thonnard Jr, N. Ford. Rotational properties of 21 sc galaxies with a large range of luminosities and radii from ngc 4605 (r = 4kpc) to ugc 2885 (r = 122kpc). *The Astrophysical Journal*, 238:471–487, June 1980.

[3] H. Babcock. The rotation of the andromeda nebula. *Lick Observatory bulletin*, 49, 1939.

[4] F. Zwicky. Die rotverschiebung von extragalaktischen nebeln. *Helvetica Physica Acta*, 6:110–127, 1933.

[5] F. Zwicky. On the masses of nebulae and of clusters of nebulae. *The Astrophysical Journal*, 86:217–246, 1937.

[6] D. Clowe, et al. A direct empirical proof of the existence of dark matter. *The Astrophysical Journal Letters*, 648:109–113, September 2006.

[7] S. Rahvar. EROS/MACHO gravitational microlensing events toward LMC in Evans halo model. *International Journal of Modern Physics D*, 12:45–62, 2003.

[8] G. Steigman. Primordial nucleosynthesis in the precision cosmology era. *Annual Review of Nuclear and Particle Science*, 57:463–491, December 2007.

[9] R. Cooke, et al. Precision measures of the primordial abundance of deuterium. *The Astrophysical Journal*, 781, January 2014.

[10] P. Ade, et al. (Plank Collaboration). Plank 2015 results. XIII. Cosmological parameters. *Astronomy and Astrophysics A*, June 2016.

[11] C. L. Cowan Jr., F. Reines, F. B. Harrison, H. W. Kruse, et al. Detection of the free neutrino: a confirmation. *Science*, 124:103–104, July 1954.

[12] Y. Fukuda, et al. (Super-K Collaboration). Measurements of the solar neutrino flux from Super-Kamiokande's first 300 days. *Physical Review Letters*, 81:1158–1162, July 1998.

[13] J. Lesgourgues, S. Pastor. Neutrino cosmology and Planck. *New Journal of Physics*, 16(6), June 2014.

[14] S. D. M. White, C. Frenk, M. Davis. Clustering in a neutrino-dominated universe. *Astrophysical Journal*, 274:L1–L5, 1983.

[15] M. Kamionkowski. WIMP and axion dark matter. In *High-energy physics and cosmology. Proceedings, Summer School, Trieste, Italy, June 2-July 4, 1997*, pages 394–411, 1997.

[16] G. Bertone, D. Merritt. Dark matter dynamics and indirect detection. *Modern Physics Letters A*, 20(14):1021–1036, 2005.

[17] G. Bertone, D. Hooper, J. Silk. Particle dark matter: evidence, candidates and constraints. *Physics Reports*, 405(56):279–390, 2005.

[18] L. Baudis. WIMP dark matter direct-detection searches in noble gases. *Physics of the Dark Universe*, 4:50 – 59, 2014.

[19] M. C. Smith, et al. The RAVE survey: Constraining the local galactic escape speed. *Mon. Not. Roy. Astron. Soc.*, 379:755–772, 2007.

[20] J.D. Lewin, P.F. Smith. Review of mathematics, numerical factors, and corrections for dark matter experiments based on elastic nuclear recoil. *Astroparticle Physics*, 6:87–112, December 1996.

[21] T. Marrodn Undagoitia, L. Rauch. Dark matter direct-detection experiments. *Journal of Physics G: Nuclear and Particle Physics*, 43(1):013001, 2016.

[22] W. R. Leo. *Techniques for Nuclear and Particle Physics Experiments*. Springer-Verlag, Heidelberg, Germany, 1994.

[23] L. Baudis. Direct dark matter detection: The next decade. *Physics of the Dark Universe*, 1(12):94 – 108, 2012. Next Decade in Dark Matter and Dark Energy Next Decade in Dark Matter and Dark Energy.

[24] R. Bernabei et al. DAMA/LIBRA results and perspectives. *Bled Workshops Phys.*, 17(2):1–7, 2016.

[25] R. Agnese et al. Search for Low-Mass Weakly Interacting Massive Particles with SuperCDMS. *Phys. Rev. Lett.*, 112(24):241302, 2014.

[26] F. Petricca et al. New results on low-mass dark matter from the cresst-ii experiment. *Journal of Physics: Conference Series*, 718(4):042044, 2016.

[27] Barbosa de Souza et al. First search for a dark matter annual modulation signal with nai(tl) in the southern hemisphere by dm-ice17. *Phys. Rev. D*, 95:032006, Feb 2017.

[28] D. S. Akerib et al. Results from a search for dark matter in the complete lux exposure. *Phys. Rev. Lett.*, 118:021303, Jan 2017.

[29] V. Chepel, H. Arajo. Liquid noble gas detectors for low energy particle physics. *Journal of Instrumentation*, 8(04):R04001, 2013.

[30] P. Agnes, et al. (DarkSide collaboration). First results from the darkside-50 dark matter experiment at laboratori nazionali del gran sasso. *Physics Letters B*, 743:456 – 466, 2015.

[31] T. Doke, H. J. Crawford, A. Hitachi, J. Kikuchi, and P. J. Lindstrom, K. Masuda, E. Shibamura, T. Takahashi. Let dependence of scintillation yields in liquid argon. *Nuclear Instruments and Methods in Physics Research Section A: Accelerators, Spectrometers, Detectors and Associated Equipment*, 269(1):291 – 296, 1988.

[32] T. M. Miyajima, T. Takahashi, S. Konno, T. Hamada, S. Kubota, H. Shibamura, Doke. Average energy expended per ion pair in liquid argon. *Phys. Rev. A*, 9:1438–1443, Mar 1974.

[33] T. Doke, A. Hitachi, J. Kikuchi, K. Masuda, H. Okada, Eido Shibamura. Absolute scintillation yields in liquid argon and xenon for various particles. *Japanese Journal of Applied Physics*, 41(3R):1538, 2002.

[34] T. Doke, K. Masuda, E. Shibamura. Estimation of absolute photon yields in liquid argon and xenon for relativistic (1 mev) electrons. *Nuclear Instruments and Methods in Physics Research Section A: Accelerators, Spectrometers, Detectors and Associated Equipment*, 291(3):617 – 620, 1990.

[35] A. Hitachi, T. Takahashi, N. Funayama, K. Masuda, J. Kikuchi, T. Doke. Effect of ionization density on the time dependence of luminescence from liquid argon and xenon. *Phys. Rev. B*, 27:5279–5285, May 1983.

[36] D. Gastler, E. Kearns, A. Hime, L. C. Stonehill, S. Seibert, J. Klein, W. H. Lippincott, D. N. McKinsey, and J. A. Nikkel. Measurement of scintillation efficiency for nuclear recoils in liquid argon. *Phys. Rev.*, C85:065811, 2012.

[37] H. H. Loosli. A dating method with39ar. *Earth and Planetary Science Letters*, 63(1):51 – 62, 1983.

[38] J. Xu, F. Calaprice, C. Galbiati, et al. A study of the trace 39ar content in argon from deep underground sources. *Astroparticle Physics*, 66:53 – 60, 2015.

[39] P. Agnes, et al. (DarkSide collaboration). Results from the first use of low radioactivity argon in a dark matter search. *Phys. Rev. D*, 93:081101, Apr 2016.

[40] A. Wright. The darkside program at lngs. 2011.

[41] T. Alexander, et al. DarkSide collaboration. Light yield in darkside-10: A prototype two-phase argon tpc for dark matter searches. *Astropart. Phys.*, 49:44–51, 2013.

[42] V.M. Gehman, S.R. Seibert, K. Rielage, A. Hime, Y. Sun, D. M. Mei, J. Maassen and D. Moore. Fluorescence efficiency and visible re-emission spectrum of tetraphenyl butadiene films at extreme ultraviolet wavelengths. *Nuclear Instruments and Methods in Physics Research Section A: Accelerators, Spectrometers, Detectors and Associated Equipment*, 654(1):116 – 121, 2011.

[43] P. Agnes, et al. The electronics and data acquisition system for the darkside-50 veto detectors. *Journal of Instrumentation*, 11(12):P12007, 2016.

[44] G. Bellini et al. Cosmic-muon flux and annual modulation in Borexino at 3800 m water-equivalent depth. *JCAP*, 1205:015, 2012.

[45] Alex Wright, Pablo Mosteiro, Ben Loer, and Frank Calaprice. A highly efficient neutron veto for dark matter experiments. *Nucl. Instrum. Meth.*, A644:18–26, 2011.

[46] P. Agnes et al. The veto system of the DarkSide-50 experiment. *JINST*, 11(03):P03016, 2016.

[47] D.-M. Mei, Z.-B. Yin, L.C. Stonehill, and A. Hime. A model of nuclear recoil scintillation efficiency in noble liquids. *Astroparticle Physics*, 30(1):12 – 17, 2008.

[48] P. Agnes. g4ds: the DarkSide Simulation Tool. Presented at the Dark Matter 2016 conference, UCLA, February 2016.

[49] P. Agnes et al. CALIS - a CALibration Insertion System for the DarkSide-50 dark matter search experiment. *Submitted to: Nucl. Instrum. Meth. A*, 2016.

[50] H. Cao, et al. Measurement of scintillation and ionization yield and scintillation pulse shape from nuclear recoils in liquid argon. *Phys. Rev. D*, 91:092007, May 2015.

[51] J. Liu, R. Carr, D.A. Dwyer, W.Q. Gu, G.S. Li, R.D. McKeown, X. Qian, R.H.M. Tsang, F.F. Wu and C. Zhang. Neutron calibration sources in the daya bay experiment. *Nuclear Instruments and Methods in Physics Research Section A: Accelerators, Spectrometers, Detectors and Associated Equipment*, 797:260 – 264, 2015.

[52] W. H. Lippincott et al. Scintillation time dependence and pulse shape discrimination in liquid argon. *Phys. Rev.*, C78:035801, 2008. [Erratum: Phys. Rev.C81,039901(2010)].

[53] P.-A. Amaudruz et al. Measurement of the scintillation time spectra and pulse-shape discrimination of low-energy and nuclear recoils in liquid argon with deap-1. *Astroparticle Physics*, 85:1 – 23, 2016.

[54] D. V. Hinkley. On the ratio of two correlated normal random variables. *Biometrika*, 56(3):635–639, 1969.

[55] P. Agnes. *Direct Search for Dark Matter with the DarkSide Experiment*. PhD thesis, Université Sorbonne Paris Cité, 2017.

[56] Gerhard Bohm and Günter Zech. *Introduction to statistics and data analysis for physicists*. Deutsches Elektronen-Synchrotron, Hamburg, 2010.

[57] Trevor J. Hastie, Robert John Tibshirani, and Jerome H. Friedman. *The elements of statistical learning : data mining, inference, and prediction*. Springer series in statistics. Springer, New York, 2009.